Assessment and Control of a Cavitation-Enabled Therapy for Minimally Invasive Myocardial Reduction

by

Yiying Zhu

A dissertation submitted in partial fulfillment
of the requirements for the degree of
Doctor of Philosophy
(Biomedical Engineering)
in the University of Michigan
2017

Doctoral Committee:

Research Associate Professor Oliver D. Kripfgans, Co-Chair
Professor Cheri X. Deng, Co-Chair
Professor Katharine F. Barald
Professor Jeffrey A. Fessler
Professor Douglas L. Miller

Yiying I. Zhu

zhuyiy@umich.edu

ORCID iD: 0000-0003-0567-1391

Dedicated to all those who have offered me their generous help,

most especially my mother, Xuelin Yi,

whom I always regard as the greatest one for me in every way

ACKNOWLEDGEMENTS

Directly concerning the work in this dissertation, my deepest gratitude goes to my advisor, Doktor Oliver D. Kripfgans. The work in this dissertation would not have been possible without him. He has been very generous, spending time to guide and mentor me in the journey of exploring science. His limitless curiosity about science, inexhaustible passion on broadening knowledge, persistent and patient spirit to solve problems has motivated me to navigate the difficulties and enjoy the pleasures of learning. Not only academically, Dr. Kripfgans has also always been the strongest support mentally. It is him who introduced me to the world of running, where I learned to manage my stress and create work/life balance. It is a great honor to be his first doctoral daughter.

I would also like to thank other faculty members who have served in my doctoral committee, for their encouragement and critical comments which have improved this dissertation. Professor Douglas L. Miller has been offering me his generous attention and broad knowledge for the entire time. His high-level scope and being practical to handle variety in biological outcomes has been promoting our productive work. It is Professor Jeffrey A. Fessler, with critical thinking and passion in developing mathematical methods, whom I regard as my model as a scientist, led my interest to image processing and biomedical imaging. I appreciate Professor Katharine F. Barald for lending her expertise and time in examining my dissertation. She has given me a different view on the project as a biologist, which broadened my scope as an engineer. Professor Cheri X. Deng inspired me to be versatile by encouraging me

to be open minded and embrace various opinions from engineering, life science and medicine being in the biomedical field.

There are many other individuals I would like to address for all their help I have received to 'survive' my graduate school. I value every effort from the folks on our interdisciplinary research project whom I haven't mentioned: Drs. Xiaofang Lu, Chunyan Dou, Gabe Owens and William Armstrong. The academic and non-academic support from the faculty in my research home, Ultrasound Group in Basic Research of the Department of Radiology, can not be neglected. I would like to thank Drs. Paul L. Carson, J. Brian Fowlkes, Mario L. Fabiilli, Stephen Z and Guan Xu. Pinter for the mentorship. Additionally, my academic home Biomedical Engineering deserves mention, from which I was able to approach my academic mentors Drs. Zhen Xu, Xueding Wang and Tim L. Hall for advice. Besides this, I would have to acknowledge my elder academic brother, Dr. Kevin J. Haworth, who has been helping me both in person and remotely, via both verbal commutation and literature. Moreover, my academic younger brothers and sisters, Doctors to be: Alex Moncion, Rungroj Jintamethasawat and Kejie Chen, have all been an important part of my experience for scientific, social, and philosophical discussions. Also, my thank goes to my former colleagues, Won-Mean Lee and Dr. Fong Ming Hooi, who helped me settle down in the lab when I first started this journey.

Needless to say, it wouldn't be possible for me to achieve this far without love and support from my family, even though they have been far away, on the other side of the earth, in China. Other than the people from work, all my friends here have been my greatest companions through the past six years. With them, I was able to enjoy Ann Arbor and experience "Pure Michigan". Last but not least, I would like to express my deepest love to the University of Michigan, Ann Arbor, where I found out who I am and what I want to be.

PREFACE

During my years in graduate school, other than science, the most valuable thing I have learned is how to grow as a person.

This dissertation about a therapy development originates from the observations of biological effects in ultrasound imaging. Six years ago, I started working on this project as an electrical engineer with expertise in signal processing and limited basic knowledge in biology. However, up to now, I have witnessed the growth of the therapy development and of myself by absorbing the thoughts of professionals in various fields: physicists, engineers, biologists and physicians. Advancement occurs when you share your thoughts and when you encounter individuals who think outside of the box. This leads you to look at your thoughts at different angles.

I have always been a listener. I don't necessarily understand everything I've heard about but I try keep them in mind. As time passes, some random experience may trigger your understanding. I have learned 'No is not an answer', anything can be reasonably possible. You have to accept that you are not always going to be right or that you know everything. Breaking from such thoughts gives you the willingness to correct yourself.

Of course, it would be optimal if great things can be achieved at early stages. But if it doesn't, it will come as long as you practice patience. Even when you struggle for a long period, in time, what you have accumulated will start paying you back. I used to feel guilty having fun instead of working until I went through deep depression, confused about the meaning of life. It got more and more frustrating

when expectations were not achieved, until one day I realized the depression stemmed from me focusing on trying hard to please others and forgetting to love myself. Once I understood this, I started to appreciate every little thing happening around me and gradually learned that one's life is not about achieving one or several goals but instead, enjoying and fully utilizing every moment. The inspiration from running, music or showering may shed light on the solution of an equation, the development of experiment protocols or explanation of experiment observations.

With patience, you convey your message better, you understand better, you communicate better and you learn better.

Time is of the essence.

Yiying Zhu

Ann Arbor, Michigan

March, 2017

TABLE OF CONTENTS

LIST OF FIGURES

Figure

LIST OF TABLES

Table

LIST OF ABBREVIATIONS

HCM Hypertrophic Cardiomyopathy

MCE myocardial contrast echocardiography

MCET Myocardial Cavitation-Enabled Therapy

PRPA peak rarefactional pressure amplitude

fps frames per second

PRF pulse repetition frequency

HIFU high intensity focused ultrasound

PSF point spread function

MP methylprednisolone

USCA ultrasound contrast agent

RF radio frequency

HIFU high intensity focused ultrasound

CW continuous wave

FPGA Field-Programmable Gate Arrays

GUI Graphical User Interface

ECG Electrocardiography

ASA alcohol septal ablation

LVOT left ventricular outflow tract

ABSTRACT

Assessment and Control of a Cavitation-Enabled Therapy for Minimally Invasive Myocardial Reduction

by

Yiying Zhu

Co-Chairs: Oliver D. Kripfgans and Cheri X. Deng

Hypertrophic Cardiomyopathy (HCM), which occurs in 1/500 individuals worldwide can lead to sudden death in adults without prior symptoms. Echocardiography is commonly used to diagnose hypertrophic cardiomyopathy. Current treatment involves invasive and high-risk procedures such as surgery or catheter-based ablation of spetum to potentially prevent left ventricular outflow tract obstruction. A novel technique, called Myocardial Cavitation-Enabled Therapy (MCET), has been proposed as a means to achieve minimally invasive myocardial reduction, i.e. heart tissue ablation. MCET aims to target hypertrophic heart muscle over time without substantial tissue scarring. The treatment employs contrast echocardiography at higher than diagnostic pressure amplitudes to produce scattered microlesions (clusters of dead cells) by cavitating contrast agent microbubbles. The assessment and control of MCET is explored in three different contexts as follows:

- A computer-aided 3-D quantitative evaluation scheme, for acute studies, is developed to characterize macrolesions (targeted region for treatment) based on

histology sections, including lesion size and lesion density. The characterization is based on brightfield and fluorescence histological images as available in acute preclinical studies. The radially symmetric model employed to characterize macrolesion density is feasible for the study using a single focused beam to perform treatment. This methodology provides a volume-oriented, quantity-sensitive therapy evaluation. Results from parametric studies of MCET demonstrate that the quantitative scoring scheme reduces visual scoring ambiguity, overcomes the limitation of traditional visual scoring and works for cases with a large histologically identified lesion count, i.e. has an appropriate dynamic range for evaluating therapeutic applications. The presented results presented here have shown that MCET-induced macrolesions grow radially as the acoustic pressure amplitude increases. Using a swept beam as a new method seems to be able to shorten treatment time.

- MCET shows great potential as a minimally-invasive myocardial tissue reduction therapy after long-term healing. Chronic studies of 6-week show the maturation of MCET induced microlesions with quantitative results of the fibrotic tissue fraction. And the tissue reduction in a HCM rat model is demonstrated by showing and heart muscle wall shrinkage by about 16%, which is a therapeutically useful magnitude. MCET method can be improved by addition of adjuvant treatment with steroids and hypertension medication to help fibrosis reduction. Further development and refinement in larger animals of MCET treatment for HCM should fill the need for a new clinical treatment option.

- Feasibility of detection, quantification and localization for microbubble cavitation is investigated for treatment monitoring and controls. A passive cavitation imaging algorithm and variations of this algorithm provide spatial information on the extent of cavitation events. Cavitation sites can be localized with rea-

sonable spatial resolution. The described passive imaging algorithm applies to both systems: Verasonics (an ultrasound research platform) alone transmitting high intensity focused ultrasound (HIFU) and receiving signals with cavitation signatures, and Verasonics only for passive receiving with another HIFU system for therapeutic exposure. The overall therapy-monitoring scheme is able to adequately delineate the spatial location of triggered microbubble dynamics for real-time monitoring of monitoring of microlesion accumulation.

CHAPTER I

Introduction

1.1 Background

The need for myocardial reduction can arise for Hypertrophic Cardiomyopathy (HCM) and other ventricular hypertrophies, such as right ventricular hypertrophy associated with the tetralogy of Fallot, and as such, it represents a substantial public health concern. HCM is the most common genetic cardiovascular disease, occurring in 1 in 500 people (*Maron et al.*, 2012). Patients may experience shortness of breath, angina, palpitations, and even sudden death as has occurred in young athletes (*Maron and Maron*, 2013). Myocardial hypertrophy leads to the obstruction of the left ventricular outflow path in up to 75% of patients. About one-third of patients with obstruction remains symptomatic after pharmacological therapy and are candidates for myocardial reduction (*Marian*, 2009). The gold standard for diagnosis and treatment follow-up is echocardiography. The standard method for therapeutic reduction is septal myectomy, specifically, for removing asymmetric septal hypertrophy with perturbation of the mitral valve leaflets (*Maron et al.*, 2003b). Nonetheless alternatives to surgery have been sought using various forms of technology. For example, thermal ablation with high intensity focused ultrasound can be used to reduce cardiac tissue by accumulating focal lesions, but it has limited depth and requires a large aperture (i.e. open chest in the canine model) (*Otsuka et al.*, 2007). In

addition, radio-frequency catheter ablation of septal hypertrophy failed to produce efficacious septal narrowing while leading to a need for pacemaker implantation in 21% of patients (*Lawrenz et al.*, 2011). Transcatheter septal ablation with alcohol, as an alternative to surgery, has been developed, and it has achieved some success in terms of safety and efficacy (*Leonardi et al.*, 2010). However, this procedure unfortunately has a high incidence of heart blockage requiring permanent pacemakers in about 20% of cases(*Marian*, 2009). In addition, there is a substantial risk of serious arrhythmia arising after healing of the alcohol-induced infarction to scaring with subsequent cardiac remodeling (*Nishimura and Ommen*, 2010). The technique of transcatheter septal ablation has not been widely accepted, and a better less-invasive alternative to surgery is sorely needed.

Microbubbles cavitate with presence of ultrasound. The potential for cavitation activity in diagnostic ultrasound was recognized early in safety studies based upon theoretical analysis (*Apfel*, 1982; *Carstensen and Flynn*, 1982). However, at that time, cavitational bioeffects of pulsed ultrasound were unknown. Without the presence of exogenous cavitation nuclei, cavitation is not detectable for diagnostic ultrasound (*Carstensen et al.*, 2000), and thresholds to induce cavitation activity are expected to be quite high (*Church*, 2002). Ultrasound contrast agents were invented to enhance blood echogenicity with stabilized microbubble suspensions. The highly non-linear response of the microbubbles provides novel opportunities for diagnostic imaging (*Bruce et al.*, 2003). The cavitational response to even diagnostic pulses also leads to a variety of microscale bioeffects in contrast enhanced diagnostic ultrasound, which are certainly undesirable but of uncertain medical impact (*Miller et al.*, 2008). Conversely, the ultrasonic cavitational bioeffects have been a boon to a search on new therapeutic strategies. The activation of microbubbles in the circulatory system for therapeutic purposes continues to be explored. Ultrasound microbubble activation therapies have attractive features, including the ability to guide the treatment using

ultrasound imaging and real-time feedback from the microbubble emissions (*Cochran et al.*, 2011; *Kooiman et al.*, 2014; *Vignon et al.*, 2013). Prospective treatments range from transient opening of capillaries, such as the blood-brain barrier (*Burgess and Hynynen*, 2014), to complex methods for drug or gene delivery using specially prepared gaseous delivery vehicles that can be targeted to the desired region for treatment (*Ma et al.*, 2013). These methods have been studied for treatments like gene therapy, various cancer treatments and thrombolysis (*Ibsen et al.*, 2013; *Laing and McPherson*, 2009; *Unger et al.*, 2014).

High pressure amplitude myocardial contrast echocardiography (MCE) has been shown to lethally injure cardiomyocytes (*Miller et al.*, 2005a). This phenomenon leads to randomly scattered microlesions involving one or a few cardiomyocytes seen in histology. The microlesions represent cardiomyocyte loss and, as after a long-term healing process, they appear to result in fibrous microscar formation with tissue shrinkage. This presents another attractive opportunity for therapeutic applications. Based on aforementioned process of tissue shrinkage, Myocardial Cavitation-Enabled Therapy (MCET) was proposed as a new noninvasive alternative for patients needing cardiac tissue reduction (*Miller et al.*, 2014a).

Treatment of MCET is guided by the ultrasound used diagnose and characterize the hypertrophy in need of reduction. The MCET method is non-invasive with microbubbles doing microsurgery. The scattered nature of the cell loass maintains the treated region as functional myocardium with microcirculation and electrical conductivity, rather than being cut away by surgery or essentially killed and fixed by alcohol ablation. It takes advantage of the use of contrast agent microbubbles to produce scattered sites of ultrasonic cavitation nucleation and microlesion production in the heart, which may provide a relatively safe means of targeted tissue reduction therapy. This will represent a significant departure from current practice and a potential breakthrough in care of patients with HCM and other conditions requiring

myocardial reduction. The dispersed nature of MCET microlesions should prevent infarction-induced arrhythmia by leaving most of the cardiac tissue unharmed, even in the target volume. The idea of MCET may become a viable option as a conservative initial remedy with repeated treatment, or a therapy for patients for whom surgery is not an option, or even a proactive prophylactic procedure. This development will significantly improve the prognosis and quality of life for patients living with these life threatening conditions.

1.2 Therapy Mechanism

Illustrating the therapeutic mechanism of MCET involves several core concepts that form its technical foundation, requiring careful definitions and a solid background. Those components are ultrasound, microbubble cavitation, microlesion and macrolesion. This introductory section will define these terms and explain their relevance.

1.2.1 Physics of Ultrasonic Microbubble Cavitation

Ultrasound is a longitudinal pressure wave with a frequency above 20 kHz. As schematically shown in Figure 1.1(a), an acoustic pressure wave alternately compresses (compression phases; dark gray regions) and expands (rarefaction phases; light areas) the medium through which it travels. Hence, when an ultrasound wave is passing through a medium, the molecules inside the medium can be actually displaced as illustrated in Figure 1.1(b). The black dots represent molecules present in the medium that are shifted from their equilibrium state. They are compressed at high pressure and expanded at low pressure (*Leighton*, 2007).

The original intention of gas microbubble deployment in ultrasound imaging was to provide contrast an enhancement, as microbubbles improve the scattering of the ultrasound wave, and are, therefore, also called "echo contrast agents" (*Calliada et al.*,

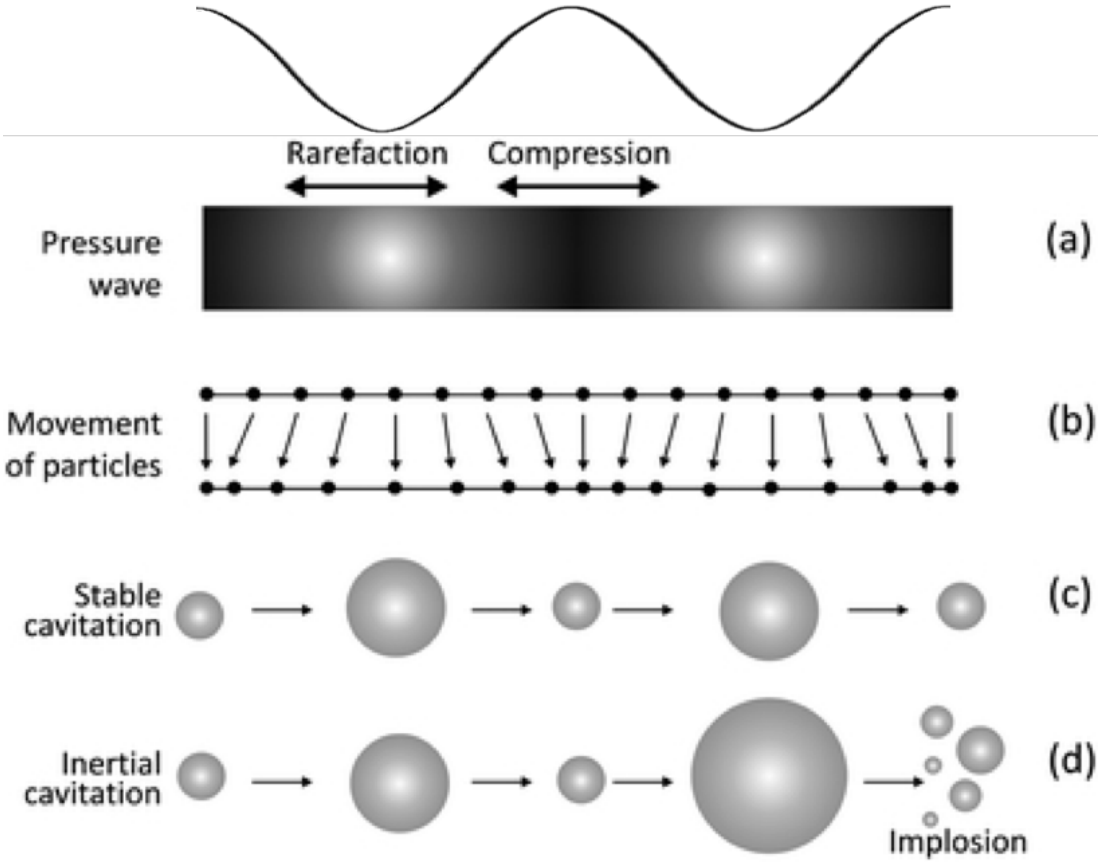

Figure 1.1: Schematic representation of physics of ultrasound and microbubble cavitation. (a) An acoustic pressure wave, alternately compresses (compression phases; dark gray regions) and expands (rarefaction phases; light areas). (b) Displacement of molecules in a pressure wave: the black dots represent molecules present in the medium that are shifted from their equilibrium state when ultrasound is passing through. (c) and (d) show, respectively, stable and inertial cavitation of microbubbles. Adapted from (*Lentacker et al.*, 2009)

.

1998). In this context, "microbubbles" and "contrast agents" are used interchangeably throughout this dissertation.

Microbubbles can be as simple as air-filled bubbles of micrometer sizes, but microbubbles in this work are composed of a perfluorocarbon gas core surrounded by a stabilizing shell, as are all currently commercially available ultrasound contrast agents, e.g., Definity®(Lantheus Medical Imaging, Inc., N. Billerica, MA) (*Ignee et al.*, 2016). This structure prevents gas diffusion out of the microbubble which drastically enhances their stability and circulation time in blood.

Ultrasonic **microbubble cavitation** is defined as the process of microbubbles interacting with an ultrasound field (*Fowlkes and Holland*, 2000). As illustrated in Figure 1.1(c) and (d), microbubbles that are exposed to ultrasound start to cavitate. Specifically, cavitating microbubbles alternate between shrinking and expanding as a result of, respectively, the compressive (high) and rarefactive (low) pressure phases of the ultrasound wave.

Cavitation is classified into stable cavitation (SC) and inertial cavitation (IC) (*McLaughlan et al.*, 2010). Stable cavitation (so named non-inertial cavitation) comprises stable, low amplitude oscillation of the microbubbles with resonance frequencies depending on bubble size and other properties (Figure 1.1(c)). Such stable oscillations create strong liquid flows around the microbubbles, the so-called microstreams. Microstreams can apply shear stress on cell membranes which may result in a transient opening of the cell membranes (*Sboros*, 2008; *Wu et al.*, 2002) (Figure 1.2). In response to peak rarefactional pressure amplitude (PRPA)s in excess of the **inertial cavitation threshold**, the microbubbles grow rapidly during the rarefaction phase, until they collapse due to the inertia of the inrushing fluid. This cavitation results in the fragmentation of the microbubbles into many smaller microbubbles (Figure 1.1(d)). This type of cavitation is called inertial cavitation (*Newman et al.*, 2001; *Newman and Bettinger*, 2007). During the collapse of the microbubbles, shock

waves are generated in the fluid near the microbubble (Figure 1.2). Finally, jet formation can also occur when a collapsing microbubble is located close to a surface like a cell membrane. In this case, an asymmetrical collapse takes place, which results in the formation of a liquid jet towards the surface. The shock waves and microjets create forces that can perforate cell membranes and even permeabilize blood vessels (*Lentacker et al.*, 2009).

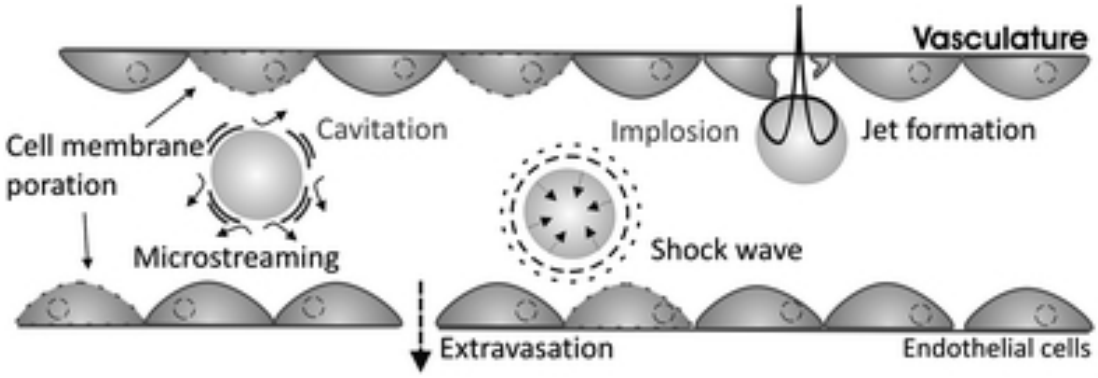

Figure 1.2: Schematic representation of biological effects which may arise during cavitation and implosion of microbubbles. Microstreams can apply a shear stress on cell membranes which may result in a transient opening of the cell membranes, so called sonoporation (*Sboros*, 2008; *Wu et al.*, 2002; *Bao et al.*, 1997). Shock waves and microjets generated from bubble collapse create forces that can perforate cell membranes and even permeabilize blood vessels leading to possible extravasation and damage to adjacent cells outside blood vessels (*Lentacker et al.*, 2009; *Miller*, 2007; *Lentacker et al.*, 2009).

1.2.2 Microlesion and Macrolesion

Studies have demonstrated that an *in vivo* PRPA threshold (Figure 1.3) exists for MCE to generate premature electrocardiographic complexes and lethal injury of cardiomyocytes in an animal model (*Miller et al.*, 2005a). This phenomenon leads to randomly scattered **microlesions** involving one or a few lethally injured cardiomyocytes as seen in histology within a confined region of millimeters named **macrolesion**. The injured cardiomyocytes represented by the microlesions appear to gradually resolve

with minimal fibrous scar formation as followed through a 6-week healing process (*Miller et al.*, 2005b). This cardiomyocyte loss forms the basis of tissue shrinkage induction.

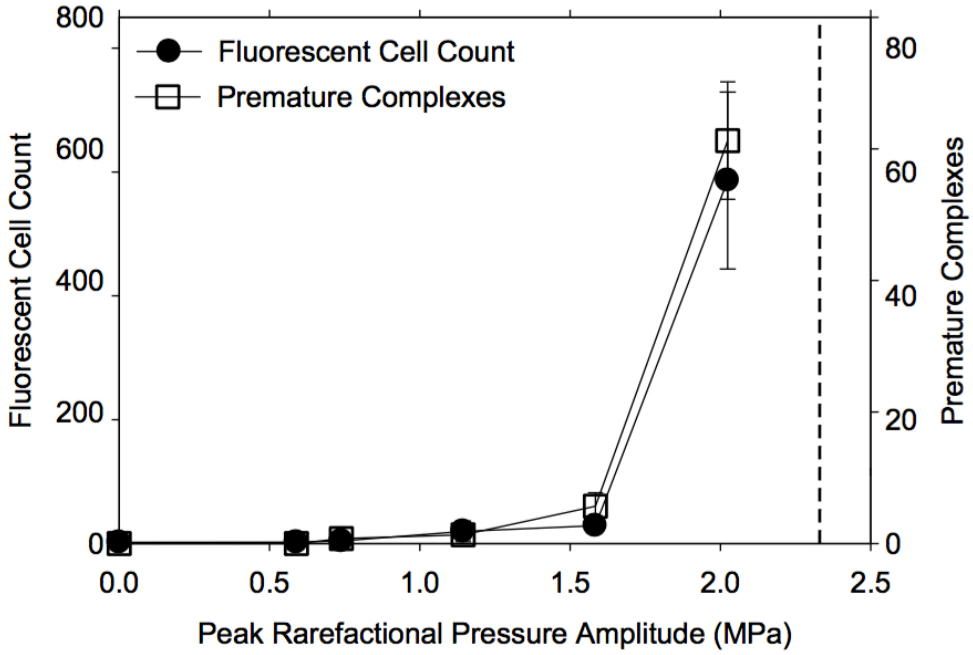

Figure 1.3: Plots of fluorescent cell counts of lethally injured cardiomyocytes forming microlesions in single frozen sections 1 day post exposure compared to the ECG premature complexes counted during 1.5 MHz MCE with Definity® infusion. The dashed line marks the upper limit for diagnostic ultrasound. Cell count and number of premature heartbeats had a similar dependence on PRPA. Adapted from (*Miller et al.*, 2014a)

After MCET treatment, a macrolesion is created in which the myocardial volume experiences a ultrasound field pressure above the PRPA threshold (*Zhu et al.*, 2015a). As illustrated in Figure 1.4, macrolesions identified by dark color resulting from Evans blue leakage in heart phaotographs are of different dimensions depending on their exposure conditions. At higher magnification imaging for fluorescent histological slices, a bulk of scattered microlesions of different densities within macroleions can be identified. The distribution of microlesions is associated with that of ultrasonically cavitated microbubbles in the myocardium.

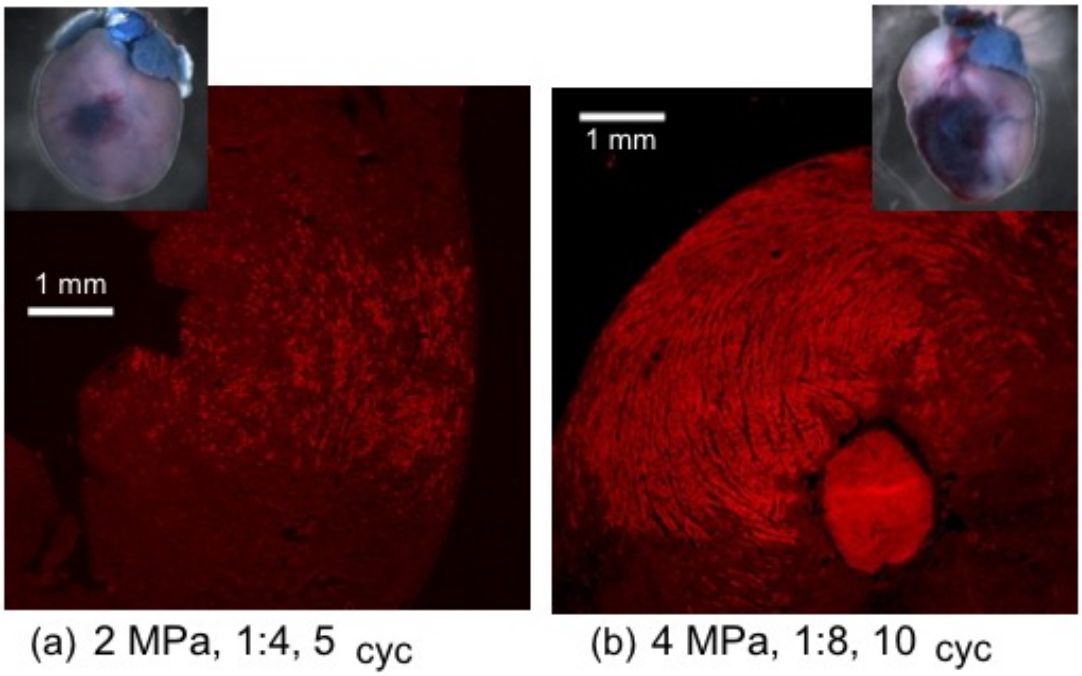

Figure 1.4: Examples of heart photographs made one day after ultrasound exposure. Evans blue staining of lethally injured cardiomyocytes and the corresponding fluorescent image slices with microlesions fluorescence red for treatment conditions for (a) PRPA = 2 MPa, triggered every 4 heart beats, therapeutic pulse of 5 cycles (b) PRPA = 4 MPa, triggered every 8 heart beats, therapeutic pulse of 10 cycles. Adapted from (*Miller et al.*, 2014a)

1.3 Process of MCET Therapy

MCET presents a minimally invasive treatment for myocardial reduction. As illustrated in Figure 1.5 ultrasound contrast agent microbubbles are continuously infused intravenously during treatment. With the presence of contrast agents in the myocardial capillaries identified by MCE hyperechogenicity, intermittent contrast destruction are facilitated using transcutanuous focused ultrasound therapy transducers. Ultrasonic exposures are triggered every N cardiac cycles to allow microbubble reperfusion after destruction, so that microbubble cavitation induced scattered histologically definable microlesions gradually accumulate to the desired density level (*Miller et al.*, 2014a). The scattered microlesions are created within a targeted volumetric macrolesion by focusing ultrasound energy. The microlesions represent cardiomyocyte loss and lead to tissue shrinkage after the healing process. The fractional macrolesion is the site where tissue shrinkage is intended, with the tissue reduction portion proportional to microlesion distribution density, *i.e.* total damaged cardiomyocytes over affected volume, assuming the tissue loss equal to the volume of eventually removed microlesions.

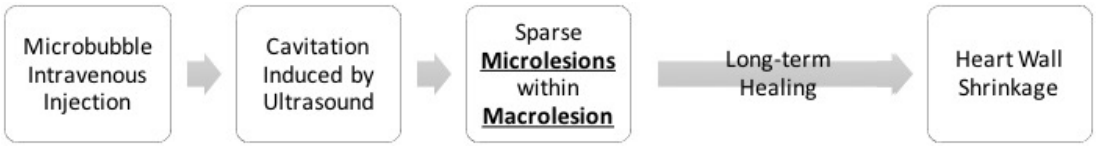

Figure 1.5: Flow chart of the MCET process

1.4 Dissertation Overview

The following chapters of this dissertation will delve more deeply into the development of MCET. In particular, the first two chapters will concentrate on acute studies in a rat model. The first chapter will discuss a three-dimensional analysis revealing microlesions created within the treated macrolesion. The second chapter

will focus on the tuning of key parameters involved in MCET and discussion in a quantitative manner, for pre-clinical treatment plans for myocardial lesion creation and properties. The third chapter will inspect the long-term effects of MCET over 6 weeks in rat models. The fourth chapter will investigate treatment monitoring in terms of cavitation. Finally, the dissertation summary and directions for possible future work will be addressed. Each chapter will contain an introductory section to provide necessary background material so that the chapter can be read independently from the rest of the dissertation. A more detailed outline of the dissertation is given below.

Chapter II provides a three-dimensional analysis of stacked heart tissue histology sections revealing microlesions. It presents an effective means to characterize the overall impact or the "macrolesion" created in the volume of interest. The quantitative image analysis overcomes the problem of optimization of the treatment caused by the uncertainties in the visual scoring of microlesion accumulation after therapy-level treatment. This work was published in the journal "IEEE Transactions on Biomedical Engineering" (*Zhu et al.*, 2015a).

Chapter III compliments Chapter II by investigating the tuning of key parameters involved in MCET and paving the way for pre-clinical treatment planning of myocardial lesion creation thereof, in a quantitative manner. The resulting assessment of the therapeutic effect drives parameter adjustment to optimize MCET ultrasound parameters and administration of microbubble strategies to achieve efficacious effect . This work was published in the journal "Journal of Therapeutic Ultrasound" (*Zhu et al.*, 2015b).

Chapter IV discusses the healing process and adjuvant treatments over time after MCET, leading to eventual myocardial reduction, i.e. decrease in heart wall thickness.

Chapter V describes a MCET platform with therapeutic capability and treatment monitoring. It investigates possible schemes based on microbubble cavitation

feedbacks.

Chapter VI concludes the dissertation with a summary and a discussion on the outlook for future extensions and refinement of the current research portfolio.

CHAPTER II

Characterization of Macrolesions Induced by MCET

2.1 Introduction

Hypertrophic cardiomyopathy (HCM), involving enlargement and hyperplasia of the myocardium, occurs in at least one out of 500 people. Sudden death is the most visible and unpredictable consequence of Hypertrophic Cardiomyopathy (HCM), occurring without warning signs or symptoms. It has been reported that HCM is the most common cause of sudden death in young people, and is the most frequent cause of sudden death in US competitive athletes (*Maron and Maron*, 2013). Although pharmacologic therapies have exhibited significant positive effects, there remain substantial undesired side effects, leaving approximately a third of patients as candidates for myocardial reduction (*Marian*, 2009).

The definitive treatment for HCM is surgical myectomy (*Ommen and Nishimura*, 2004), which involves resection of a small portion of the interventricular septum at its base. Less-invasive alternatives have been explored using a variety of techniques, most commonly an endovascular procedure. However, the need for permanent pacing, the inability to address concomitant anatomic abnormalities and the uncertainty about the long-term effects of having caused substantial myocardial necrosis and scaring

are undesirable. Other approaches such as thermal ablation (*Otsuka et al.*, 2007) or histotripsy (*Xu et al.*, 2004) reduce cardiac tissue by accumulating ultrasonic focal lesions.

For decades, ultrasonic bioeffects from microbubble inertial cavitation have been discussed for their therapeutic potentials (*Miller et al.*, 2008). Concurrent studies have investigated cavitation-induced microvessel and cell injuries (*Chen et al.*, 2012). A novel technique using contrast echocardiography using higher than diagnostic pressure amplitudes, named Myocardial Contrast Enabled Therapy (MCET), is hypothesized to induce a fractional macrolesion with sparse and histologically definable microlesions, which in turn shrink the diseased heart muscle without substantial scaring (*Miller et al.*, 2005b).

Currently, therapeutic ultrasound has great potential in medicine as a noninvasive method to treat tumors, promote hemostasis, and treat other diseases due to its ability to penetrate deeply and deposit thermal or mechanical energy at a specific site with submillimeter accuracy. Various imaging modalities, including x-ray, computed tomography, magnetic resonance imaging, and ultrasound imaging, can provide precise targeting and therapy monitoring (*Vaezy et al.*, 2001).

Passive cavitation imaging has been demonstrated for potential use with continuous-wave high-intensity focused ultrasound thermal ablation (*Gyöngy and Coussios*, 2010) and for pulsed-wave ultrasound therapy insonations (*Haworth et al.*, 2012). A system for microbubble-mediated sonothrombolysis utilizing therapy guidance and cavitation imaging has been developed (*Vignon et al.*, 2013).

Myocardial Cavitation-Enabled Therapy (MCET) is performed under the guidance of echocardiography. Ventricular premature complexes and blood pressure can provide temporal feedback (*Miller et al.*, 2014a), while inertial cavitation mapping combined with anatomical imaging could delineate the spatial accumulation of cardiomyocytic response.

To evaluate the effectiveness of MCET treatment and modulate its treatment parameters, such as ultrasound amplitude, contrast dose, and treatment duration, an evaluation scheme is needed for characterizing microlesions. In previous studies, myocardial necrosis (*Miller et al.*, 2005b), (*Miller et al.*, 2005a) was evaluated qualitatively by visual identification and scoring of Evans blue-stained cells in frozen histological slices of heart tissue (*Miller et al.*, 2011). However, visual scoring only yields a limited 1-D descriptor, i.e., scalar information of damaged cells assessed for each tissue slice, which is far from adequate to describe a comprehensive treatment outcome for tuning therapeutic inputs. For example, a qualitative score of 58,790 more than 23,560 helped make relative judgments about the optimum exposure parameters in terms of overall induced impact, but it gave no information about the amount of tissue reduction. Thus, an objective and quantitative scoring is needed to precisely determine treatment outcome and volume-based treatment. Spatial distribution evaluation is essential to ultimately develop a safe and effective therapeutic application.

Numerous methods have been devised for cellular and histological analysis. Molecular imaging, defined as the visual representation, characterization, and quantification of biological processes at cellular and subcellular levels, could be used to noninvasively detect and monitor cancer treatments (*Weissleder*, 2002). It enables tumor localization, spatial visualization of specific molecular markers, and biological processes that influence tumor behavior and/or response to therapy (*Weissleder*, 2006).

Regarding cellular microscopy, computational imaging provides multidimensional and quantitative image analysis, enabling mathematical modeling of cell biology. Employed process steps include image acquisition and preprocessing, registration, segmentation, volume rendering, etc. (*Eils and Athale*, 2003). Image segmentation, including thresholding, region growing, and cluster- ing, plays an important role in characterizing contents of medical images (*Pham et al.*, 2000).

This chapter describes a scheme for MCET characterization in acute preclinical studies (*Zhu et al.*, 2015a). A computer-aided histological evaluation of MCET-induced macrolesions has been implemented to quantify treatment outcome. The point of the presented method is to provide the volumetric macrolesion determination to approximate the expected amount of tissue reduction, which was not available from the qualitative visual score. Two-dimensional brightfield and fluorescence images were evaluated by an algorithm, which automatically identified microlesions, and characterized the volume-oriented fractional macrolesion. Subsequently, this method can be applied to optimize ultrasound pulse parameters, exposure duration, and contrast agent dose for MCET treatment of HCM, which would require up to 25% vol-vol tissue reduction in some myocardial areas.

2.2 Methods and Materials

2.2.1 Animal and Tissue Preparation

In concomitant research designed to optimize the timing of pulses for MCET, tissue samples were collected and prepared for histological evaluation. For this study, these samples were utilized for development of computer-aided evaluation. Briefly, *in vivo* animal procedures were conducted on 20 male Sprague-Dawley rats (Charles River, Wilmington, MA, USA) and five sham rats weighing 331 ± 33 g under the approval and guidance of the University Committee on Use and Care of Animals. All rats in the treated group were injected with Definity® (Lantheus Medical Imaging, Inc., N. Billerica, MA) at a rate of 5 L/kg/min. MCET was performed with 2 ms period 4 kHz pulse repetition frequency (PRF) 1.5 MHz ultrasound burst of five cycle pulses at 4.0 MPa peak rarefactional pressure amplitude (PRPA) by use of a 1.9 cm diameter and 3.8 cm focus single element therapy transducer, triggered at one beat out of four heart beats. The therapeutic transducer was focused approximately 0.5

cm into the myocardium (*Miller et al.*, 2014a). While the distance to the myocardium might change a few millimeters, the effect of choice of cardiac phase was studied in Miller et al. (*Miller et al.*, 2014b) and found to not be significant. Before being exposed to 5 minutes of therapy, all rats were injected with Evans blue, which has been proven to be a dependable stain for histological determination of cell necrosis (*Jacyn Baker and Mock*, 1994). After being frozen in compound (Tissue-Tek, Sakura Finetek USA, Inc., Torrance, CA, USA) on dry ice, each heart was dissected to provide samples covering the entire exposed myocardial volume. Up to 40 sections, 10 μm thick, for each heart were cut every 200 μm into the sample to cover about 5 mm of the dissected portion of the heart. Two hundred micron spacing was set to avoid possible overlap of stained cardiomyocytes in adjacent sections and thoroughly sample the cardiac volume. However, it should be noted that some stained cells present in between sections were not actually observed, but assumed by extrapolation to have the same fractional lesion area over the 190 μm unsampled space.

2.2.2 Cardiomyocyte Scoring

Besides the proposed automatic characterization scheme, visual scoring and measurement of troponin I in plasma were performed to evaluate cardiomyocyte injuries. Visual scoring was based on Evans blue staining as described previously (*Miller et al.*, 2014a). Troponin I was analyzed from plasma samples analyzed one day after euthanasia with an ELISA assay kit (Rat Cardiac Tn-I (ultra sensitivity), Life Diagnostics, Inc., West Chester, PA, USA). This cardiac enzyme is a sensitive indicator of cardiac injury in rodents (*O'brien et al.*, 2006).

2.2.3 Microscope Image Acquisition

To enable computer-aided evaluation, both brightfield and fluorescence images were obtained for each tissue-section through a microscope camera system (SPOT

Flex, Diagnostic Instruments, Inc., Sterling Heights, MI, USA) via fluorescent stereomicroscopy (LeicaMZFLIII, Leica Microscopy Systems, Ltd., Heerbrugg, Switzerland) with a high resolution and large field of view objective (Leica Plan APO 1.6x, Leica Microsystems, Ltd., Heerbrugg, Switzerland). The images were acquired as 16 bit 4,096 by 4,096 pixel, RGB, covering the entire tissue sections. One image set of treated myocardium at the approximate midpoint of the treated zone is shown in Figure 2.1(a) and (b); a sham image set is shown in Figure 2.1(c) and (d). Macrolesion is a volume defined as a bulk of the microlesions within the target area, where a microlesion was defined simply as a local collection of one or a few damaged cardiomyocytes. An example showing 3D macrolesion projection onto 2D is identified by MaL (macrolesion) shown in Figure 2.1(a). Left ventricle (LV), right ventricle (RV), and septum (SP) are also labeled. The damaged cardiomyocytes in scattered microlesions appear stained light blue in the brightfield image, together with erythrocytes and other cells associated with the colocated microvascular hemorrhage, as shown in Figure 2.1(a). The damaged cardiomyocytes specifically appear fluorescent red in the relatively high contrast fluorescence image as shown in Figure 2.1(b). In contrast, normal heart tissue appears grayer in the brightfield image and darker in the fluorescence image. The therapeutic ultrasound beam path projected onto the 2-D image is estimated from the lesion cloud as shown in Figure 2.1(b). Brightfield images were taken using auto exposure to provide morphologic information and fluorescence images were taken using a constant exposure to provide constant and quantitative lesion contrast information.

2.2.4 Cardiomyocyte Modeling

An average cross-sectional area (AC) for one cardiomyocyte sliced in a tissue section was estimated based on a mathematical model, which then gave an approximation of the number of stained cells by dividing the total injured area by the estimated AC

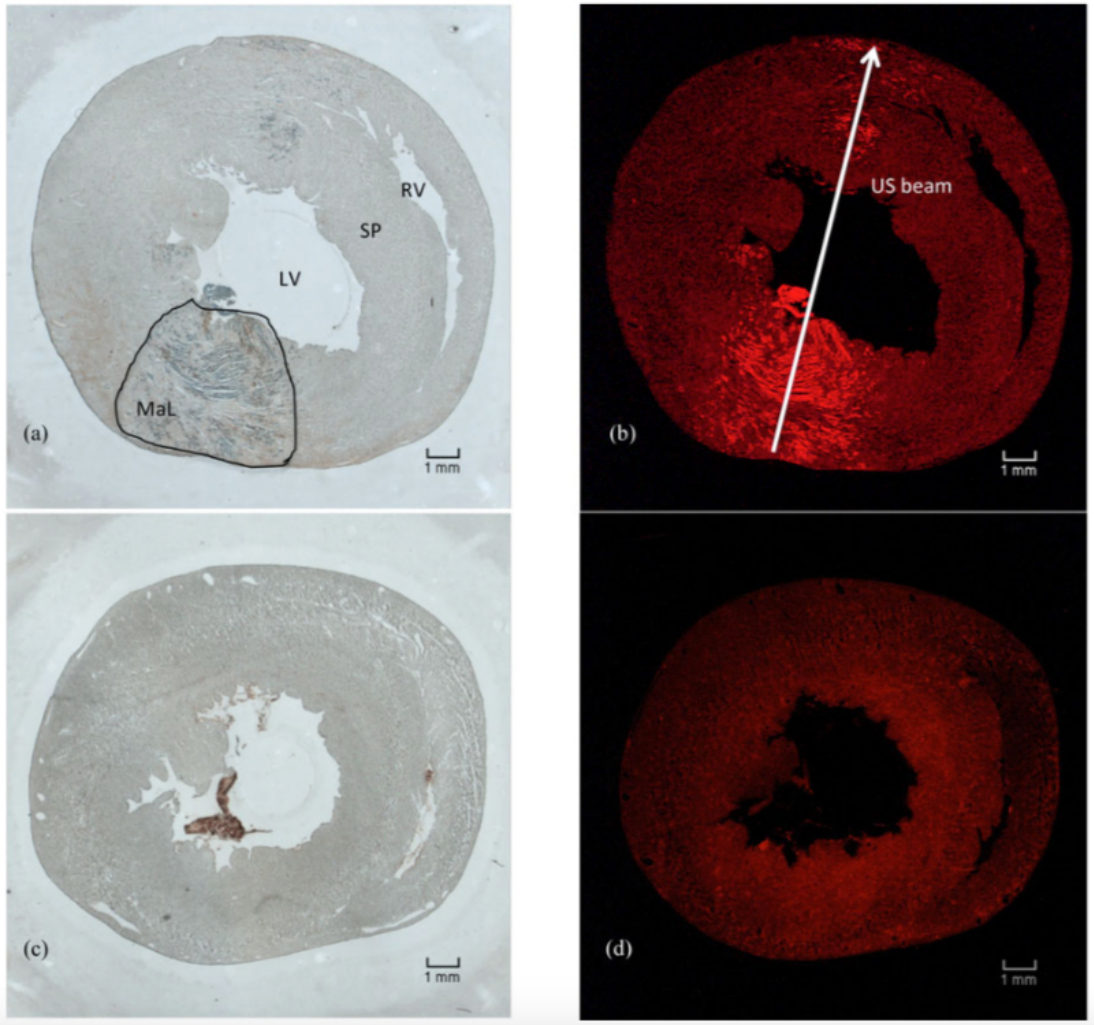

Figure 2.1: Evans blue staining indicated injured cardiomyocytes for microscope assessment as shown in (a) within an area noted by MaL (macrolesion), where also LV (left ventricle), RV (right ventricle), and SP (septum) are labeled. An example tissue section of treated heart muscle is shown in (a) brightfield and (b) fluorescence. The damaged cardiomyocytes in scattered microlesions appear stained light blue in the brightfield image, together with erythrocytes and other cells associated with the colocated microvascular hemorrhage, as shown in (a). The damaged cardiomyocytes specifically appear fluorescent red in the relatively high contrast fluorescence image as shown in (b). The therapeutic ultrasound beam trajectory indicated by the white arrow in (b) is estimated from the lesion cloud as described in the text (US: ultrasound). Similarly, (c) brightfield image and (d) fluorescence image of an example tissue section of a sham case are shown. The background fluorescence includes a few bright spots due to cell overlap, arterial walls, and other autofluorescent normal structures.

Table 2.1: Single cardiomyocyte geometry model

Parameter	Abbreviation	Value	Unit
Cell length	l	113.4±0.8	μm
Cell width	w	28.9±0.4	μm
Cell depth	d	17.6±0.4	μm

. A cardiac myocyte cell was geometrically modeled as an elliptic cylinder with cell dimensions summarized in Table 2.1 based on previous work (*Bassien-Capsa et al.*, 2006). The left ventricular wall comprises three strands of different longitudinal alignment: superficial (subepicardial) noted as S, middle noted as M, and deep (subendocardial) noted as D. The myocyte model approximated the superficial "layer" at an angle of 15° with respect to the long axis of the left ventricular inlet, occupying 25% of the wall thickness, the middle "layer" circumferentially arranged occupying 56% of the wall thickness, and the deep "layer" radiating longitudinally accounting for 19% of the wall thickness (*Ho*, 2009).

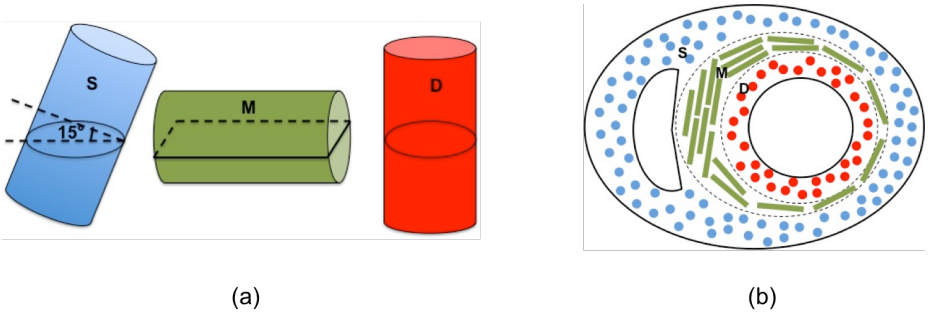

Figure 2.2: Illustration of a heart tissue slice plane intersecting with layers of the ventricular wall. (a) Schematic diagram for three elliptic-cylinder modeled cardiomyocytes oriented differently for each layer: blue for superficial (S), green for middle (M), and red for deep (D) layer. (b) Schematic diagram for the orientation of cardiomyocytes in each layer: blue for superficial (S), green for middle (M), and red for deep (D) layer.

As illustrated in Figure 2.2, a slice plane intersects with layers of different cell orientation, resulting in variable cross-sectional areas. The average cross-sectional cell area A_C is then given by Equation 2.1

$$A_C = \bar{A_S} P_S + \bar{A_M} P_M + \bar{A_D} P_D \tag{2.1}$$

where $\bar{A_S}$, $\bar{A_M}$, and $\bar{A_D}$ are average areas for the three layers: S, M, and D. P_S, P_M, and P_D are the fractional volume percentages of each layer for the overall wall thickness, namely $P_S = 25\%$, $P_M = 56\%$, and $P_D = 19\%$. For the superficial layer, we assumed that the cutoff plane did not reach the edge so that the cross section was always strictly an ellipse. Thus, cross-sectional areas for superficial and deep layers (Equation 2.2 and 2.3) were both considered as ellipses.

$$\bar{A_S} = \pi \cdot \frac{w}{2\cos 15^\circ} \cdot \frac{d}{2\cos 15^\circ} \tag{2.2}$$

$$\bar{A_D} = \pi \cdot \frac{w}{2} \cdot \frac{d}{2} \tag{2.3}$$

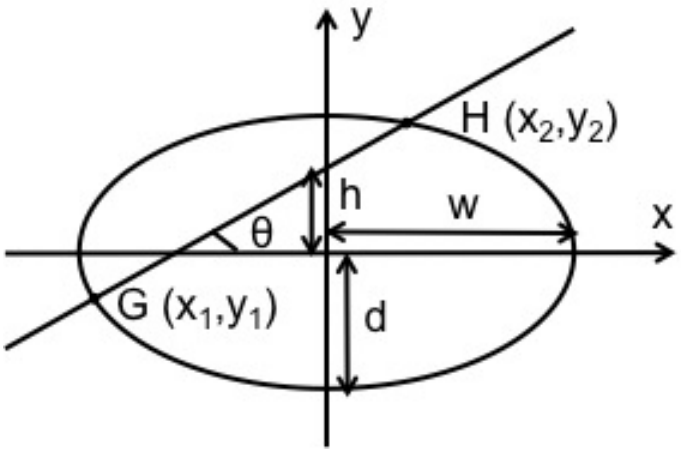

Figure 2.3: Top view of an elliptic cylinder cell intersected with the cutting plane at an angle of θ. The cutting edge is GH.

For the middle layer, the intersection plane was always a rectangle with length equal to l, and width GH as depicted in Figure 2.3 and determined by the orientation that the cutting plane intersects with the elliptic cylinder Equation 2.4,

$$\frac{x^2}{w^2} + \frac{y^2}{y^2} = 1 \tag{2.4}$$

with $-w \leqslant x \leqslant w$, $-d \leqslant y \leqslant d$, intersects with the cutting line Equation 2.5

$$y = \tan\theta \cdot x + h \tag{2.5}$$

with $0 \leqslant x \leqslant \pi/2$, $0 \leqslant y \leqslant h_{max}(\theta)$ at points $G(x_1, y_1)$ and $H(x_2, y_2)$, if and only if x,y have real solutions. For a certain cutting angle θ, the maximum value that h could achieve is when the cutting line is tangent to the ellipse. Thus, h_{max} is a function of θ. Thus, the length of the cutting edge GH, L_{GH}, is a function of θ and h as Equation 2.6

$$L_{GH}(h,\theta) = \sqrt{\left(x_1(h,\theta) - x_2(h,\theta)\right)^2 + \left(y_1(h,\theta) - y_2(h,\theta)\right)^2} \tag{2.6}$$

We assume that θ and h are uniformly distributed variables within their range, i.e. Equation 2.7 and 2.8

$$p(\theta) = \begin{cases} \frac{2}{\pi}, & 0 \leqslant \theta \leqslant \frac{2}{\pi} \\ 0, & \frac{2}{\pi} < \theta < 2\pi \end{cases} \tag{2.7}$$

$$p(h) = \begin{cases} \frac{1}{h_{max}(\theta)}, & 0 \leqslant h \leqslant h_{max}(\theta) \\ 0, & \text{otherwise} \end{cases} \tag{2.8}$$

where p indicates the probability density function for $p(\theta)$ and $p(h)$. The average cross-sectional area $barA_M$ in this case is Equation 2.9

$$\bar{A_M} = l \cdot \bar{L_{GH}} \tag{2.9}$$

where

$$\bar{L_{GH}} = \int_{\theta,h} L_{GH}(h,\theta)P(h,\theta)\mathrm{d}h\mathrm{d}\theta \quad = \int_{0}^{\pi/2}\int_{0}^{h_{max}(\theta)} L_{GH}(h,\theta)P(h,\theta)\mathrm{d}h\mathrm{d}\theta \tag{2.10}$$

Finally, given the previous relationships, an average cross-sectional area, $barA_C$, of 2,399 μm^2 can be computed. The pixel size for all 2-D digital images is 15.7 μm^2. Thus, one cell occupies approximately 2,399 $\mu m^2/(15.7\mu m^2/\text{pixel})$, that is 153 pixel in the acquired images. An approximation for the number of stained cardiomyocytes could then be inferred.

2.2.5 Lesion Characterization

To reduce computation complexity and save computation memory, the red channel, of all the data was first extracted. All the images were preprocessed to remove uneven illumination and zero padded ready for registration before feeding into the lesion characterization processing. Background illumination for both brightfield images and fluorescence images was estimated using a Gaussian low-pass filter (*Qu et al.*, 2012), that was then subtracted from the original images. The normalized images were processed following the steps shown in Figure 2.4. The main steps to characterize macrolesions include: 1) tissue detection; 2) microlesion detection; 3) image registration and 3-D stacking; 4) therapeutic beam estimation; and 5) macrolesion characterization.

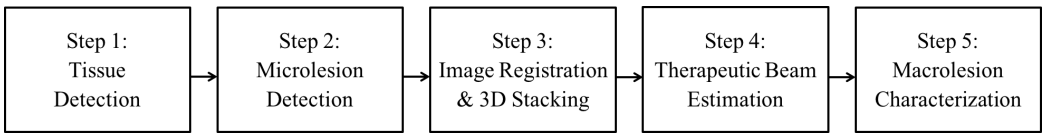

Figure 2.4: Flowchart for the overall method of macrolesion characterization.

Tissue detection and microlesion detection were first done based on 2-D images to form microlesion masks, which contain the morphologic information of the heart

as well as stained cell regions. Image registration was then performed on microlesion masks to reconstruct a volume-based model according to the morphology of the heart. The therapeutic beam was estimated from the 3-D stacked microlesions, and finally a macrolesion was characterized along the therapeutic beam.

Step 1: Tissue detection. The main objective in this step is to segment the tissue portion based on morphologic information from brightfield images to constrain the subsequent characterization. Brightfield images [see Figure 2.1(a) and (c)] were downsampled first to be segmented and then upsampled back after segmentation to decrease computational load. A threshold mask as shown in Figure 2.5(b) and an edge-detected mask as shown in Figure 2.5(c) were obtained simultaneously from a normalized brightfield image as the example shown in Figure 2.5(a), which was then fused together giving the tissue mask as shown in Figure 2.5(d).

Step 2: Microlesion detection. Starting with an initial guess of 10% for the lesion density, two lesion masks were obtained from thresholding brightfield and fluorescence images. An automatic threshold, described later, for the fluorescence image was then determined from the statistics of pixel values within the mutual mask of the two lesion masks. An example of a lesion mask on top of a zoomed original brightfield image Figure 2.6(a) is shown in Figure 2.6(b) illustrating the morphologies of the detected lesions.

Step 3: Image registration and 3-D stacking. To achieve volume-based characterization, 2-D lesion masks were stacked to 3-D according to the information provided through neighboring brightfield images from the tissue slide stack, i.e., by means of the transformation information from rigid image registration. Stacking registered mask images allows for visualization of the employed 3-D model as shown in Figure 2.7, where the red contour is rendering the tissue edges as resulting from step 1, and black marks symbolize microlesions detected in step 2. The inner red oval shape is the exclusion representing the in- ner surface of the LV. For the purpose to visualize the

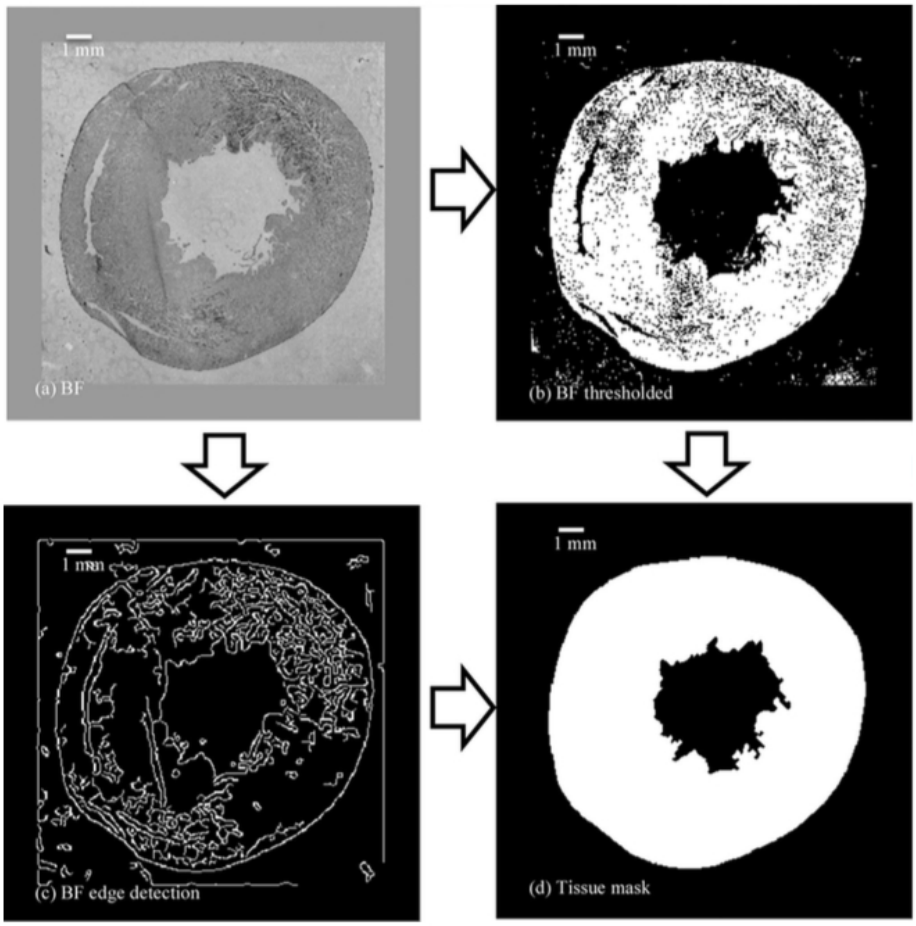

Figure 2.5: Threshold mask as shown in (b) and an edge-detected mask as shown in (c) were obtained simultaneously from a normalized brightfield (BF) image as shown in (a). Fusion of these resulted in the tissue mask as shown in (d).

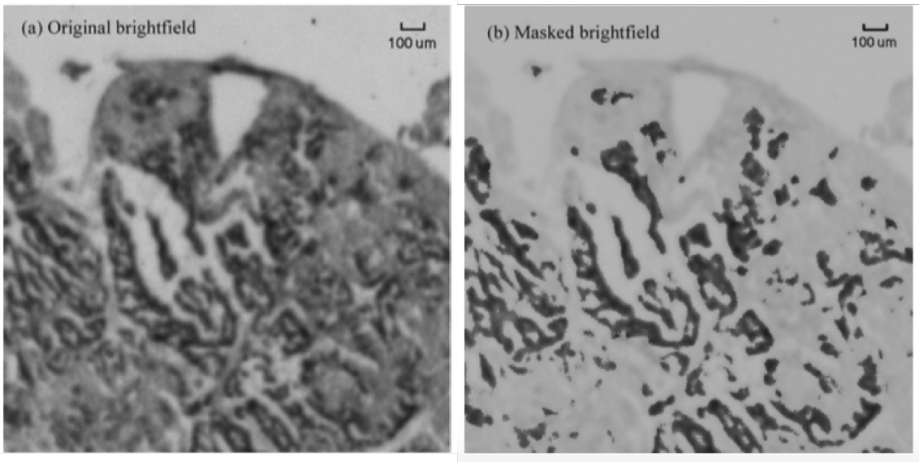

Figure 2.6: Automatic threshold for fluorescence image has been used to detect microlesions shown masked on the brightfield image in (b) compared to original brightfield image in (a). Note: images were zoomed in.

overall effect of treatment, high-resolution image showing the detailed morphology of individual cell is unnecessary; thus, 32 times downsampled microlesions symbolized by black marks are displayed representing the trend of lesion density. However, the full resolution is used for characterization.

Step 4: Therapeutic beam estimation. The therapeutic beam vector shown as a blue line with an arrow in Figure 2.7 was characterized by least square line fitting from the detected microlesions, excluding autofluorescing blood vessels and other nonmicrolesion microstructures, which were considered as noise.

Step 5: Macrolesion characterization. The stacked 3-D heart model was resliced along the therapeutic beam in 800-μm-thick steps. Note that the reslices here are not tissue-sections but slices perpendicular to the identified ultrasound beam. At each position along the beam axis, a disk was characterized as illustrated in Figure 2.8(a): each such slice was first populated with a 20-mm-diameter disk coaxial to the beam; each disk was then progressively reduced in size until a certain microlesion quantity was reached from a dynamic threshold, the criterion of which is explained below. Disks were characterized individually and then stacked together resulting in a final macrolesion as shown in Figure 2.8(b).

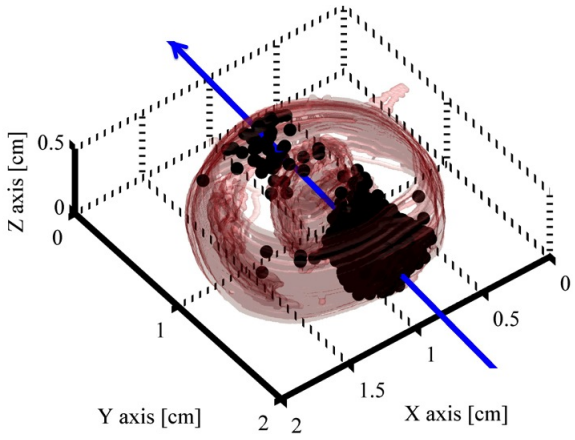

Figure 2.7: Three-dimensional stacking of registered image masks allows for visualization of the employed 3-D model, where the red heart tissue surface outline is rendered as a result from step 1 (tissue detection), black marks symbolize downsampled microlesions detected in step 2, and the therapeutic ultrasound beam (blue line) is characterized from least square fitting of the microlesion cloud (see text for more details).

To determine the dynamic radius mentioned earlier, a dynamic percentage value of overall stained cells within a maximum slice volume is computed. The threshold is a piecewise function of total number of stained cells and is shown in Figure 2.10. Here

$$p(h) = \begin{cases} \text{if} \quad N > N_0, \quad T = T_0; \\ \text{if} \quad N < N_0, \quad T = max(T_0(1 - e^{-N}), T_0), \end{cases} \tag{2.11}$$

where N indicates the total number of stained cells detected, N_0 is a cutoff threshold for piecewise function, and T indicates the percentage threshold for radius selecting with a constant T_0 as a maximum. As illustrated in Figure 2.9, the example here sets $N_0 = 30$, $T_0 = 95\%$.

The *in vivo* point spread function (PSF) of the therapeutic beam was characterized as a function of space by first sampling along the therapeutic beam interrogating coaxial cylinders of λ (1 mm) diameter and quarter λ length. Then, at the point of maximum axial lesion density, the lateral direction was sampled with coaxial rings of

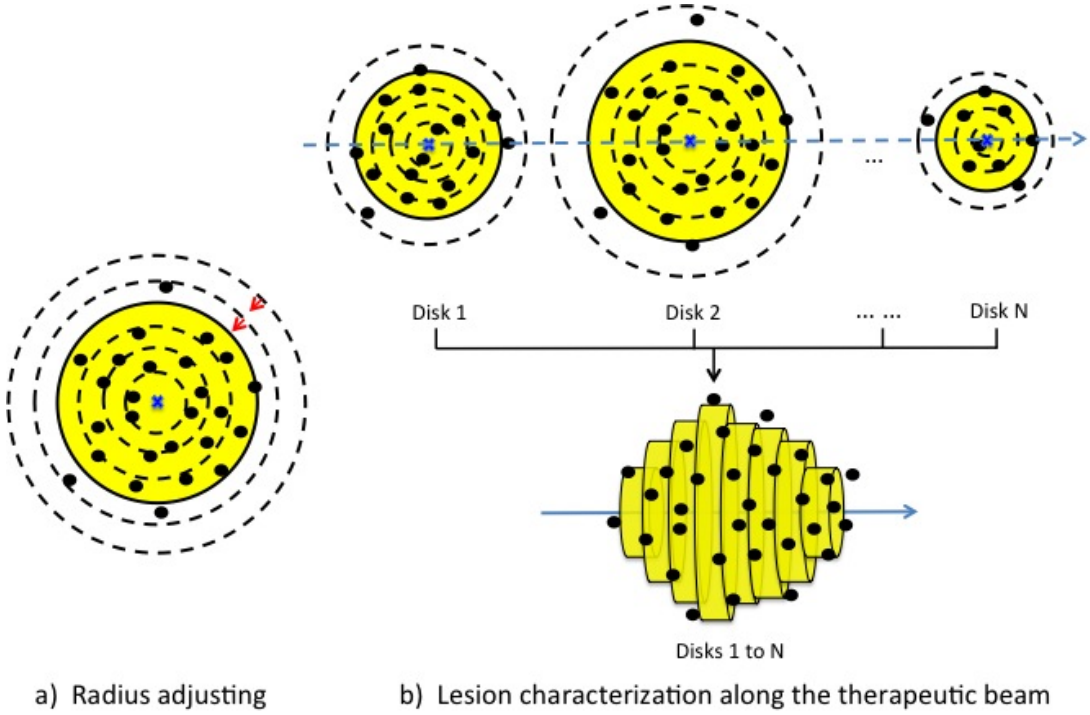

Figure 2.8: Schematic diagram of the procedure for macrolesion characterization. The stacked 3-D heart model was resliced along the therapeutic beam in 800-μm-thick steps. At each position along the beam axis noted by a blue "x, a disk was characterized as illustrated in (a). Each disk started with a 20 mm diameter and coaxial to the beam and is graphically identified as the most outer dash circle; the disk diameter was then progressively reduced as the red arrow implies until a certain microlesion quantity was reached from a dynamic threshold (see Fig. 9). The resulting disk then characterizes the local macrolesion slice and is shown in yellow, surrounded by black solid line. The yellow cylinder-like volume as in (b), *i.e.*, stacked disks, is defined as a macrolesion, characterized by a dynamic thresholding algorithm for counting enclosed microlesions for each disk step as illustrated in (a) (US: ultrasound).

one-eighth λ width and quarter λ height.

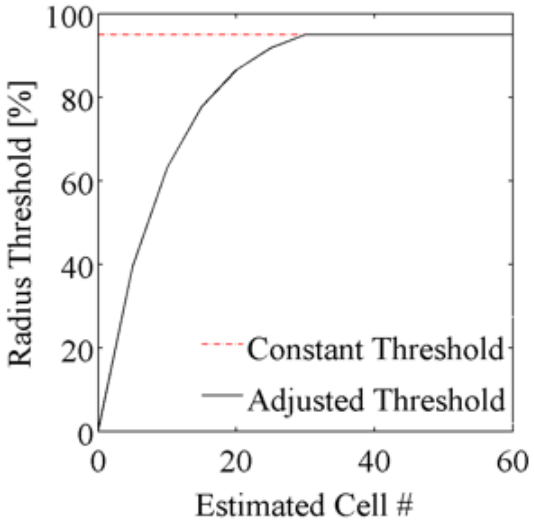

Figure 2.9: For a stained cell number cutoff threshold of 30, the auto adjusted threshold is plotted as a function of counted stained cells. If only 20 stained cells are counted within the current axial slice, then the macrolesion radius is set such that approximately 80% of the counted stained cells are enclosed.

2.3 Results

2.3.1 Lesion Visualization

A radially symmetric macrolesion was characterized via stepping disks of various radius determined by the local distribution of microlesions. An example is shown in Figure 2.10. An example of a 3-D macrolesion intersecting with one of the original 2-D microscopy images is shown in Figure 2.11 with a delineated boundary indicating macrolesion projection and tissue boundary characterized from brightfield tissue detection.

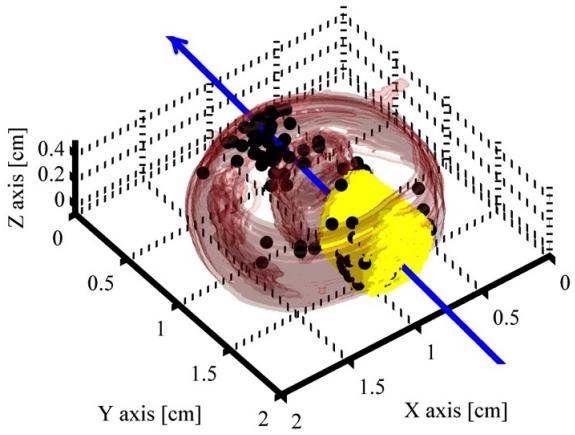

Figure 2.10: Characterized macrolesion visualization: the same as 2.7, additionally the resulting volumetric macrolesion is shown as yellow disks along the therapeutic beam. Note that it did not include the distal cloud of microlesions. The inclusion criteria were chosen to reject volumes with less than 10% microlesion density. In a chronic study, we plan to explore what microlesion density will cause significant tissue reduction.

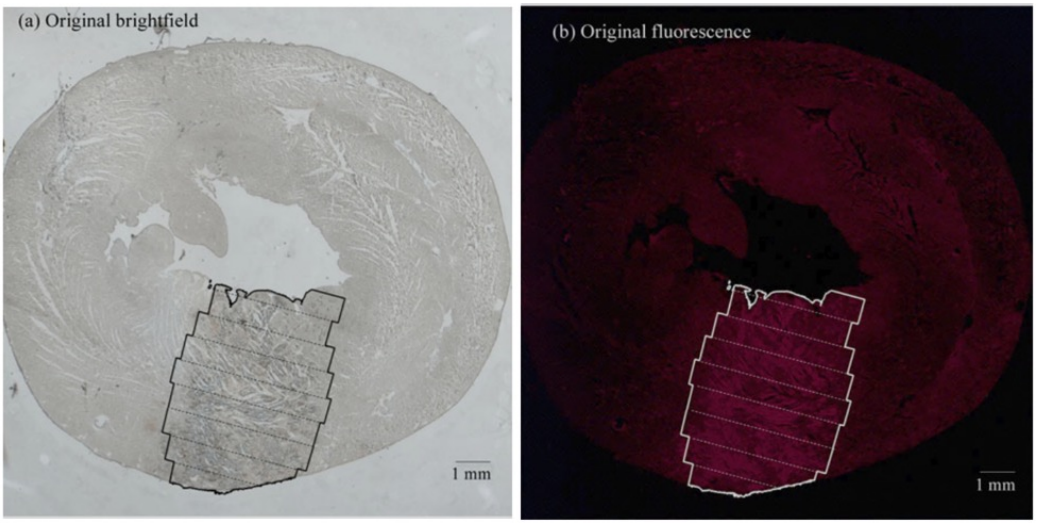

Figure 2.11: Example set of images showing the characterized macrolesion projected back onto its original 2-D microscopy images with dashed lines indicating stacked cross-sectioned cylinders and tissue boundary derived from brightfield tissue detection.

2.3.2 Group Comparison

As described in a concomitant study (*Miller et al.*, 2014a), the treated group of rats was subdivided into three groups, with five rats in each group. They were treated at three different time points of the cardiac cycle: at the onset of R wave (RR, end diastole), at the R wave plus one-third of the R to R interval (RR/3, end systole) and at the R wave plus two thirds of RR (2RR/3, mid- diastole). Results for macrolesions characterized for all 20 rats are presented in Figure 2.12 using boxplots. For each box, the central mark is the median, the edges of the box are the 25th and 75th percentiles, the whiskers extend to the most extreme data points not considered outliers, and outliers are plotted individually. The normal range was defined as greater than $q_3 + 1.5(q_3 - q_1)$ or smaller than $q_1 - 1.5(q_3 - q_1)$, where q_1 and q_3 are the 25^{th} and 75^{th} percentiles, respectively. Corresponding median values for treated groups are reported in Table 2.2. The results show no significant variation between treated groups, which agree with the visual scoring results from the concomitant study. The summarized results for the treated group of 15 rats compared to sham group show significant macrolesions with a median volume of 87.3 μL of 14.0% lesion density, 2.7 mm macrolesion radius, and 4.8 mm macrolesion length compared to zero lesion density, radius, and length for the sham group. This overall result was consistent with the measurements of troponin, which were also indicative of total cardiomyocyte necrosis.

2.3.3 Point Spread Function

The *in vivo* PSF of the therapeutic beam in terms of lesion density was characterized for one rat affected by an extreme long therapeutic path through the myocardium, as shown in Figure 2.13.

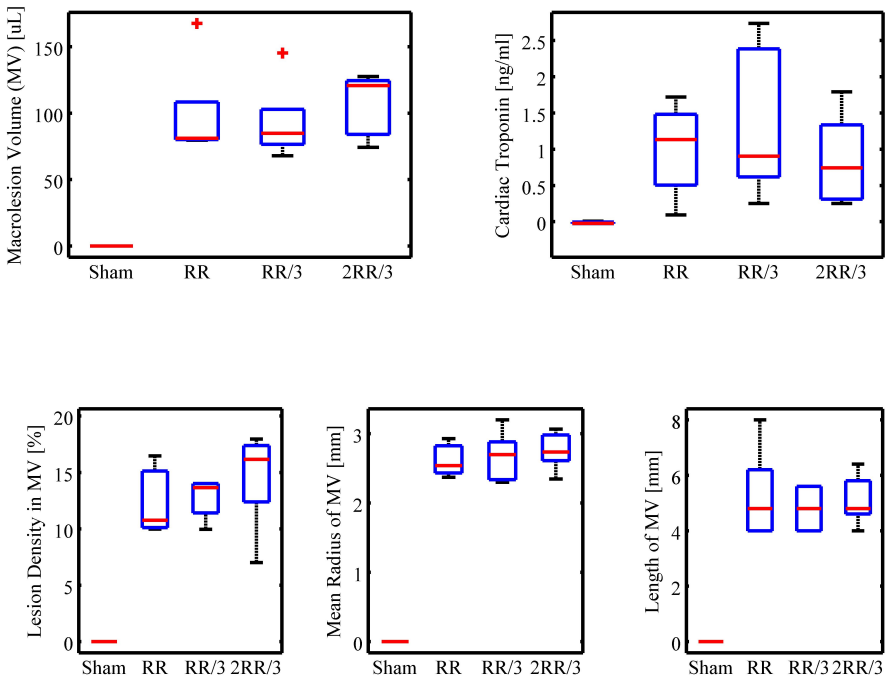

Figure 2.12: Characterized features of macrolesions are compared to the measurement of troponin I in plasma samples taken one day after the treatment. The treated group was subdivided into three subgroups being treated at different time points of the cardiac cycle: R wave (RR, end diastole), R wave plus 1/3 of the R to R interval (RR/3, end systole), and R wave plus 2/3 of the R to R interval (2RR/3, mid-diastole).

Table 2.2: Summary of results. Median values summarized for Figure 2.12 for sham group, treated group, (RR, RR/3, 2RR/3) of five rats in each at different exposure time with respect to a cardiac cycle and all treated rats of 15.

	Sham(5)	RR(5)	RR/3(5)	2RR/3(5)	Treated(15)
Macrolesion volume [μL]	0	81.1	84.8	120.7	87.3
Cardiac troponin I [ng/mL]	0	1.1	0.9	0.7	0.9
Lesion density in macrolesion volume [%]	0	10.8	13.7	16.2	14.0
Mean radius in macrolesion volume [mm]	0	2.5	2.7	2.7	2.7
Length of macrolesion volume [mm]	0	4.8	4.8	4.8	4.8

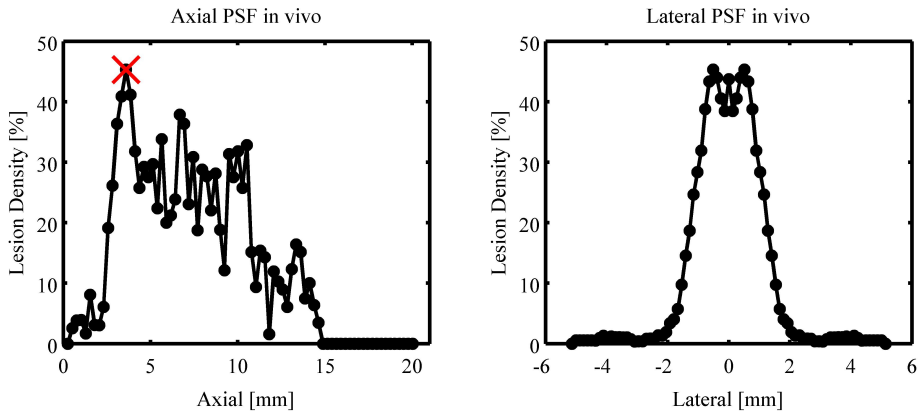

Figure 2.13: *In vivo* PSF of the therapeutic beam as assessed in terms of lesion density along the axis of the treatment transducer. Top: lesion density within macrolesion along the therapeutic beam axis; bottom: lateral cut through macrolesion at axial maximum (indicated as an x on the top).

2.4 Discussion

This computer-aided histological evaluation appears to provide robust characterization of the macrolesion formed by the accumulation of microlesions based on the following considerations.

2.4.1 Therapeutic Beam Estimation

Occurrence of cavitation events induces the here observed damage to cardiac myocytes. It is expected that the lesion density would be uniform within the beam profile, where the acoustic pressure exceeds the cavitation threshold, assuming that the contrast agent in the myocardium is uniformly distributed. However, lesion uniformity could be disrupted by variable superthreshold acoustic pressures, which may injure more than one cell per cavitation event. Hence, we expect the lesion density trend of the microlesion to be dictated by the acoustic beam profile as well as processes involving motion of the myocardium. For example, breathing motion leads to smearing out the accumulation effect of the treatment, which then is not shaped strictly according to therapeutic beam. Thus, in turn, the therapeutic beam estima-

tion is affected. A decreasing trend of the lesion density was observed along the axial direction, possibly due to acoustic attenuation caused by contrast agents in the LV. The lateral PSF profile was obtained at the maximum of the axial response, which was regarded as the volume of interest of the therapy. The *in vivo* PSF -6 dB lateral width of approximately 2.8 mm agrees reasonably with the 3.5 mm beam diameter of the therapy transducer as obtained from a free-field water tank calibration. The i*n vivo* lateral beam width may be affected by aberration dis- tortion of the sound wave propagating through overlying tissue layers, thus narrowing the beam diameter with pressure amplitudes above the threshold required for cavitation. Additionally, acoustic attenuation will reduce the *in situ* pressure amplitude and also narrow the beam cross section containing pressure amplitudes required for microlesion creation.

2.4.2 Cardiomyocyte Model Validation

A total of 160 manually selected cells according to the morphology appearing in brightfield images were taken an average to obtain estimation of area for a cell of 2,719 μm^2 versus 2,398 μm^2 from the theoretical geometric model. The 12% deviation of the estimation model from the selected estimation comes from bias on selecting large identifiable cells on the manual side and the variation from the cell orientation from the modeling side.

2.4.3 Cardiomyocyte Cell Scoring Validation

The Evans blue staining found in frozen sections, one day after therapy, identifies lethally injured cells resulting from microlesions (*Miller et al.*, 2005b), (*Vaezy et al.*, 2001). Therefore, the total determination of the macrolesion as a fraction of the tissue volume provides a first approximation to the amount of tissue reduction expected from the treatment. The desired reduction would be about 20%, which could be expanded beyond the single focus treatment described here by moving the

beam to provide the needed therapeutic reduction in larger (i.e., human) hearts. The simple visual scoring of the stained cells provides only a qualitative measure of the microlesion effect, particularly for high densities of microlesions seen in the treatments intended for therapeutic tissue reduction, which only approximate the more accurate image analysis values (see Figure 2.14). In addition, the qualitative visual scores fail to give a total fractional reduction throughout the treated volume, which is provided by the reconstruction of the volume and the macrolesion determination. The cell identification scheme counts pixels rather than cells assuming an overall constant statistical mean multiplier for pixel to cell size conversion, by which the pixel counting and subse- quent area to number of cells conversion is independent of the at times complicated cell morphology. The automatic scheme of stained cell identification seems reasonable compared to visual scoring as shown in Figure 2.14. The cases of large accumulations of stained cells were often difficult to score visually resulting in qualitative results rather than actual cell count. In contrast, the proposed computer-based characterization method is objective and quantitative and overcomes the limitation of large number of cells.

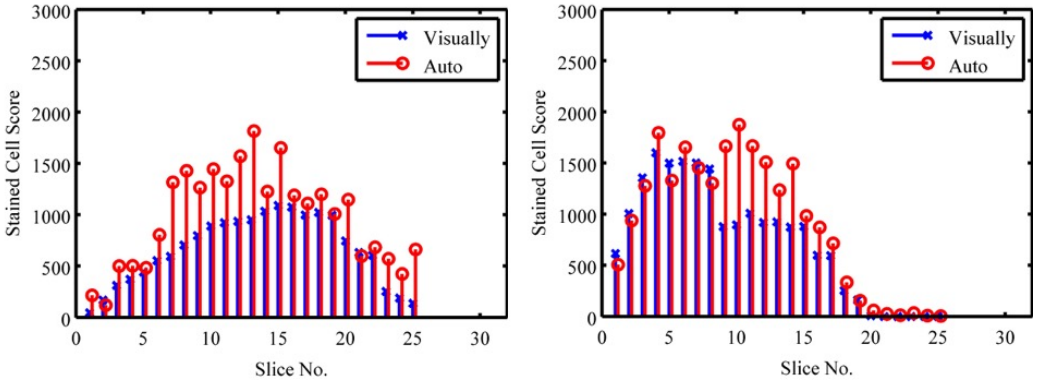

Figure 2.14: Two examples of comparison on visual cell scoring and automatic scoring derived from the proposed computer-based quantification method with the cardiomyocyte model. The proposed method gives an area-based estimation of stained cell number instead of a subjective judgment based on microlesion morphology.

2.4.4 Lesion Characterization Criterion

The volume estimation of macrolesions considered local le- sion density as well as total lesion number. Additionally, a dynamic radius cutoff criterion was used that depends on the number of the stained cells. Using a constant threshold for stained cell intensity would not affect the shape of a well-generated dense lesion due to the large number of microlesions in the macrolesion volume, but would affect a sparse macrolesion due to its low number density of microlesions. Thus, a dynamic threshold was introduced.

2.5 Conclusion

A computer-aided 3-D objective evaluation scheme has been developed to characterize macrolesions, including lesion size and lesion density, for MCET to reduce myocardial tissue, based on brightfield and fluorescence images as available in acute preclinical studies. The radially symmetric model employed to characterize macrolesion density is feasible for the study using a single focused beam. This methodology reduces visual scoring ambiguity and provides a volume oriented, quantity- sensitive therapy evaluation. The significance of characterized macrolesion compared to sham group demonstrates that the evaluation scheme is robust against noise. Future implementations of MCET involve formulating a set of optimized treatment parameters to create a desired total volume reduction based on lesion density within the target volume. In particular, we are interested in the microlesion density and macrolesion size, as both determine the anticipated myocardium reduction. The proposed evaluation scheme could possibly assist quantifying other therapeutic applications resulting in sparse effects, such as drug delivery, gene therapy, and blood brain barrier opening.

CHAPTER III

Quantitative Assessment of Damage During MCET: A Parametric Study in a Rodent Model

3.1 Introduction

Hypertrophic Cardiomyopathy (HCM) is a common genetic cardiovascular disease, which is usually clinically recognized by a maximal left ventricular wall thickness greater than 15 mm (*Gersh et al.*, 2011). This globally prevalent disease, reported in about 0.2% (i.e., 1:500) of the general population, is the most frequent cause of sudden death in young people and can lead to functional disability from heart failure and stroke *Maron and Maron* (2013). The traditional treatment for Hypertrophic Cardiomyopathy (HCM) to reduce myocardium is septal myectomy. This surgical method removes septal hypertrophy, which possibly leads to perturbation of mitral valve leaflets *Marian* (2009). An innovative therapeutic scheme, named Myocardial Cavitation Enabled Therapy (MCET), has been proposed as a means to achieve minimally invasive myocardial reduction by cavitating contrast agent microbubbles with ultrasound to produce a fractional macrolesion containing sparse and histologically definable microlesions *Miller et al.* (2014a). There are several ways of controlling cavitation here. Cavitation is enabled by the injection of ultrasound contrast agents. These will enable cavitation only in the focal region of the transducer and thus only

there lead to microlesion formation in the myocardium. Second, ultrasound cavitation is dependent on sound pressure amplitude. In vivo experiments reveal that cavitation-induced lesions take place at peak rarefactional pressures larger than 2 MPa as obtained under free field conditions. In this case ECG is monitored for premature complexes. It has been seen that the occurrence of premature complexes is directly correlated with cavitation events *Miller et al.* (2011).

As a potential tissue reduction therapy, Myocardial Cavitation-Enabled Therapy (MCET) avoids open-chest surgery and is hypothesized to allow healing with minimal scar formation, resulting in shrinkage of the cardiac treatment volume. This ultrasound microbubble-enabled method additionally provides the possibility of guiding and monitoring via quantifying feedback from the microbubble emissions.

To optimize MCET ultrasound parameters and administration of microbubble settings, assessment of the therapeutic effect is needed to assist parameter adjustment. Efforts in computerized analysis have been made to aid diagnostics and therapy for being fast, objective and quantitative. Methods have been developed for computed tomographic angiography for the purposes of detecting heart diseases (*Zhou et al.*, 2012)(*Bouraoui et al.*, 2010) and for quantification of coronary arterial stenosis (*Xu et al.*, 2012). Automatic detection of pulmonary embolism has also been used in CT angiography (*Zhou et al.*, 2003) (*Bouma et al.*, 2009). Quantitative ultrasound has been employed in diagnosis of osteoporosis (*Moayyeri et al.*, 2012), as well as in at-risk pregnancies with three-dimensional sonographic measurement of blood volume flow in umbilical cords (*Pinter et al.*, 2012). Three-dimensional high-frequency ultrasound data also has been processed to offer a quantitative evaluation of cancerous lymph nodes at the microscopic level (*Mamou et al.*, 2010).

For MCET, a quantitative method for assessing the distribution and total accumulation of myocardial necrosis based on Evans blue-stained cells in the tissue histology slices was developed previously (*Zhu et al.*, 2015a) and is used in this study.

This chapter investigates the tuning of various parameters involved in MCET and paves the way for pre-clinical treatment planning of myocardial lesion creation and properties thereof, in a quantitative manner.

One important and practical aspect of MCET is managing the buildup of microlesions and macrolesions to achieve a desired amount of myocardium reduction in larger pre-clinical models as well as, ultimately, in the clinic. Acoustic pressure amplitude, contrast dose and treatment duration are adjustable variables. The parametric exploration of various conditions will assist in the search for feasible treatment conditions that allow for fast lesion creation with a 15-20% microlesion density and a large axial and lateral dimension. Another desirable factor for practical clinical implementation is the treatment efficiency. Instead of treating a single focal spot as done in our previous study (*Miller et al.*, 2014a), a scanned beam would allow for a more rapid accumulation of lesions in a larger target treatment volume.

Our method of computer-aided histology analysis was developed using relatively high exposure parameters to reflect therapeutic treatment conditions (*Pinter et al.*, 2012). This provided a means to reconstruct the tissue volume containing microlesions and their distribution, which can then be integrated to yield the potential fraction of tissue reduction. For validation, a visual scoring method was used in tandem, in which lethally injured cells indicated by fluorescent staining in frozen sections were counted. The visual method has been the gold standard for quantifying cell death by counting the absolute number of stained cells. However, when the number of stained cells becomes large, as for treatment (rather than exploring bioeffects), the visual method becomes a qualitative scoring method, which was suspected to yield inaccurate results for the validation for the computer-aided method. The purpose of this study was to analyze several exposure groups, which had reduced, sub-therapeutic treatment effects, using quantitative visual scoring for comparison to the computer-aided analysis.

3.2 Methods and Materials

3.2.1 Experimental Conditions

To make MCET amenable to clinical translation, the evaluation of B-mode echogenicity (more generally backscatter), physiological responses, *i.e.* premature complexes and visual scoring (*Miller et al.*, 2015) is employed. For this study tissue samples were collected and prepared for histological evaluation. Specifically, these samples underwent quantitative analyses aimed to assist the treatment planning. *In vivo* animal procedures were conducted on fifty male Sprague-Dawley rats (Charles River, Wilmington, MA, USA) including five sham rats weighing 352 ± 30 g. Approval and guidance of all animal work was done by the University Committee on Use and Care of Animals. All rats in the treated group were injected with Definity®(Lantheus Medical Imaging, Inc., N. Billerica, MA) at a rate of 5 or 12.5 $\mu L/kg/min$. Microbubbles suspended and diluted in sterile saline were infused via a tail vein or jugular vein catheter (gauge # 24) starting 15 seconds before ultrasound exposure and concluding with the end of exposure. MCET was performed with ultrasound bursts of five cycle pulses at a center frequency of 1.5 MHz and a pulse repetition frequency of 4 kHz. The ultrasound exposure system consisted of a function generator for generating a pulse train (model 3314A function generator, Hewlett Packard Co., Palo Alto CA), an arbitrary waveform generator for amplitude modulation of the pulse train (model 33220A, Agilent Technologies, Loveland CO), a power amplifier (A-500, Electronic Navigation Industries, Rochester NY) and a 1.5 MHz single element therapy transducer (Panametrics A3464, Olympus, Waltham, MA). The therapy transducer was a standard single-element focused transducer, with a 1.9 cm diameter and 3.8 cm focal length. The treatment was targeted with the aid of diagnostic ultrasound imaging (GE Vivid 7 with S-10 phased array, GE Healthcare, Jupiter FL, USA) operated at 10 MHz with a 5 cm focal depth, as previously described (*Miller et al.*, 2015).

The setup scheme as illustrated in Figure 3.1 provided targeting of the therapy beam and for low-power imaging of the heart during exposure. The imaging array and therapeutic transducer were fixed at a 37° angle such that the acoustic axis of the therapy transducer is parallel with one image line of the sector array. This image line was identified in a water tank using a line target and marked on the screen of the ultrasound scanner. Then this image line was used to evaluate acoustic access to the left ventricular wall. Subsequently the transducer/probe gantry was translated such that the therapy transducer beam aimed along the same fixed path as the image line identified in the image to pass through the window between the ribs (vertical axis) and between the sternum and the left lung. Burst emissions were triggered from the ECG signal at every four heartbeats end-systole. Prior to ultrasound exposure, all rats were injected with Evans blue, a reliable histological stain for lethal injury of cardiomyocytes (*Miller et al.*, 2015).

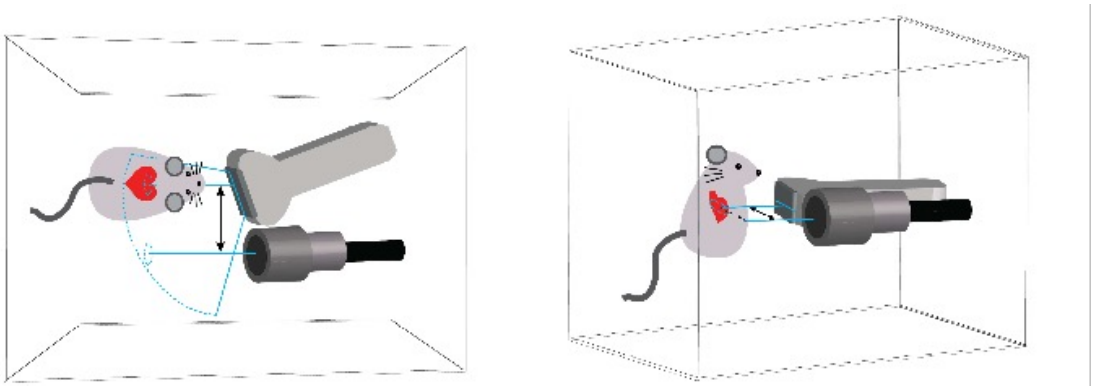

Figure 3.1: Schematic illustration (top view and side view) of the experimental setup. The imaging array and therapeutic transducer were fixed at a 37° angle so the acoustic axis of the therapy transducer was parallel with a specific image line of the sector array. This image line was identified in a water tank using a line target and marked on the screen of the ultrasound scanner. This image line was then used to warrant the acoustic access to the left ventricular wall. Subsequently, the transducer/probe gantry was translated so the therapy transducer beam followed the same path as for the previously identified image line.

The study was conducted with groups of five rats each and given letter designa-

Table 3.1: Table of sets of conditions used for respective groups of rats, with a cohort of 5 animals each. Group F acted as a sham and calibration group, as described in the text.

Group ID	Infusion Site	Pressure (PRPA)	Modulation	Infusion Rate	Treatment Duration
A	Tail	4 MPa	Square	5 μL/kg/min	5 min
B	Jugular	4 MPa	Square	5 μL/kg/min	5 min
C	Jugular	4 MPa	Square	5 μL/kg/min	5 min
D	Jugular	4 MPa	Gaussian	5 μL/kg/min	5 min
E	Jugular	4 MPa	Gaussian	12.5 μL/kg/min	2 min
G	Tail	2 MPa	Gaussian	5 μL/kg/min	5 min
H	Tail	2.8 MPa	Gaussian	5 μL/kg/min	5 min
I	Tail	4 MPa	Gaussian	5 μL/kg/min	100 s
J	Tail	4 MPa	Gaussian	5 μL/kg/min	30 s

tions to identify the specific set of conditions in each group. Groups A to J were designed specifically to test treatment effects for different parameters, as listed in Table 3.1. Except for Group G and H, all rats were exposed to ultrasound with a peak rarefactional pressure amplitude (PRPA) of 4 MPa. The pulses in the center of the focal region were measured in a water bath using a calibrated hydrophone with a 0.2 mm diameter aperture (model HMA-0200, Onda Corp., Sunnyvale, CA) to acquire the point spread function and the electro-acoustic transfer function. Comparison of groups A and B tested the influence of catheter placement, with the jugular vein giving a central and larger vein access than the tail vein. Groups B and C were compared to test the effect of aiming ultrasound near ribs. Those two comparisons were performed intentionally to test experimental perturbations.

Groups B and D compared the results of treatment using square versus Gaussian pulse train modulations of the acoustic pressure. The single element transducer delivered a Gaussian envelope pulse train, such that the full-width half maximum of the Gaussian modulation was 2 ms. This modulation scheme was to simulate an exposure that would be experienced by contrast agent in the presence of a sweeping ultrasound beam, as found in a diagnostic imaging setup (*Miller et al.*, 2007). To reduce treat-

ment times for larger treatment volumes such a beam could be implemented as a sweeping therapy beam and is thus included in the tested exposure conditions. Note that only the pulse train envelope is Gaussian modulated. Each individual pulse is a constant amplitude five-cycle tone burst (see Figure 3.2). The amplitude modulation was set to give zero exposure unless a modulation-envelope signal was triggered. The envelope signal was either a 2 ms square pulse with a constant amplitude of 4 MPa PRPA or a Gaussian modulation function that produced a 2 ms pulse with amplitudes greater than 2 MPa PRPA. The Gaussian modulation was designed to emulate a scanned ultrasound beam from a clinical ultrasound scanner, with approximately 56 frames per second (fps).

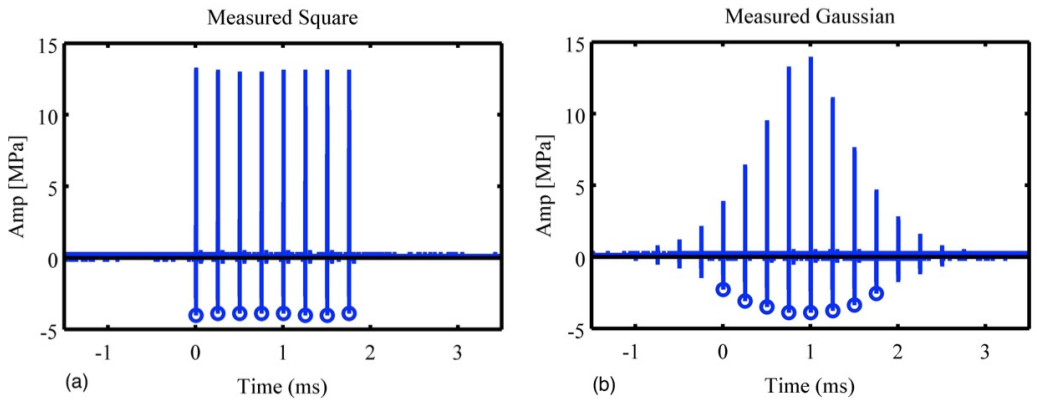

Figure 3.2: Employed electric pulse train excitations. Circles in square modulation (a) and Gaussian modulation (b) pulse trains indicate the employed negative pressure amplitudes. Note that each spark is a 5-cycle 1.5 MHz tone burst.

Different contrast agent dose rates were tested by comparing Groups D and E. The previous rate was 5 μL/kg/min, representing the recommended dose for diagnostic applications (*Miller et al.*, 2014a). A higher infusion rate of 12.5 μL/kg/min was tested for the possibility of using a higher dose in therapeutic applications, which may reduce treatment durations.

Comparison between Groups G, H and D evaluated the dependence of lesion formation on acoustic pressure. The three groups were respectively exposed to ul-

trasound fields of 2, 2.8 and 4 MPa PRPA. Groups J, I and D, on the other hand, evaluated microlesion accumulation by varying the treatment duration, *i.e.* adjusting the contrast infusion duration. Groups G, H, I and J were specifically treated with sub-therapeutic parameters with reduced treatment impact on cell survival. Correlation between acoustic pressure, treatment duration and induced microlesion density was intended to establish some dynamic range for microlesion induction.

Finally, Group F was a sham and calibration control group, in which each rat received the full 4 MPa therapy exposure before the contrast agent infusion started.

Results in groups are presented in boxplots. For each box, the central mark is the median, the edges of the box are the 25th and 75th percentiles, the whiskers extend to the most extreme data points not considered outliers, and outliers are plotted individually. The normal range was defined as $q_3 + 1.5(q_3 - q_1)$ or smaller than $q_1 - 1.5(q_3 - q_1)$, where q_1 and q_3 are the 25^{th} and 75^{th} percentiles, respectively.

3.2.2 Cardiomyocyte Scoring

Rat hearts were harvested and scored one day after exposure as described in previous work (*Miller et al.*, 2015). Briefly, up to forty 10 μm thick frozen sections were made from the treated volume in each heart. A quantitative method for assessing the distribution and total accumulation of myocardial necrosis is based on Evans blue-staining and was developed previously (*Zhu et al.*, 2015a). Microlesions were identified by fluorescence microscopy and photographs of each section. Image registration was then performed to digitally stack the frozen sections in 3D and to reconstruct a model of the heart morphology in the entire sampled region showing the three-dimensional distribution of microlesions. The microlesion fraction of the tissue within the focal zone was calculated to estimate the potential fractional volume of tissue reduction that was achieved. Quantitative results were characterized in terms of microlesion volume, macrolesion volume, microlesion lesion density and dimensions of the radially

symmetric approximated macrolesion.

In addition to the computer-aided assessment, traditional visual scoring was used to evaluate myocardial necrosis qualitatively by visual identification and quantitatively by scoring of Evans blue-stained cells using fluorescence microscopy (*Miller et al.*, 2015). Automatic scores were obtained from dividing the geometric microlesion volume by a constant conversion factor acquired from a geometry based cardiomyocyte model (*Zhu et al.*, 2015a).

3.2.3 Therapeutic Field Simulation

The acoustic field, assuming a water path, for the employed single element therapeutic transducer was simulated in FIELD II (*Jensen and Svendsen*, 1992), a widely used ultrasound simulation program. A 1.9 cm diameter concave single element transducer with 3.8 cm focus excited at 1.5 MHz with a 5-cycle burst was modeled. The time period between two successive bursts being 250 μs apart (4 kHz pulse repetition frequency (PRF)) were significantly larger than the 3 μs indivisual pulse length. Thus they were considered to have no interference on each others acoustic field. Figure 3.3 (a) shows a normalized field reflecting the maximum exposed pressure during one burst. The effective region of sound pressures with amplitudes above the acoustic pressure threshold of 2 MPa is indicated in Figure 3.3 (b). By revolving this shown region along the lateral (x=0 mm) axis, the effective volume, denoted as an axisymmetric rotational model, was calculated. This simulation intended to associate *in situ* acoustic field with the formed lesion.

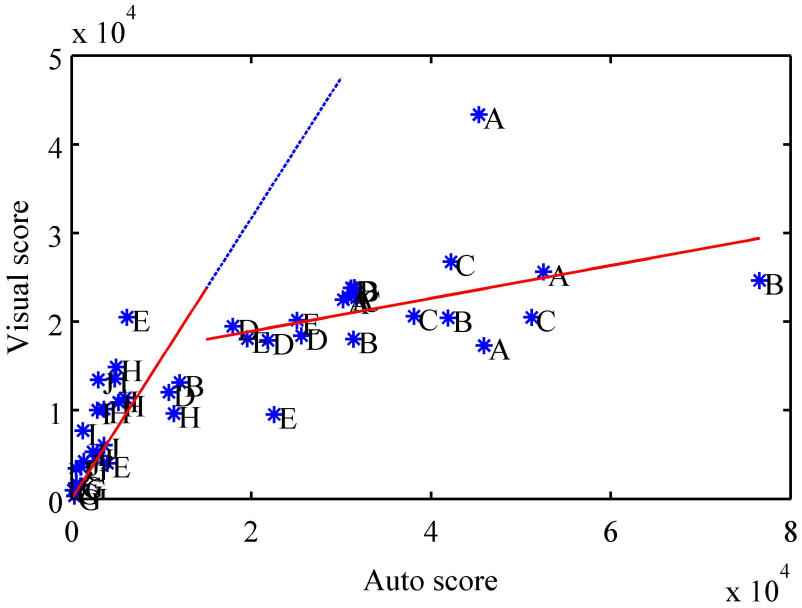

Figure 3.3: Scatter plot showing comparison of visual score versus auto score. The auto score was obtained from a computer-aided method (*Zhu et al.*, 2015a) with piece-wise least square fitting at a break point for the auto score equal to 15,000. Visual scoring correlates best with auto scoring for fewer lesion counts, which reveals the difficulty to assess large number of lesions quantitatively by visual means.

3.3 Results

3.3.1 Quantitative Computer-Guided Lesion Analysis

The previous study (*Miller et al.*, 2014a) was limited by a low dynamic range with respect to the number of induced lesions. Current results span a large range of number of lesions per area on histology, which therefore allows for a more critical evaluation of the performance comparison between visual and automatic scoring. Data presented in this study reach to tens of thousands of lesions, a range that is difficult to assess quantitatively by traditional visual scoring. Figure 3.4 shows visual scores plotted versus auto scores (obtained from computer-aided algorithm) for all groups listed in Table 3.1. The data can be segmented in two regions: low counts ranging from 0 to 15,000 and high counts from 15,000 to 80,000 (both with respect to the auto score), respectively. A linear least square fit of the form $y = a_1 \cdot x$, was performed for the low lesion count segment and is shown in red and extended as blue in Figure 3.4. Another linear least square fit, now of the form $y = a_2 \cdot x + b$, was performed for the high lesion count segment and is shown in red in Figure 3.4. Best-fit coefficients were found as: $a_1 = 1.52$, $a_2 = 0.19$; and b=15,216, with a_1 greater than 1 would mean that visual scoring counted more cells, a_2 being so low shows that visual scoring counted groups of cells as one. This result clearly showed the "saturation" effect of the visual scoring method for high cell counts.

3.3.2 Acoustic Pressure Dependence

3.3.2.1 Macrolesion volumes

Macrolesion dimensions are in part dictated by the therapy beam geometry as illustrated in Figure 3.5. Lesion lengths (axial) and lesion diameters (lateral and elevational) are determined by the point spread function of the therapy transducer and the acoustic pressure of the transmitted wave. In other words, the volumetric

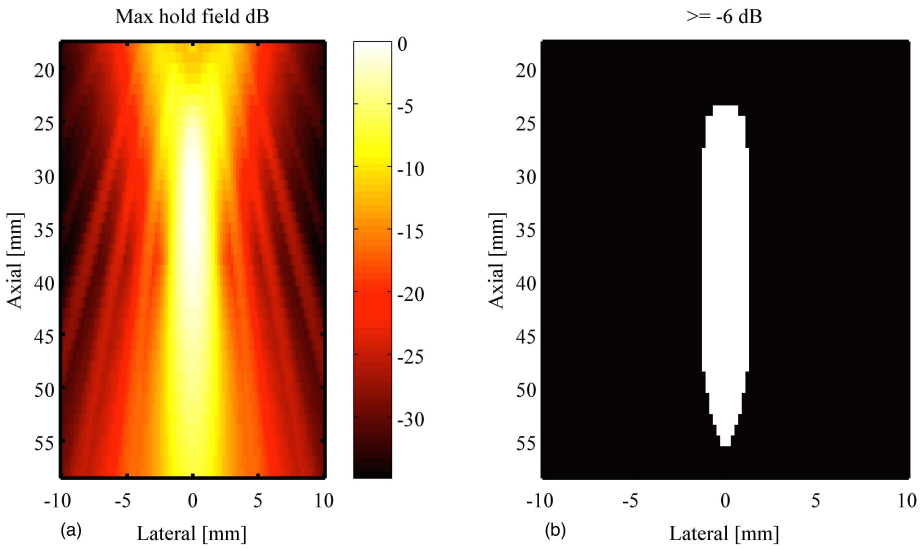

Figure 3.4: Therapeutic ultrasound transducer field simulation. (a). FIELD II simulation of pressure distribution for free field single element therapy transducer. (b). Lesion formation based on the lesion-pressure dependence; volume narrows the region of lesion formation to where peak negative pressure is above 2 MPa, *i.e.* greater than the lesion formation pressure threshold. The acoustic pressure field representing the expected lesion region is 2.5 × 32 mm at the level of -6 dB relative to 4 MPa.

region of the acoustic wave that bears pressure amplitudes above the pressure p_L required for lesion formation, will contribute to the therapy. This volumetric region grows as the pressure amplitude at the focus grows and thus larger acoustic pressures yield larger lesion count. Macrolesion dimensions are also dictated by the spatial availability of cells and contrast agent. The simulation gave an acoustic field of 2.5 × 32 mm at the level of -6 dB relative to 4 MPa as shown in Figure 3.3 (b), representing the expected lesion region. *In vivo* results for the parametric acoustic pressure amplitude cases 2.0 (G), 2.8 (H), and 4.0 MPa (D) are illustrated in Figure 3.6 using boxplots. Frequently, the axial dimension was limited by the thickness of the myocardium with the therapy beam penetrating the left ventricle entirely before the pressure amplitude fell below the threshold p_L. Likewise, the therapy beam pressure rose above p_L before entering the myocardium. Therefore an increase in pressure at the focus will only show limited increase in the axial lesion size. Radial macrolesion

expansion is hyperlinear and follows the prediction of the simulation shown as the plotted curve in Figure 3.6 (c). Simulations were done to compute the average radius of the acoustic beam above the hypothesized threshold p_L (2.0 MPa).

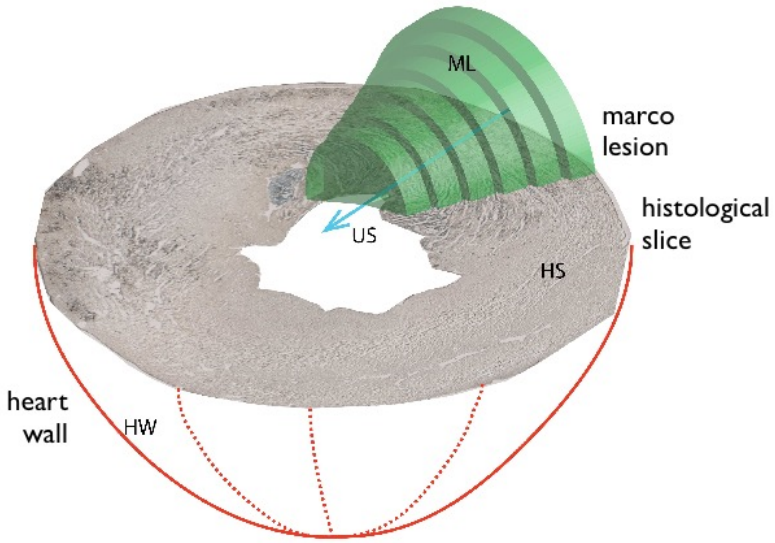

Figure 3.5: Diagram illustrating a macrolesion as characterized from a stack of histology slices. The heart wall (HW) is depicted in red lines. A cross-section of the heart is shown as a histological slice (HS), stained with Evans blue indicating cell necrosis, *i.e.* microlesions. The ultrasound beam is indicated as a blue line and arrow (US) and was derived from least square fitting of microlesions. Along the beam, the shown green cylindrical disks were characterized from cylindrical volume elements that contain 95% of the local microlesions. These coaxially stacked disks form a radially symmetric volume, called the macrolesion (ML), which is assumed to correlate with the *in situ* acoustic field.

3.3.2.2 Microlesion Characteristics

The spatial variation in lesion density was analyzed with respect to the therapeutic beam geometry. Specifically, lesion density was plotted as a function of local pressure amplitudes. Reslicing of the therapeutic beam volume was facilitated by placing axially oriented disks. Stacking them along the therapeutic beam as illustrated in Figure 3.5 in green, allowed for plotting of lesion density as a function of local in situ pressure amplitudes. Least square fitting shown as a blue line in Figure 3.7 (a) resulted

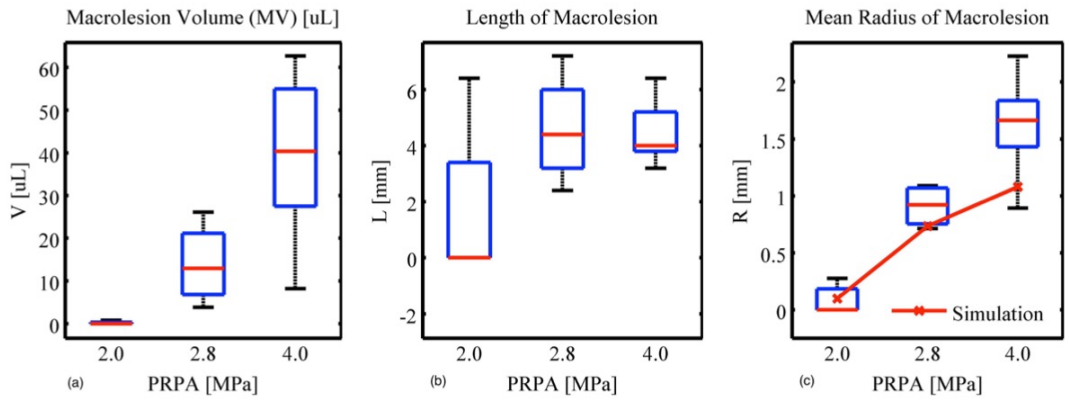

Figure 3.6: Treatment impact for different acoustic pressures. Here included: (a) macrolesion volume, (b) length of macrolesion and (c) radius of macrolesion for groups exposed under 2.0 MPa (G), 2.8 MPa (H) and 4.0 MPa (D). Simulations were done for a mean radius of acoustic field above the lesion formation pressure threshold of 2.0 MPa (PRPA). Macrolesion volumes appear positively related to acoustic pressure, where contributions come from the radial direction while the axial sizes are insignificantly different.

in $y = 4.52x - 4.07$, with 0% lesion density occurring at 0.9 MPa indicated by the red circle. The microlesion volumes for resliced disks versus different acoustic amplitudes are plotted in Figure 3.7 (b) with least square fitting resulting in $y = 57.2x - 130.0$ and zero microlesion volume occurring at 2.3 MPa indicated by the red circle.

3.3.3 Contrast Agent Availability Versus Macrolesion Characteristics

As alluded to in the previous section, macrolesion dimensions are dictated by several experimental conditions, including contrast agent availability. More available agent will likely generate more lesions. On the other hand, more contrast agent per unit time may lead to agent induced acoustic shadowing and a diminished in situ pressure wave amplitude. Results for changes in contrast agent availability are shown next.

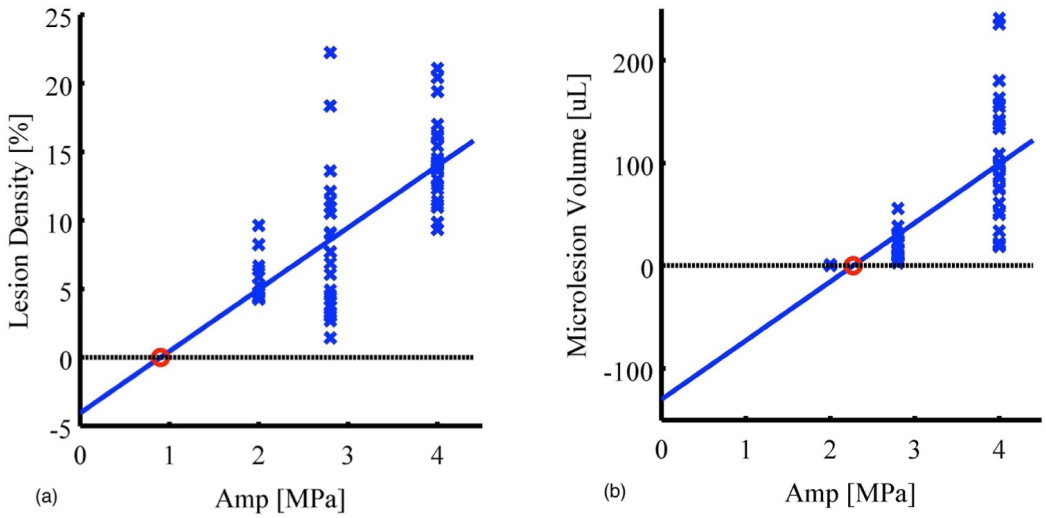

Figure 3.7: Treatment impact characterized for re-sliced volume along therapeutic beam. Results for exposures of 2.0, 2.8 and 4.0 MPa PRPA are shown for: (a) scatter plot of lesion density with least square fitting and zero crossing 0.9 MPa PRPA; (b) scatter plot of microlesion volume with least square fitting and zero crossing 2.3 MPa PRPA.

3.3.3.1 Infusion duration

At first a constant infusion rate of 5 $\mu L/kg/min$ was tested for three infusion durations, namely 30, 100 and 300 seconds, for groups J, I and D, respectively. Under ultrasound exposure, increase in contrast infusion time allows for higher deposition of total number of microbubbles. Figure 3.8 shows a positively correlated number of generated lesions for the respective total infusion duration. Differences in visual score and microlesion volume for durations of 30 and 100 s are not statistically different. However, a 300 s infusion duration shows a significant increase relative to the former two conditions with respect to the characterized microlesion volume. Specifically, the microlesion volume increases from 10, to 30, to 300 s is not linear and will be addressed in the Discussion section.

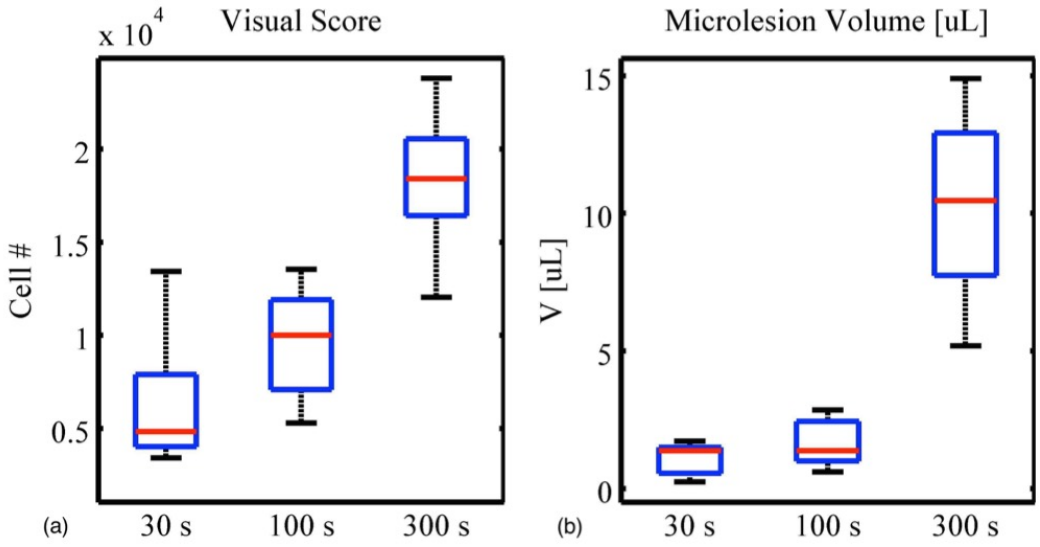

Figure 3.8: Treatment impact for different contrast agent infusion duration. Results for (a) visual score and (b) microlesion volume for groups infused with contrast agents for 30 s, 100 s, and 300 s, at a rate of 5 μL/kg/min, for groups J, I, and D, respectively. A positively correlated number of generated lesions is seen for the respective total infusion duration. Differences in visual score and microlesion volume for durations of 30 and 100 s are not statistically different. However, an infusion duration of 300 s significantly differs from the former two conditions.

3.3.3.2 Infusion rate

Here a constant total dose of contrast agent (25 $\mu L/kg$) was tested for two infusion rates, namely 5 $\mu L/kg/min$ for 5 mins and 12.5 L/kg/min for 2 mins, for groups D and E respectively. A higher infusion rate, *i.e.* more agent per unit time, may lead to agent-induced acoustic shadowing and a diminished *in situ* wave pressure amplitude. Figure 3.9 shows no significantly different number of generated lesions for the respective infusion rates. Note that microlesion volume here refers to the total volume of all induced microlesions over the entire myocardium, which is not identical to the shown microlesion volume within the characterized macrolesion (macrolesion volume times lesion density).

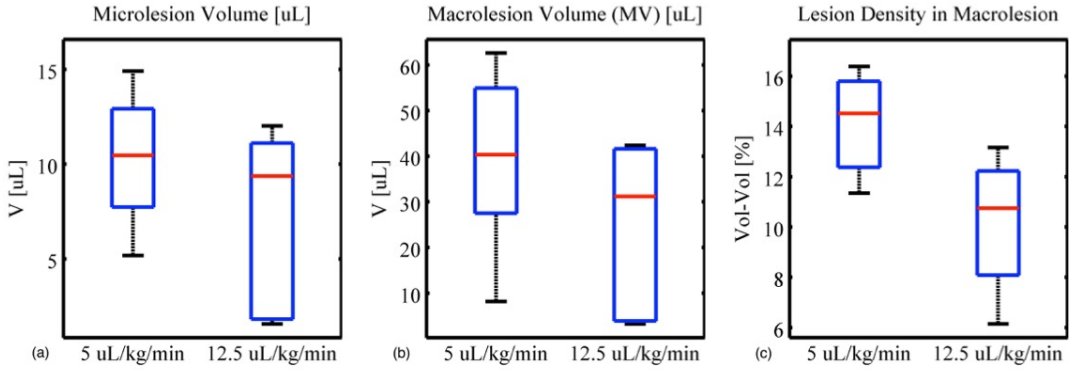

Figure 3.9: Treatment impact for different contrast agent infusion rates. Results are shown for (a) microlesion volume, (b) macrolesion volume and (c) lesion density for groups infused with contrast agents for 5 min at a rate of 5 μL/kg/min (D) and 2 min at 12.5 μL/kg/min (E), *i.e.* yielding the same total dose. They are not significantly different, showing that the impact is dominated by the cumulative dose.

3.3.4 Therapy Beam Sweeping

In this experiment, Gaussian modulation was employed to mimic therapy beam sweeping. It was observed as shown in Figure 3.10 that both the resulting macrolesion volume as well as the microlesion density inside the created macrolesion are reduced in comparison to the static beam, but not significantly different. The median macrole-

sion volumes resulting from square and Gaussian modulations are 65.6 μL and 40.3 μL respectively, and the median lesion densities are 16.8% and 14.4%.

The pulse modulation groups corresponding to square and Gaussian profile are shown in Figure 3.2. In the simulation modeling, the volume exposed by negative pressures greater than 2 MPa, and marked by circles, were integrated across space and time yielding 4.5 and 2.7 $\mu L \cdot s$ for square and Gaussian modulation, respectively.

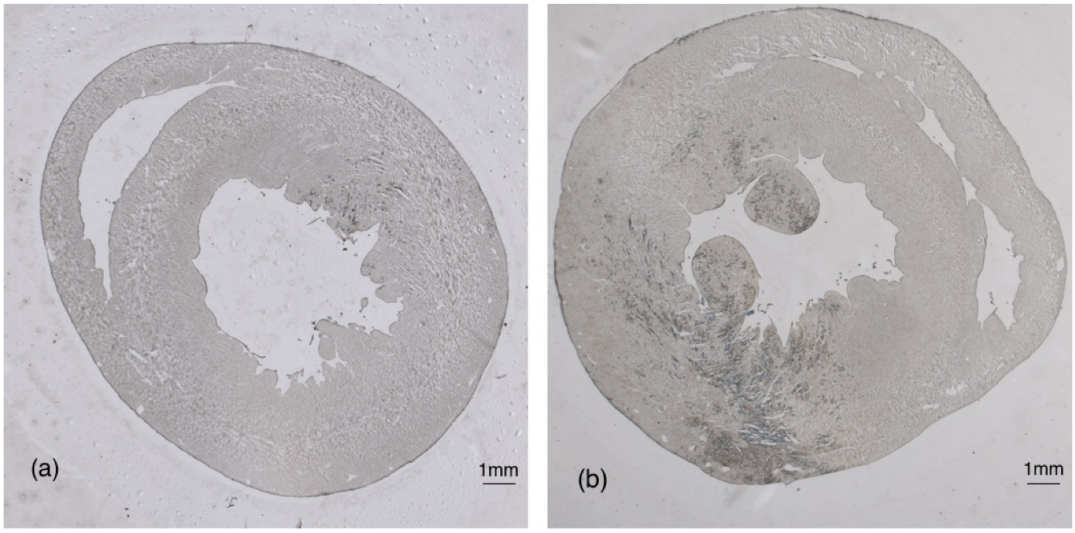

Figure 3.10: Example microscopic brightfield images of treated heart slices. The histology slice (a) contains sparse microlesions. Note that microlesions appear with a light blue stained by Evans blue. The shown histology violates the standard heart model shown in (b). Distributed myocytes are lying in different tissue layers and with varying orientations.

3.4 Discussion

The quantitative results generated by the previously developed and here tested computer-aided scheme provide possibilities for numeric and quantitative 3D lesion analysis and their dependence on experimental parameters that were investigated for their relevance for developing and improving MCET.

3.4.1 Cardiomyocyte Scoring

Visual lesion counting, as a traditional evaluation method, is appropriate for low lesion count cases as discussed for Figure 3.4. However, for therapeutic applications, a large number of lesions require tedious counting. The computer-aided scheme (*Zhu et al.*, 2015a) provides for an objective and quantitative lesion analysis. As shown in Figure 3.4, a dramatic change in visual score versus auto score for high-count cases opposed to low-count cases reveals the limitation of visual scoring, when counting large numbers of lesions. Machine operated and tested algorithms prevail. Note that even at low counts, auto score has a positively correlated relationship to visual score but does not have a one-to-one correspondence. Variance arises from manual bias differentiating individual cells from a clustered cell pool. On the other side as for auto scoring, imperfection exists when a constant conversion factor is employed for converting microlesion area, *i.e.* image pixels, on a given histology slide to a fixed number of cells, eq. 1. An additional limitation is the assumption that cells possessing the same dimensions for each heart layer but different orientations for three layers (*Zhu et al.*, 2015a). Our model uses a statistical average based on a standard heart. This might lead to partial violations when the actual geometry (Figure 3.11 (a)) differs from the standard heart (Figure 3.11 (b)).

3.4.2 Experimental Perturbations Exclusions

Initially, the choice of injections sites, *i.e.* the jugular vein versus the tail vein, were thought to possibly influence the number of systemically circulating microbubbles. Comparing the two cohorts, however, showed that the two microbubble administration routes were equivalent. As shown in Figure 3.12, tail vein (A) versus jugular vein (B) injection did not lead to significant differences in the subsequent lesion formation in either lesion density or in macrolesion volume. Additionally, variations of transducer aiming were tested. Intentionally aiming ultrasound at ribs (Group C)

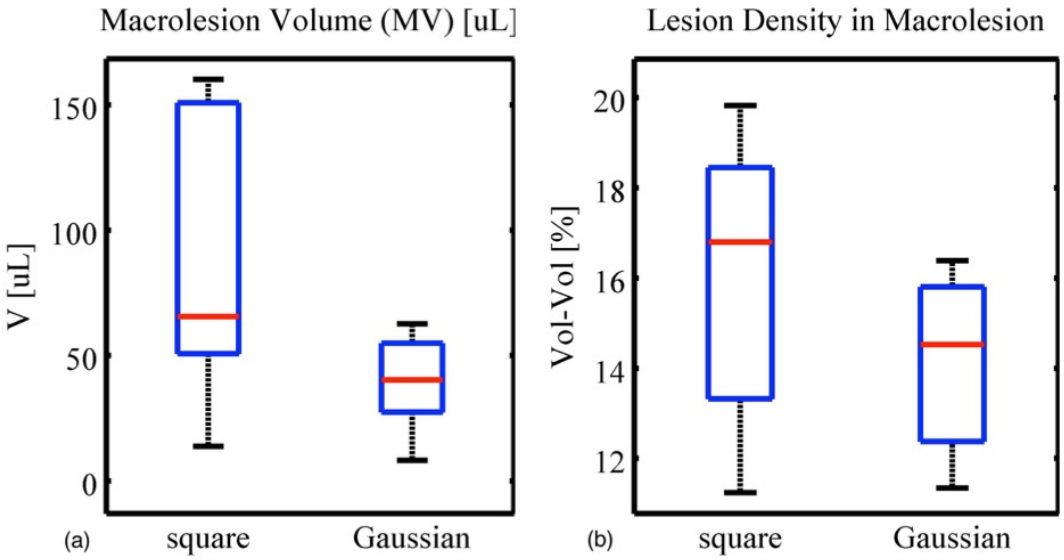

Figure 3.11: Treatment impact for square and Gaussian pulse modulation schemes. Results for the impact of individual focal treatment (group B) versus a swept beam (group D) are shown for (a) the corresponding macrolesion volume and (b) the observed lesion density. Similar impact is seen between Gaussian modulation and square modulation, which validates that a swept beam scheme might be a viable method to shorten treatment duration.

does not impact the therapeutic result. *In vivo* variations can be significant (see error bars in Figure 3.12); however, there is significant overlap between the tested routes for injection and between various aiming paths.

3.4.3 Acoustic Field Modeling

3.4.3.1 Acoustic Amplitude

Acoustic modeling provides a way to approximate lesion formation. In the therapy, impact analysis bioeffects of various acoustic exposures were investigated. The associated field simulation underestimates the mean radius of the macrolesion at 4 MPa as shown in Figure 3.6 (c). This is because *in vivo* some of the beam penetrates the left ventricle. This part of the beam was not excluded in the simulation, thus the simulation resulted in averaging out the affected macrolesion radius. Another factor contributing to the greater treatment effect seen *in vivo* than the simulation comes from deformation of hearts after being harvested. Rats were treated at the ends of systole but hearts were relaxed after being sacrificed. Thus the acoustic pattern may be distorted to some extent.

3.4.3.2 Swept Beam

Treatment in humans will require focusing of the therapeutic beam at a larger area than currently done in rodents (rats). Such will either lead to the need of a modified, *i.e.* larger, point spread function or more likely numerous repetitions of individual exposures. The latter can be realized by either individual focal treatments or by employing a swept beam. The former will require a longer time for treatment of an equivalent total count of focal spots since the beam will be stepped from treatment location n to n+1., therefore a swept beam was investigated. Illustrated by O plot marks in Figure 3.2, are the individual tone bursts that exceed the lesion formation pressure threshold. With that and the previously mentioned axisymmetric rotational

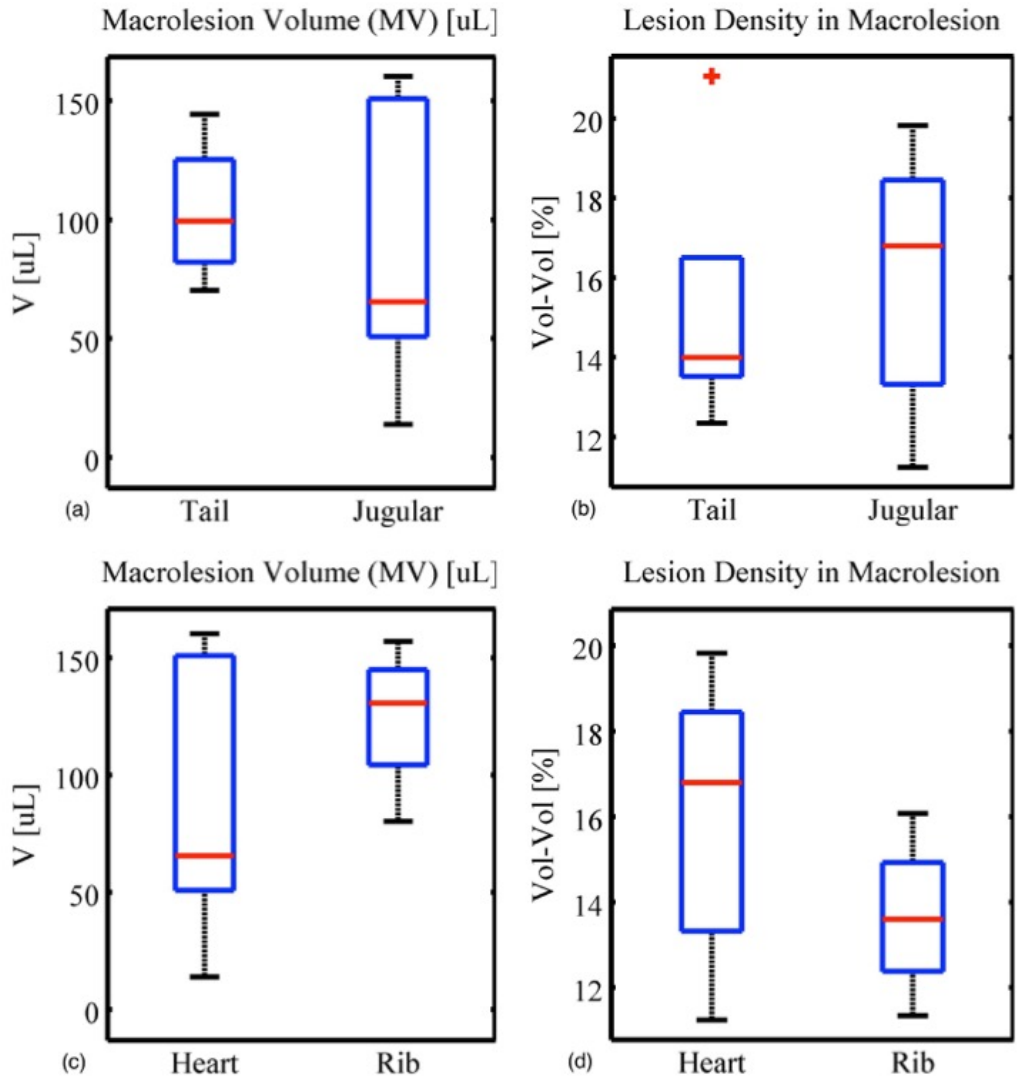

Figure 3.12: Comparison of treatment impact for different injections sites and ultrasound aiming strategies. Results show (a) macrolesion volume (b) and lesion density for two microbubble administration routes, *i.e.* tail vein (A) versus jugular vein (B) injection; additionally shown are (c) macrolesion volume and (d) lesion density for regular aiming (B) and intentionally aiming at ribs (C). Injection and aiming variations do not significantly differ among the tested groups.

model (point spread function), an effective treatment volume was simulated. Integration across space and time, yielded 4.5 and 2.7 $\mu L \cdot s$ for square and Gaussian modulation, respectively. Therefore the swept beam simulation predicts an effective volume of 59.8% of that of an individual focal treatment. The experimental macrolesion volume shown in Figure 3.10 (a) yields an effective median volume fraction of 61.5%, supporting the axisymmetric rotational volumetric model.

3.4.4 Thresholded Induced and Statistically Accumulated Lesion

3.4.4.1 Lesion Formation as Accumulated Statistical Events

In the experiment of increasing infusion, the slightly decreasing trend of lesion density shown in Figure 3.6 may indicate some shadowing effect caused by a large population of instantaneous microbubbles placed along the beam path, acting as scatterers. However, the shadowing factor will need to be verified for the cases of a longer path, such as in a larger animal model.

The experiment of various infusion durations of contrast agents is potentially equivalent with longer duration exposure. As shown in Figure 3.13, visual score, microlesion volume, macrolesion volume and mean radius of macrolesion showing positive correlation revealing the fact that the probability to create lesion is accumulated over time. Growth of the macrolesion radius indicates that the edge of the macrolesion is contributing to the lesion formation over time. Lesion density increases for longer infusion times. Short term and intermediate do not significantly differ. This could be due to the lack of statistical power or too short of a duration to allow for fully developed statistical analysis. The macrolesion lengths are not showing any strong correlation with the infusion interval, as they are likely limited by the distal ventricle and possibly due to tissue attenuation.

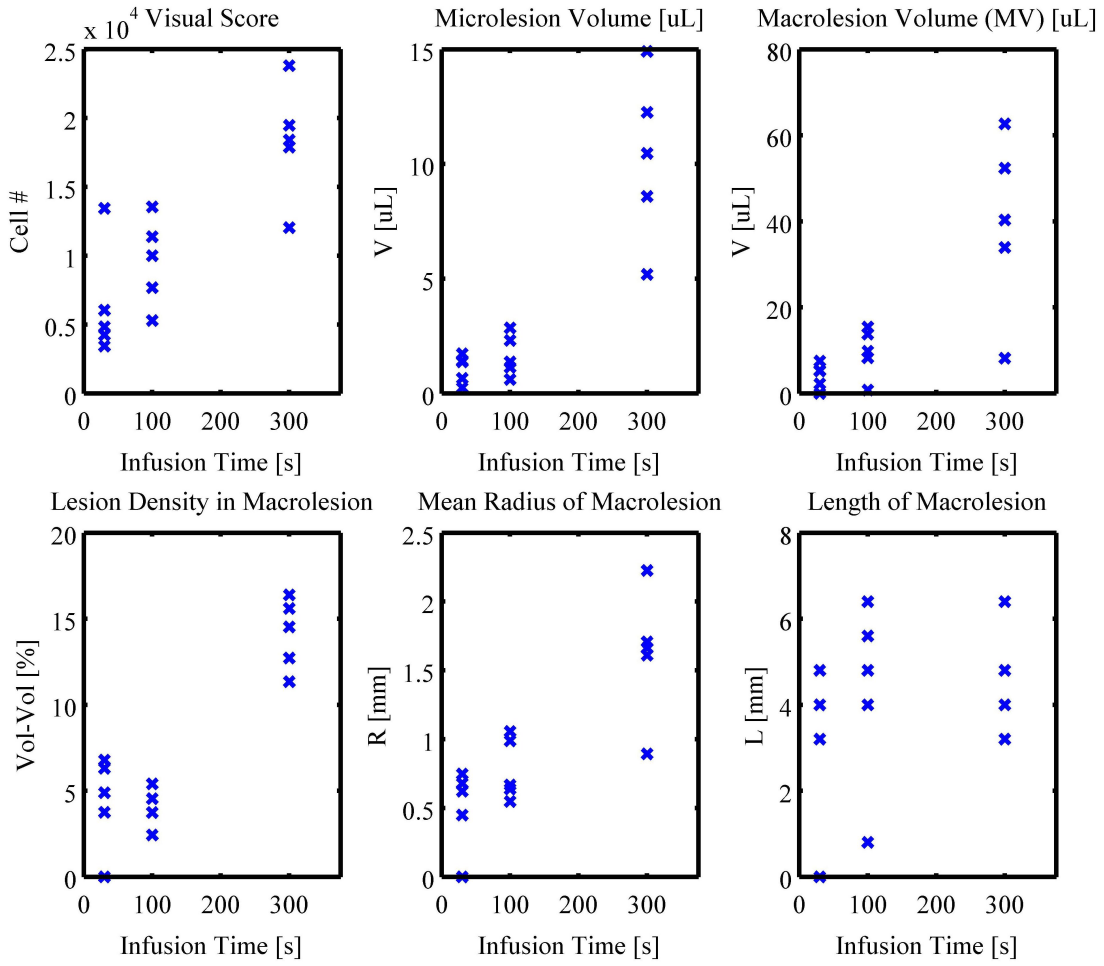

Figure 3.13: Scatter plot of characterized parameters versus infusion durations. Results for (a) visual score, (b) microlesion volume, (c) macrolesion volume and (d) macrolesion mean radius show some linear dependence with respect to infusion duration, revealing the fact that the probability to create lesion is accumulative over time. Growth of the macrolesion radius indicates that the macrolesion edges contribute to the lesion formation as well.

3.4.4.2 Microlesion Density versus Ultrasound Amplitude

Least square fitting in Figure 3.7 (a) implies that an increasing acoustic pressure has a positive effect on microlesion formation up to 4 MPa, *i.e.* higher acoustic pressure or exposure possesses the higher potential to induce bioeffects. A similar positive correlation of acoustic amplitude on cavitation-induced bioeffects was also presented by Samuel et al. (*Samuel et al.*, 2009). One possible reason is that larger pressure will result in a larger active microbubble population. Therefore a larger density of microlesion will be induced by the then more frequent microbubble cavitation events. For a constant pressure amplitude, macrolesions also grow radially over time. This is because of the probabilistic accumulation of microlesions on the penumbra of the current macrolesion. There the probability for microlesion generation is larger than zero percent and smaller than one hundred percent, *i.e.* the sound pressure amplitude is close to the threshold p_L discussed above. If is 20%, then a 5-times longer exposure will statistically result in additional lesion formation.

3.4.4.3 Acoustic Pressure Threshold

The zero microlesion volume shown in the line fit in Figure 3.7 (b) might overestimate the acoustic pressure threshold for lesion induction. This is because microlesion volumes were characterized in a way that could bias towards beam regions with lower acoustic pressure and hence lower partial microlesion volume.

Additionally, the acoustic pressure threshold for microlesion induction by either lesion densities or microlesion volumes, is a rough estimation and may be inaccurate due to biological variations, with R^2 being 0.48 and 0.56.

3.4.5 Application in Human

Ideally, the wanted axial length of the transducers point spread function matches the myocardial thickness. Here in the presented small animal model, a shorter depth

of field would have been desirable, though no side effects for here 1 day acute studies, except for some pulmonary hemorrhaging, presented in the study. The characterized macrolesions for all rats showed similar lengths, which in most cases here is due to the acoustic path restrained by the limited thickness of the left vertical wall. However, when the study moves to a larger animal model (such as swine) rather than the currently employed rodents (rats), the effect of therapeutic pressure on the macrolesion length will manifest itself and be vital for lesion formation and accretion.

The shown results serve as a preliminary test of MCET for application in humans. The main benefit from this therapy method is the minimal invasiveness and the hypothesis that cavitation-induced, sparsely distributed microlesions dont lead to major infarct-like scars, which can disrupt conduction pathways and lead to heart block, such as for alcohol ablation treatment (*Folkert et al.*, 2010). The relationship between lesion characteristics from the small animal model, such as lesion dimension and density, and *in situ* ultrasound field, is assumed to be analogous to that of a large animal model. Both models follow the same rationale of lesion formation. In the larger model, especially in humans it is anticipated that we will have to create composite lesions, *i.e.* lesions created by electronically and/or mechanically sweeping the beam. For therapy of large volumes, the therapy beam will likely be scanned through the desired volume (simulated here by the Gaussian modulation) to accomplish the treatment in less time than is needed to treat point by point (as in high intensity focused ultrasound (HIFU)). Suppose a human subject needs MCET treatment at a myocardial region of 4 cm diameter (*Maron*, 2005). Assuming that the left ventricular wall of the hypertrophic heart has a 21 mm thickness (*Maron et al.*, 2003b), a macrolesion, approximated as a cylinder, with volume $pi \times (4cm/2)^2 \times 21mm = 28.4mL$, would be needed. Assuming the therapy employs the recommended dose of Definity® for diagnostic exams, *i.e.* $5\mu L/kg/min$, a five-minute treatment of a single focal spot will yield a 50 μL macrolesion with 20% microlesion density. To create the aforemen-

tioned macrolesion, a total duration of approximately 2,640 minutes will be needed to achieve the desired lesion volume. Recruitment of a swept beam to foster the lateral lesion formation at 56 fps, as discussed above, will reduce the total duration to 47 minutes. Stacking multiple axial focal zones will enlarge axial lesion size and further accelerate the therapy. The above calculations are under the assumption that the *in vivo* microbubble distribution in the myocardium is similar in human and the chosen rat model. A large animal model for human cardiophysiology, such as swine, will be needed for investigating the clinical transition for MCET.

3.5 Conclusion

The quantitative scoring scheme overcomes the limitation of traditional visual scoring and works for histological cases with a large lesion count, *i.e.* has an appropriate dynamic range for evaluating therapeutic applications. The presented results have shown that MCET-induced macrolesions grow radially as the acoustic pressure amplitude increases. A swept beam as a new method to shorten treatment time seems promising but requires additional verification to ensure efficacy. These characterizations and validations may assist future MCET treatment planning.

CHAPTER IV

Chronic Effect Evaluation of MCET

4.1 Introduction

Currently available clinical methods for myocardial reduction in treating Hypertrophic Cardiomyopathy (HCM) are debulking of the myocardium. The primary method for reduction of asymmetric septal hypertrophy with perturbation of the mitral valve leaflets, surgical septal myectomy, is largely invasive(*Maron et al.*, 2003a; *Gersh et al.*, 2011). Alternatives to surgery have been sought using various technologies, such as thermal ablation using ultrasound (*Otsuka et al.*, 2007) or radiofrequency ablation (*Lawrenz et al.*, 2011), alcohol septal ablation (*Gersh et al.*, 2011; *Leonardi et al.*, 2010) and so on. To date, these techniques are not widely used due to their limitations and potential adverse consequences, *e.g.* a need for pacemaker implantation in 21% of patients (*Lawrenz et al.*, 2011).

We have developed a novel ultrasonic technique called Myocardial Cavitation-Enabled Therapy (MCET), which aims to shrink the targeted myocardium over time after noninvasive treatment. The treatment involves intermittent pulsed ultrasound (higher than normal diagnostic pressures, (*Miller et al.*, 2015)) together with ultrasound contrast-agent microbubbles to generate cavitation and tissue injury in the myocardium. This treatment produces scattered sites of ultrasound-induced injury, so called microlesions, only in the volume of interest. The target volume can be

manipulated by focusing ultrasound and is defined as a macrolesion. In previous acute animal studies, characterized MCET lesion creation (*Zhu et al.*, 2015a) was dose-dependent, adjustable by manipulation of the ultrasound focus, optimized at the end of systole, could be monitored by premature ventricular complex frequency, and the degree of injury correlated with troponin levels (*Miller et al.*, 2014a,b, 2015; *Zhu et al.*, 2015b). However, the extent of tissue shrinkage as the final goal remains to be addressed.

This chapter focuses on the long-term effect evaluation of the myocardium after MCET to verify the central hypothesis, i.e. myocardial reduction. With the computer-aided histological scheme, the fraction of myocardial tissue destroyed and the resulting scar formation, along with the extent of tissue shrinkage were evaluated.

4.2 Methods and Materials

4.2.1 Animal and Tissue Preparation

Tissue samples were collected and prepared for histological evaluation 6 weeks after treatment. Briefly, *in vivo* acute operations were conducted under ketamin/zylazine IP anesthesia on Dahl SS rats (Charles River, Wilmington, MA, USA) and SS-16^{BN} rats (Medical College of Wisconsin, Milwaukee WI) under the approval and guidance of the Institutional Animal Care and Use Committee. All rats in the treated group were infused with an in-house developed closely duplicate of the ultrasound contrast agent Definity® (Lantheus Medical Imaging, Inc., N. Billerica, MA), as described previously (*Lu et al.*, 2016; *Miller et al.*, 2016), at a rate of 5 μL/kg/min (tail vein catheter). MCET was acoustically facilitated with a 1.9 cm diameter and 3.8 cm focus single element transducer transducer, aimed i*n vivo* using a co-aligned cardiac phased array (10S, Vivid 7, GE Healthcare) to focus approximately 0.5 cm into the myocardium as illustrated in Figure 4.1 (*Miller et al.*, 2014a). For therapy,

5 or 10-cycle tone bursts at 1.5 MHz, 16 repetitions of peak rarefactional pressure amplitude (PRPA) above 4 MPa at a 0.25 ms pulse interval, *i.e.* 4.0 kHz pulse repetition frequency (PRF), were sent. Ultrasound exposures, modulated by a square or Gaussian function (*Lu et al.*, 2016), were triggered every 4 or 8 heartbeats, at end-systole (RR/3, using ECG gating), and lasted for 5 or 10 minutes. The rat sham group was exposed using either set of parameters for 5 or 10 min without infusion of contrast agent, followed by 5 or 10 min infusion of contrast agent with no ultrasound exposure. Long-term follow-up was undertaken to assess treatment outcomes with no adjuvant, losartan or methylprednisolone (MP). The use of methylprednisolone and losartan as adjuvants intended to reduce the acute inflammatory response (*Roberts et al.*, 1985) and subsequent scar formation (*Frimm et al.*, 1997). A high dose of 30 mg/kg MP or low dose of 1 mg/kg given at therapy and at 3, 6 and 24 hr post therapy were utilized. Losartan was dosed at 10 mg/kg/day by gavage starting one day after ultrasound treatment and continuing for 4 wks.

At the end of wk 6, the hearts were removed. After cannulation of the aortas, the hearts were immersed in formalin after being connected to a column of neutral buffered formalin set to a height equivalent to a pressure of 15 mm Hg (20 cm H_2O). In this way, the hearts were fixed approximately in an end-diastolic configuration (Whittaker and Patterson, 2000). Each heart was cut parallel to the atrioventricular groove into four or five slices. For each rat, one slice that included the most treatment area was processed at the Histology Core of the University of Michigan Dental School with Massons trichrome staining to show fibrosis.

4.2.2 Microscope Image Acquisition

Brightfield microscopic images were obtained for each tissue-section through a microscope camera system (SPOT Flex, Diagnostic Instruments, Inc., Sterling Heights, MI, USA) with a high resolution and large field of view objective (Leica Plan APO

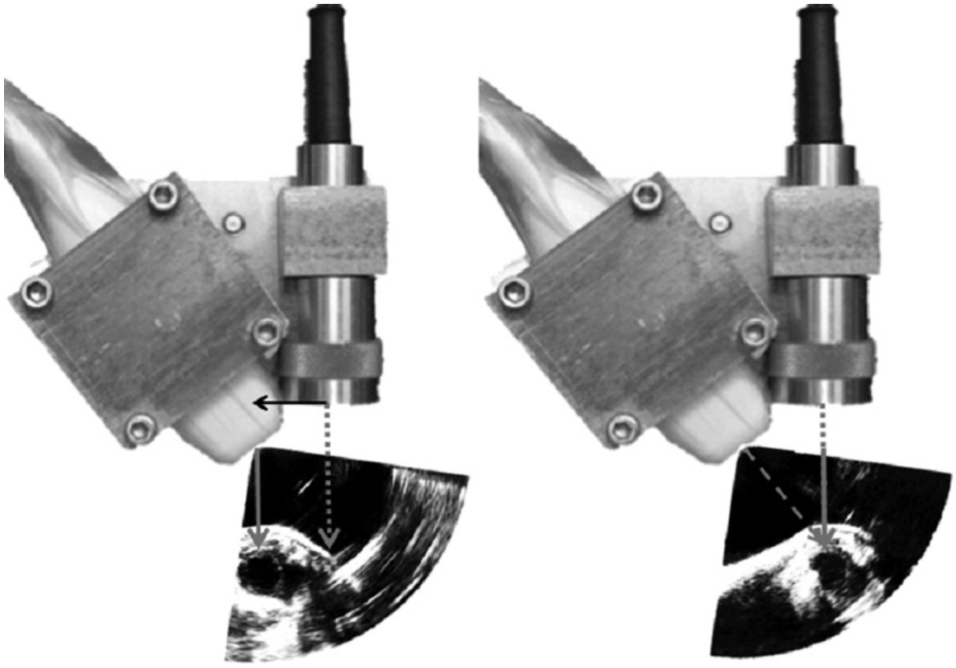

Figure 4.1: Schematic of the positioning setup of the imaging probe and the therapeutic transducer. For targeting, the rat heart was located at 2.25-cm depth at the edge of the sector, as illustrated on the left. Subsequently, the therapeutic transducer was moved in so that the beam followed the same path (dotted gray line) as the previously identified image line (solid gray line), as illustrated on the right. The heart was right in the focal zone of the therapeutic transducer (3.8-cm focal length), as illustrated at the center of the image sector at 2.75-cm depth (dashed gray line). The solid black arrow line on the left side indicates the movement of the therapeutic transducer (1.9 cm). (*Lu et al.*, 2016)

Table 4.1: Table of experimental conditions used. (Note: * indicates sham treatment of rats exposed to ultrasound for 10 min followed by microbubble infusion for 10 min without ultrasound.)

Group ID	n	Rat model	Pulse cyc no.	Pulse Modulation	Treatment Duration (min)	Adjuvant	Fibrosis fraction %	Histo wall (mm)
A	6	Dahl SS	5	15 ms Gaussian	5	none	9±6	N/A
B	6	Dahl SS	10	4 ms square	10	none	34±11	N/A
C	4	Dahl SS	10	4 ms square	10	none	35±7	N/A
D	3	Dahl SS	10	4 ms square	10	Losartan	35±2	N/A
E	3	Dahl SS	10	4 ms square	10	MP	35±4	N/A
F	4	SS-16^{BN}	10	4 ms square	10	MP, Losartan	33±5	3.08±0.28
G	7	SS-16^{BN}	10	4 ms square	10	MP, Losartan	42±10	2.29±0.33
H*	8	SS-16^{BN}	10	4 ms square	10	MP, Losartan	49±4	2.74±0.32

1.6x, Leica Microsystems, Ltd., Heerbrugg, Switzerland). The images were acquired as 16 bit 4,096 by 4,096 pixel, RGB, covering the entire tissue sections. Three image sets of sham, moderately treated and severely treated, respectively, are shown as an example in Figure 4.2. The upper row are photographs of the harvested hearts, the middle row are corresponding microscopic Massons-stained images used in image processing for analysis with the third row being zoomed in for the fibrous region for better illustration. The tissue fibrosis was evident in Massons trichrome-stained slides. Blue-stained areas (collagen) were indicative of fibrosis formation in the lesion areas relative to the red background tissue.

4.2.3 Image Processing for Quantitative Analysis

As illustrated in Figure 4.3, tissue detection was done first to set boundaries for fibrosis analysis and form the base for myocardium wall thickness measurement. After fibrosis detection, the region affected by the therapeutic beam was estimated. Fibrosis density was measured within the region, which also served as an objective segment of the heart wall for thickness measurements. Radially measured heart wall thickness measurements were enabled by the morphologic information of the heart from the tissue mask.

Tissue detection: The main objective in this step is to segment the tissue portion based on morphologic information from brightfield images to constrain the subsequent characterization. This is similar to the tissue detection technique involved in (*Zhu et al.*, 2015a), except that RGB images were transformed to gray scale, which is less computationally expensive without sacrificing spatial information. Gray scale images were downsampled first to be segmented and then upsampled back after segmentation to decrease computational load. A threshold mask and an edge-detected mask were obtained simultaneously from a normalized brightfield image, which was then fused together yielding the tissue mask.

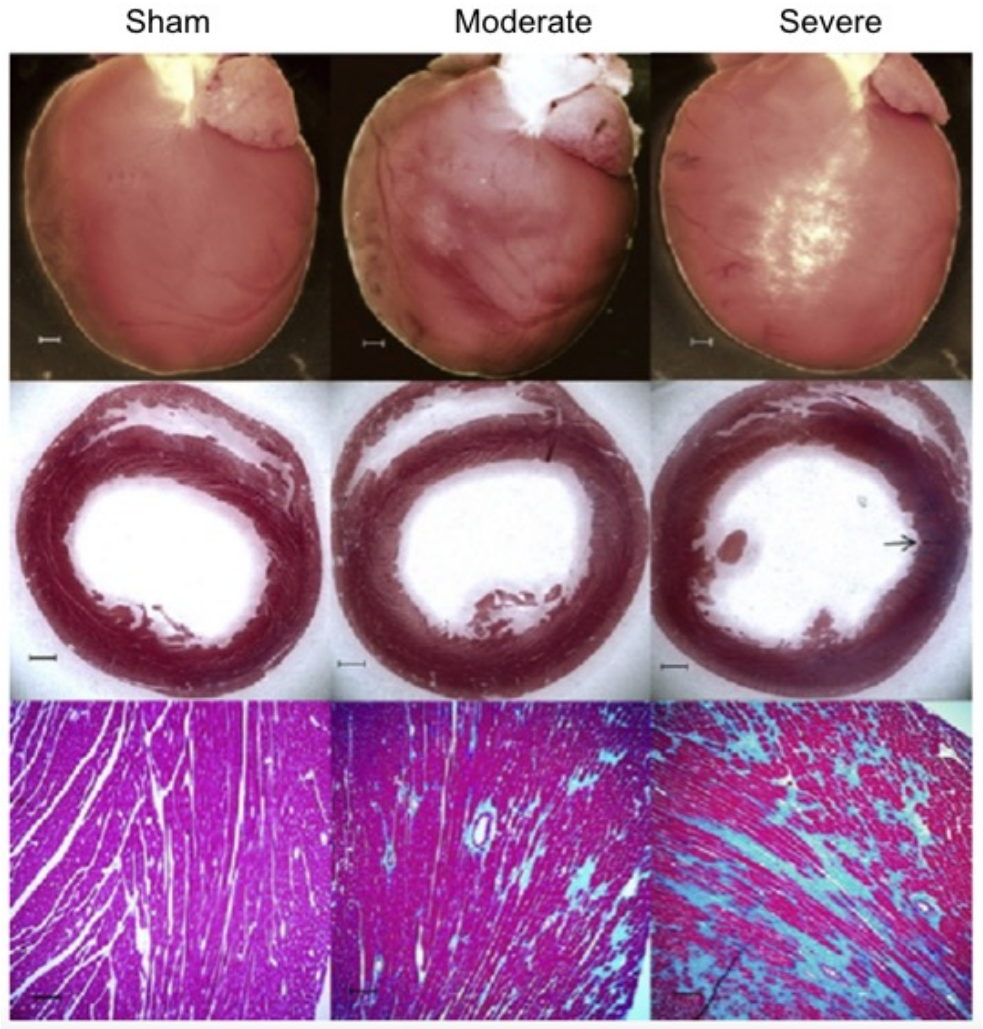

Figure 4.2: Example photographs and microscopic images for Massons trichrome-stained hislotogical slices, from left to right columns for groups sham, A and B, and top to bottom for heart photograph, microscopic image being processed and zoomed sections revealing Massons trichrome-stained cells respectively. Upper row: 1x magnification photographs taken 6 wk after exposure. Bar = 1 mm. Middle row: 1x magnification brightfield images of Massons-stained slices, used in image processing for analysis; arrow points to possible tissue shrinkage within damaged area. Bar = 1 mm. Lower row: 10^3 magnification brightfield images of Massons-stained slides. Bar =100 μm. (*Lu et al.*, 2016)

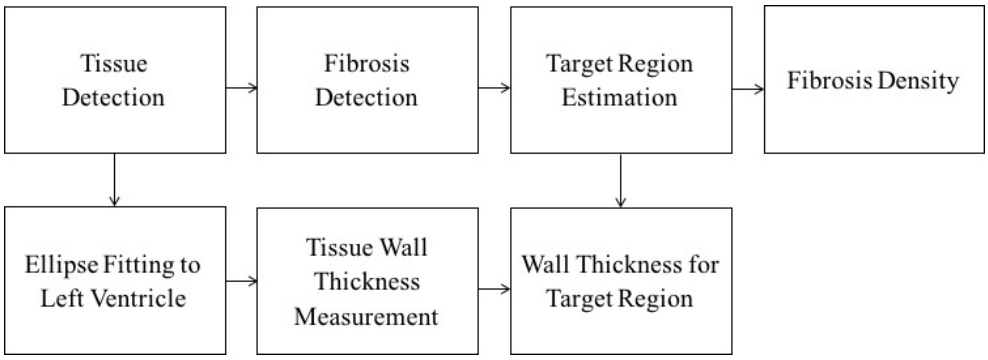

Figure 4.3: Flow chart of image processing for measurements. Tissue detection was done first to set boundaries for fibrosis analysis and form the base for myocardium wall thickness measurement. After fibrosis detection, the region affected by the therapeutic beam was estimated. Fibrosis density was measured within the region, which also served as an objective segment of the heart wall for thickness measurements. Radially measured heart wall thickness measurements were enabled by the morphologic information of the heart from the tissue mask.

Fibrosis detection: The original images of RGB color space were converted to Lab color space (*Hunter*, 1958, 1948). The Lab color space discribes mathematically all perceivable colors in the three dimensions with L for lightness and a and b for the color-opponents, green-red and blue-yellow. Since the lightness of the images are not interesting for tissue characterization, this dimension was eliminated. Only pixels within heart region were fed into the fibrosis detection. Pixel values in the two dimensions 'ab', were clustered by the k-means algorithm into 2 groups indicating fibrosis (blue) and normal tissue (red) based on Euclidean distance. K-means clustering, partitions observations, here observations as color vectors of the two dimensions 'ab', into k (here is the 2 color groups of fibrosis and normal tissue) clusters in which each observation belongs to the cluster with the nearest mean, serving as a prototype of the cluster. After k-means clustering iterated 3 times, to avoid local minima, the fibrosis mask was formed. An example is shown in Figure 4.5. The treatment target region was estimated from the centroid of the populated fibrosis with a 3 mm window as shown in Figure 4.4, which was estimated from acute lesion characterization (*Zhu et al.*, 2015a). Fibrosis fraction was then obtained by measuring the fraction of

fibrotic tissue in this treated region.

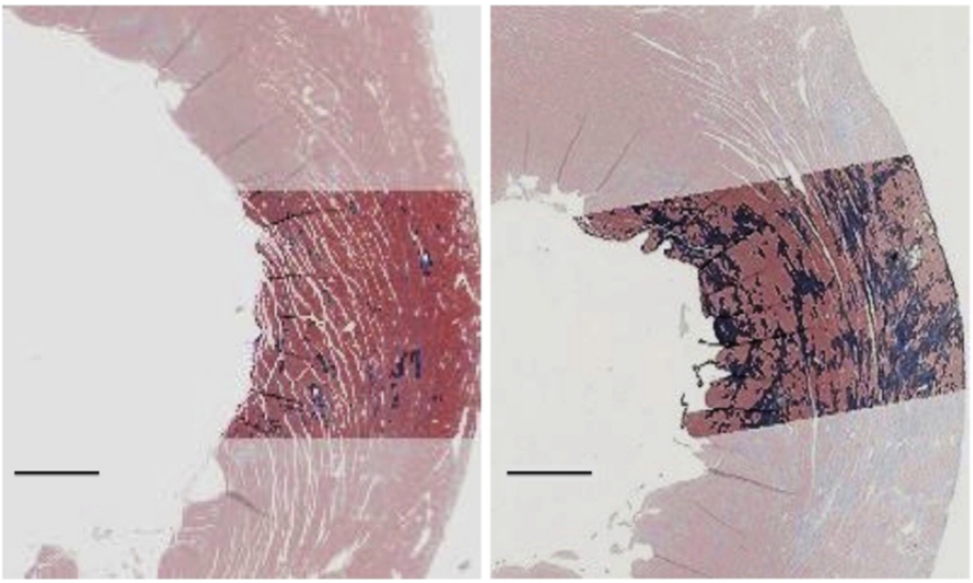

Figure 4.4: Quantification of the fibrotic tissue fraction within the treatment volume in Massons-stained slides. Transparent regions are the most dense lesion cloud ventricular wall regions where densities were calculated. Those regions are constrained by a 3 mm wide window. Left: group A, right: group B. Bar = 1 mm. (*Lu et al.*, 2016)

Heart wall thickness measurement: Based on the tissue mask, the heart wall thickness was measured radially from the left ventricular centroid. The thickness was defined by the distance from the left ventricular wall boundary to the other tissue being either the outer heart boundary or the septal wall boundary, whichever is closer, as indicated as line segments in the top left Figure 4.6. Quite often, sections were cut slightly oblique cut, resulting in an elliptical shape, for which the wall thickness was increased at the major axis ends of the ellipse. Therefore, an ellipse was fitted to the left ventricle. The measurements were corrected by normalizing the thickness measurements to the minor axis thickness as shown in bottom Figure 4.6. Finally the wall thickness evaluated for the treated region defined from fibrosis detection could be objectively quantified.

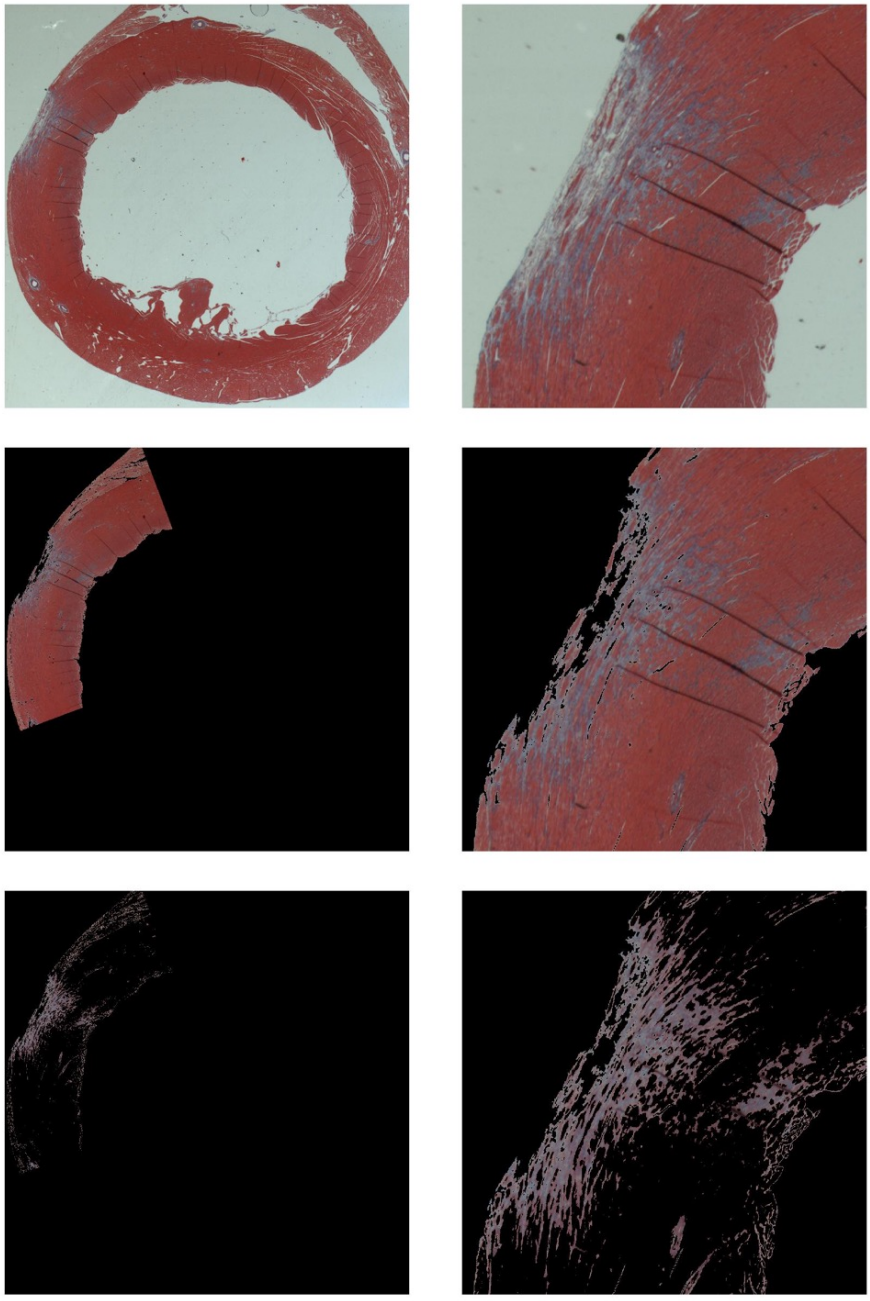

Figure 4.5: Example images illustrating fibrosis detection, from left to right columns for original and zoomed in images, and top to bottom for heart photograph, 1x magnification brightfield images of Massons-stained slices, tissue segment fed into k-means clustering and detected fibrosis, respectively.

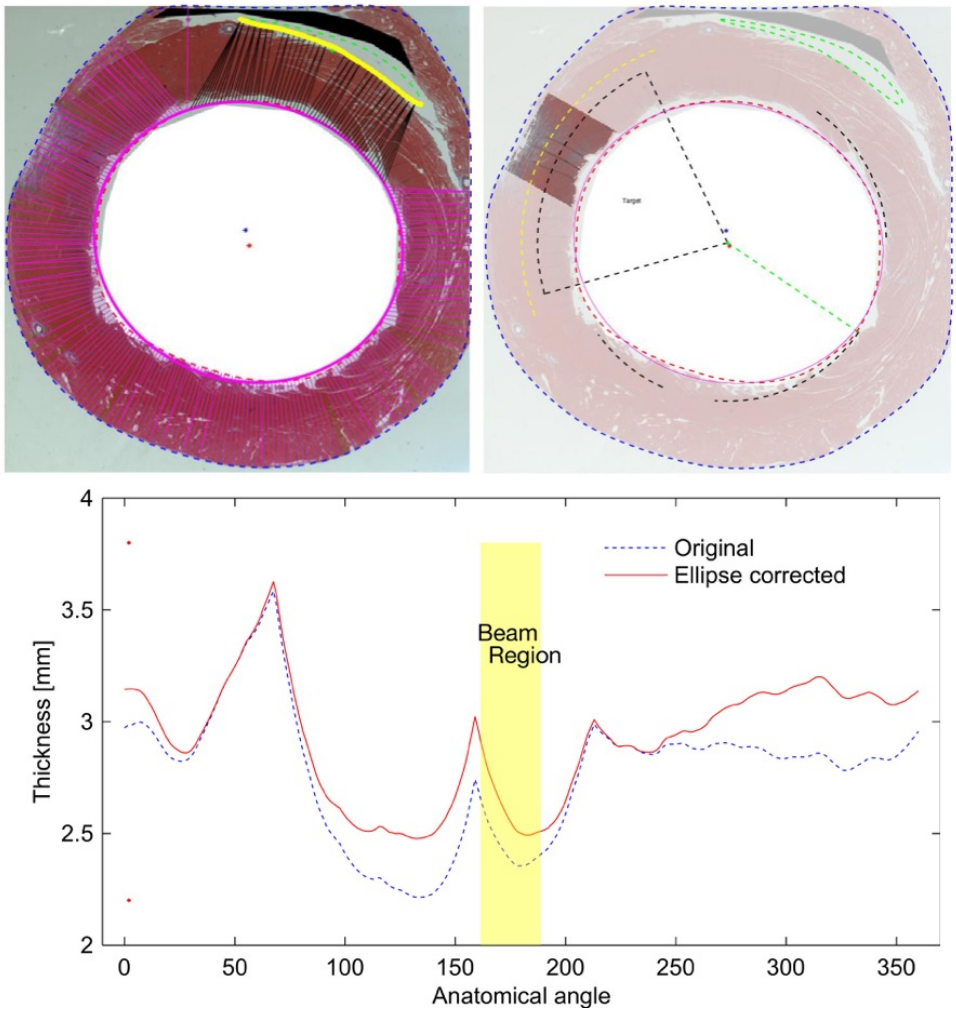

Figure 4.6: Example images illustrating the process of heart wall thickness measurement. Top left: the thickness was defined by distance from left ventricular wall boundary to another tissue boundary, being either the outer heart boundary or the septal wall boundary, whichever is closer, as indicated as line segments. Top right: the wall thickness was evaluated for the treated region defined from fibrosis detection. Bottom: wall thickness was measured radially from the center of the left ventricle centroid, corrected by normalizing the thickness measurements to the minor axis of the ellipse fitted to the left ventricle centroid.

4.3 Results and Discussion

The results for fibrosis fraction and left ventricular wall thickness centered at the region of fibrosis are summerizd in Table 4.1 for various treatment conditions. Long-term studies for healing process and maturation of the myocardium treated with MCET to assess the potential therapeutic effect (*Lu et al.*, 2016) were planned in Group A and B. The objective of Group C to H was to evaluate adjuvant treatment effect of the steroid MP and Losartan, in terms of inhibition of fibrous tissue formation during the long-term healing process to achieve final muscle wall reduction.

4.3.1 Lesion Maturation

The quantified fibrosis fraction within the treatment volume indicates the fraction of cardiomyocyte removal, which is much higher in group B than in group A (34±11% vs. 9±6%, $p < 0.001$). The two sets of enhanced therapeutic parameters were used to induce injury in rat hearts and to test the long-term outcome and tolerance of MCET. Increased trigger intervals (from 1:4 to 1:8) and pulse durations (from 5 to 10 cycles) induced more damage (*Miller et al.*, 2014a). Moreover, square envelope modulation at the highest PRPA had a larger effective macrolesion volume in terms of integrated refractional pressure over time, compared with the Gaussian modulation (*Zhu et al.*, 2015b). On the basis of these findings, we chose a set of parameters with higher effect (pulse duration of 10 cycles, 4-ms square modulation, 1:8 trigger for 10 min) and another with lower effect (pulse duration of 5 cycles, 15-ms Gaussian modulation, 1:4 trigger for 5 min). The difference between the two groups illustrates the range of therapeutic impact that can be achieved by respective exposure parameter selection. As expected, higher exposure used in group B yielded more substantial injury than lower exposure in group A. This was confirmed by the extent of fibrosis after 6 wks.

4.3.2 Adjuvant Treatment

A preliminary chronic test was conducted in the Groups C-E to assess the utility of losartan and low dose MP as adjuvants to reduce the long-term scar formation in the treated region. The fraction of scar formation in the treated region was not affected significantly by the initial low dose MP dosing nor, by the follow-up losartan treatment. Nevertheless, both low dose MP and losartan were included in the chronic study with the HCM-model rats in Groups F-H based on the toleration of the treatments and the earlier published findings (*Frimm et al.*, 1997; *Roberts et al.*, 1985). Group F and G were analyzed separately though the acute treatments were performed the same way due to their significantly different responses to the therapy, premature complexes in the ECG generation and troponin release (*Miller et al.*, 2011). Group G showed substantial fraction of fibrotic scar area at 42% in the treatment region, and wall shrinkage of 2.29 mm compared to 2.74 mm in sham Group H.

4.3.3 Discussion

Massons trichrome staining revealed that up to 49% tissue in the center of the treated area was involved in fibrotic lesions. The lesions were scattered and randomly distributed in the anterior wall without gross tissue structure destruction. This may be less severe for the tissue reduction in the treatment of HCM with fewer side effects, compared with traditional invasive septal reduction. Although the percentage of tissue damage is substantial for Group B, no obvious shrinkage of wall thickness was observed when measured with echocardiography. No consistent difference in wall thickness among sham, A and B groups was found on histology 6 wks after treatment, although some indications of wall thinning were noted in the high-exposure group. The unevenness and variation of the left ventricular wall thickness in the histologic sections preclude the identification and measurement of small changes in wall thickness. However, the study with adjuvant treatment demonstrated a significant and

therapeutically useful magnitude of tissue reduction observable histology (16%) relative to sham. Damaged microlesion areas seemed to be almost completely replaced by fibrotic tissue formation following the acute inflammation after cavitation-induced injury. This is characteristic of the normal replacement process in which fibrosis and scar preserve the structural integrity of the heart, for example, after ischemic injury (*Baroldi*, 1975). The inflammation and replacement scar volume seen here may be amenable to pharmaceutical intervention. For comparison, in human HCM patients with surgical myectomy, the interventricular wall thickness was reduced by 18% from 19.4 to 15.9 mm (*Brown et al.*, 2011).

4.4 Conclusion

Here, with quantitative measurements of the fibrotic tissue fraction and heart muscle wall change induced by MCET after a long-term healing process, we believe we have demonstrated that MCET is promising as a minimally invasive myocardial tissue reduction addition to HCM treatment options. We have presented ultrasound myocardial cavitation enabled treatment as an image-guided method capable of graded and diffuse tissue reduction with potentially minimal adverse side effects, relative to alcohol ablation or other methods. We have shown that the MCET method can be improved by addition of adjuvant treatment with steroid and antifibrotic medication. The chronic study in the SS-16^{BN} rat model of HCM has shown that the MCET method is able to significantly reduce wall thickness by about 16%, which is of therapeutically useful magnitude. After further development and refinement, MCET treatment for HCM could fill the need for a new treatment option.

CHAPTER V

Development of Monitoring Cavitation as Treatment Feedback

5.1 Introduction

Hypertrophic cardiomyopathy (HCM) occurring in 1 of 500 people can lead to sudden death to adults without prior indication (*Maron and Maron*, 2013). Echocardiography is one of the most common ways to diagnose hypertrophic cardiomyopathy. Current treatment involves invasive and high-risk procedures such as surgery or catheter-based ablation (*Marian*, 2009). A novel technique, named Myocardial Cavitation-Enabled Therapy (MCET), was proposed as a means to achieve minimally invasive myocardial reduction (*Miller et al.*, 2014a). It has demonstrated the possibility for shrinking targeted hypertrophic heart muscle over time without substantial scars (*Lu et al.*, 2016). The treatment employs contrast echocardiography at higher than diagnostic pressure amplitudes, to produce scattered microlesions (regions of lethally injured cells) by introducing cavitating contrast agent microbubbles. Previous studies of MCET have proven the efficacy of MCET to induce damage. The micro-scale surgical impacts of local cardiomyocyte necrosis and microscopic lesions, can accumulate with time to a desired total impact (*Miller et al.*, 2014a,b, 2015; *Zhu et al.*, 2015a,b). Biological responses to the MCET, e.g. premature electrocardio-

gram complexes from ECG (*Miller et al.*, 2011), only serve as temporal qualitative indicators for bioeffects. Other measurements, such as troponin levels and echocardiography (*Miller et al.*, 2014a) right after treatment provide only the qualitative information of the overall accumulated impact. A monitoring scheme for microbubble cavitation during the treatment process is beneficial for treatment control, and a spatial indicator is needed for localizing treatment effects.

Active ultrasound imaging of appearance change or presence of bubbles in the medium has been incorporated in cavitation detection (*Gateau et al.*, 2011). However, the imaging ultrasound pulses may interfere with cavitation signals resulting in ambiguity of identifying cavitation. Passive acoustic imaging technique avoid this by using an array to passively record cavitation emissions followed by beamforming of the recordings to estimate the distribution of cavitating sources, and as such, allow real-time spatiotemporal monitoring of cavitation activity in the field of view of an ultrasound transducer. Passive imaging in 2D has been proven to outperform B-mode in accessing HIFU ablation (*Jensen et al.*, 2012), and also been extended to 3D (*Collin et al.*, 2013). Its feasibility was verified with magnetic microbubbles (*Crake et al.*, 2015) and for short pulse insonations as well (*Haworth et al.*, 2012). Synchronization of the cavitation inducing transducer with the imaging transducer provides better axial resolution. Microbubble cavitation imaging for sonothrombolysis was demonstrated using a single probe (*Vignon et al.*, 2013). Pulse sequences were designed as ultrafast imaging, interleaving destruction pulse and passive cavitation detection interval to monitor bubble activities (*Xu et al.*, 2014).

This chapter discusses several possible schemes for monitoring microbubble cavitation for MCET including quantification and imaging, which will assist future *in vivo* studies for real-time temporal and spatial detection of microlesion formation.

5.2 Methods and Materials

5.2.1 Linear Scatters vs. Microbubbles

5.2.1.1 Experimental Setup A: Separate HIFU and Receive

Microbubbles, ultrasound contrast agent (USCA) of Definity (Lantheus Med. Imag., Billerica, MA), were diluted into phosphor buffered saline (PBS, pH=5.0) and pumped at a maximum velocity of 4 cm/s in a 1.5 cm diameter thin walled dialysis tubing setup. Polystyrene spheres of 5 μm diameter (2005ATS, Duke Scientific, Palo Alto, CA) as linear scatterers were diluted to 0.15 g/1100 mL in a water and glycerol suspension, to compensate for the larger mass density of the spheres relative to PBS. Spectral data from the linear scatterers was compared to that of USCA for compensating the system transfer function.

A preclinical ultrasound imaging system with a single element high intensity focused ultrasound (HIFU) transducer, synchronization and a receive-only imaging array has been implemented on a research platform (Verasonics Inc., Redmond, WA).). Single element transducers A314S (Panametrics, MA) and A381S (Panametrics, MA) at 1.0 MHz were driven in burst mode at 3.5 MHz, respectively serving as the HIFU transducer with focal lengths both of 3.8 cm. The HIFU transducer was operated at a pulse repetition frequency (PRF) of 22 Hz with ten-cycle burst and with a peak-to-peak acoustic pressure of up to 5.5 MPa at its focus. A 128-element linear array (L7-4, ATL, Seattle, WA) was employed in receive-only mode. Then the HIFU transducer was fired with its focus in the center of the dialysis tube. The L7-4 imaging array was used as a passive cavitation detector and was placed at an angle of 32 degrees with respect to the acoustic axis of the HIFU transducer. Therefore the imaging plane becomes an ellipse instead of a circle as illustrated in Figure 5.1.

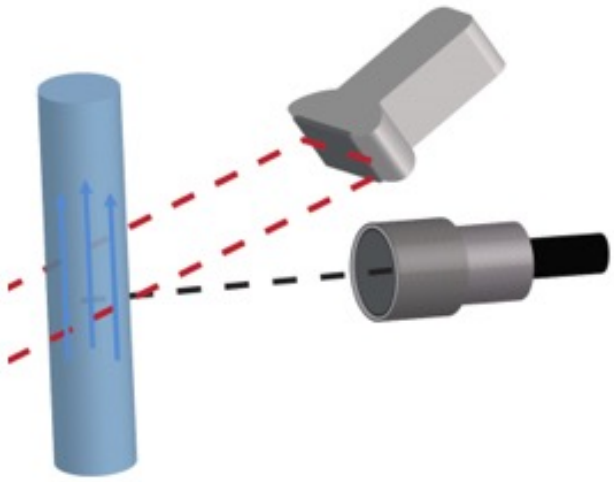

Figure 5.1: The HIFU transducer was fired with its focus in the center of a thin walled dialysis tube. The imaging array used as a passive cavitation detector and placed at an angle of 32 degrees with respect to the acoustic axis of the HIFU transducer.

5.2.1.2 Signal Processing Algorithm

A cavitation mapping technique (*Vignon et al.*, 2013) was employed to spatially localize and depict microbubble activity during HIFU exposure, and ready to be used during treatment and to monitor microlesioning *in vivo* in real-time. The acoustic emissions and scattered radio frequency (RF) signal from the volume of interest was beam-formed by a delay-and-sum algorithm followed by signal maximum hold after filtering f_0 (the driving frequency) and $2 \times f_0$. The resulting so-called non-harmonic frequencies exclude fundamental and harmonic as shown in Figure 5.2, and thus give strong evidence of any cavitation activity. Beamforming on this filtered signal yields spatial mapping of cavitation.

5.2.2 Microbubble Cavitation Detection

As described in section 1.2.1, there are two types of cavitation, stable cavitation and inertial cavitation. Detection of emissions at the subharmonic (one-half the driving frequency, $f_0/2$, where m is an integer and f_0 is 1.5 MHz) and ultraharmonic

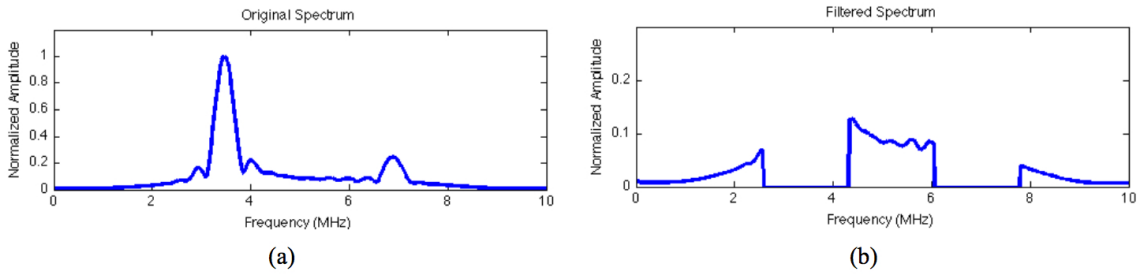

Figure 5.2: (a) Frequency spectrum of passively detected raw RF signals, (b) filtered non-harmonic spectrum for subsequent beamforming. (*Zhu et al.*, 2017)

(odd harmonics of the subharmonic, $(2m+1) \times \frac{f_0}{2}$) bands the inharmonic bands is an indication of stable cavitation within an insonified bubble population. Inertial cavitation results in substantial broadband emissions (*Haworth et al.*, 2012).

5.2.2.1 Experimental Setup B: Combined HIFU and Receive

The experimental setup is similar to that described in section 5.2.1.1 with some modifications, as provided next. A Definity® substitute was employed as USCA, diluted into phosphor buffered saline (PBS, pH=5.0) and pumped into a 1.5 cm diameter dialysis tubing setup. Microbuble vials were activated at room temperature, using a 45-s activation cycle. As the kinetic energy of the shaking results in heating the fluid, the vials were allowed to return to room temperature over 60 min. The agent was diluted by factors of 100, 200, 400, 800 and 1600 by volume into saline to achieve a number density of approximately 8×10^4 USCA/mL for 1:100 dilution.

Flow was maintained at 50 mL/min with a pump (model 77200-62, Masterflex, Gelsenkirchen, Germany) in continuous withdrawal mode. A 96-element phased array (P4-1, ATL, Seattle, WA) operated on a Verasonics platform serving as both HIFU output transducer and receiving passive imaging transducer, like in regular pulse-echo imaging mode. Thus, one acquisition involves RF traces from 96 receiving channels. The HIFU transducer P4-1 was operated at a 1.5 MHz center frequency, 2 Hz duty cycle, firing a ten-cycle tone burst at a 4kHz PRF for 20 repetitions. Ultrasound beam

was focused at 7 cm away in the center of the dialysis tube. The imaging plane of the array was placed perpendicular to the tube. This setup assures the microbubbles replenish at 2 Hz but remain almost at steady state within the focal volume during the firing of the 20 pulses.

Acoustic pressures (peak rarefactional pressure amplitude (PRPA) of 0.48 - 4.4 MPa in 18 increments, for various microbubble concentrations) were cycled through ten times, randomizing the order of excitation pressures at the beginning of each cycle, yielding ten excitations at each acoustic pressure per data set. The experiments were performed with 40 measurements per exposure parameter (USCA concentration, acoustic pressure) for averaging.

5.2.2.2 Cavitation Detection Processing

Scattering from the tube walls dominated the passively received signal. Received signals from degassed water were used to estimate tubing walls in the time domain, and a Hamming window was applied between tube walls to extract signals only within the tube for each channel out of the total of 96. To eliminate acoustic clutter from non-bubble scattering and compensate for the system transfer function, power spectra from saline controls were subtracted from USCA power spectra in the frequency domain.

Cavitation detection was performed based on power spectra of received RF signals. For each acquisition, an average spectrum, computed in MATLAB (MathWorks Inc., Natick, MA), was obtained across 96 channels. Here, as shaded spectrum indicated in Figure 5.3 left, the power spectrum bands were summed over a 2-kHz bandwidth, centered around each spectrum band of interest. Spectrum band center at $3f_0/2$ was used as a signature for stable cavitation noted as UH (ultraharmonic), and the band center at $2f_0$ was used an indicator for nonlinear propagation, noted as 2H (second harmonic). Broadband signature, noted as BB (broadband), indicating inertial cav-

itation, of the power spectrum were defined as the sum power for frequency bands centered at each $(\frac{1}{4}f_0 + \frac{nf_0}{2})$ and within a band width of 2 kHz, where n is a positive integer larger than zero. These bands were chosen to include only the transducer bandwidth of 1-4 MHz. Finally, $3f_0/2$, $2f_0$ and broadband signatures were obtained by averaging across measurements.

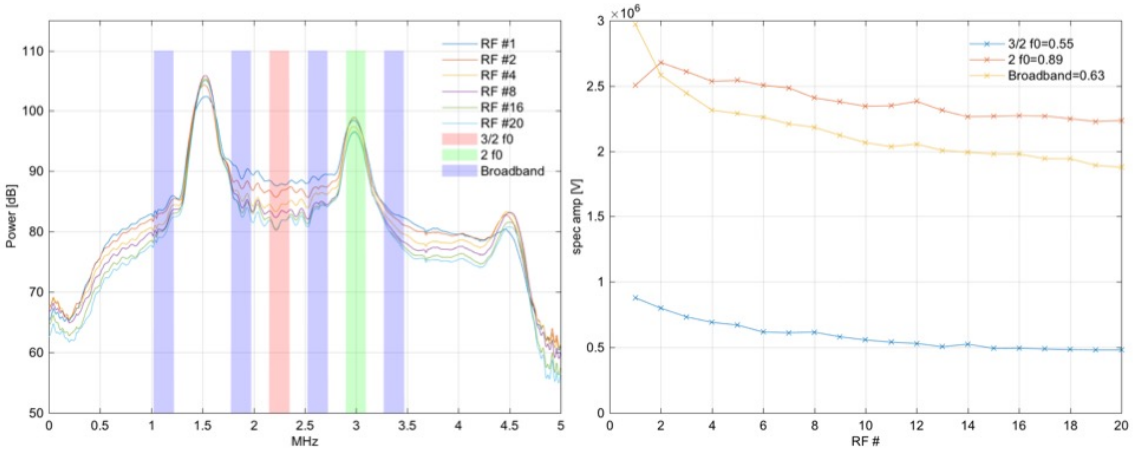

Figure 5.3: Power spectrum and microbuble signatures against the sequential number pulse RF at PRPA of 4.3 MPa with microbubble concentration of 4×10^4/mL. Left: power spectrum for acquired RF number 1, 2, 4, 8, 16 and 20 pulse out of 20 pulses at 4 kHz for one firing with shaded spectrum used for extracting bubble signatures. The spectrum band center at $3f_0/2$ (red shading) was used as a signature for stable cavitation, and the band center at $2f_0$ (green shading) was used an indicator for non-linear propagation. Broadband signature (blue shading), indicating inertial cavitation, of the power spectrum were defined as the sum power for frequency bands centered at each $(\frac{1}{4}f_0 + \frac{nf_0}{2})$ and within a band width of 2 kHz, where n is an integer. These bands were chosen to only include the transducer bandwidth of 1-4 MHz. Right: $3f_0/2$, $2f_0$, broadband signatures plotted against the acquired RF pulse number 1-20. (Setup B)

5.2.3 Passive Cavitation Imaging

Passive cavitation imaging processes the cavitation emissions passively received with an array to map emissions from an unknown location (*Gyongy et al.*, 2008; *Salgaonkar et al.*, 2009; *Farny et al.*, 2009).

5.2.3.1 Imaging Algorithm

Passive cavitation imaging using a delay, sum, and integrate algorithm to beamform the acoustic emissions received on a passive array has been previously described (*Haworth et al.*, 2012). This algorithm is based on the assumption that signals originating from a single source and arriving at different elements of an array will be coherent, though arriving at different times based on the time of flight from the source to each individual element (Figure 5.5(a)). Figure 5.4 shows the relationship between an image location $\vec{x}$ and the array. To form an image, the received signals are individually temporally delayed based on the propagation times between the receiving elements and the spatial location that the pixel represents. The waveforms are summed across the receiving elements and, due to their coherent nature, add constructively if the location of the pixel represents the source location (Figure 5.5(b)). If the received signals are time delayed using propagation times to a location that is far from the source, the waveforms will not add fully constructively (Figure 5.5(c)), resulting in a lower amplitude and less energy. After summing over channels, the frequency-dependent energy in the summed waveform was computed and used to assign a pixel value at that location.

The frequency dependent image at location $\vec{x}$, $B(f, \vec{x})$, is defined in Equation 5.1, where $S_n(f)$ is the **frequency domain** representation of the signal received on the n^{th} element of the passive array located at $\vec{x_n}$

$$B(f, \vec{x}) = |\sum_{n=1}^{N} S_n(f) e^{i2\pi f \frac{|\vec{x_n} - \vec{x}|}{c}}|^2 \tag{5.1}$$

The pixel amplitude is determined from the energy (or power) of the interest for certain frequency bands in the summed signal $B(f, \vec{x})$. To form a complete image, the energy at each desired pixel location is computed. The algorithm for computing

the pixel amplitude $B(\vec{x})$ at location $\vec{x}$ is mathematically written as in Equation 5.2

$$B(\vec{x}) = \int_{f_1}^{f_2} B(f, \vec{x}) df \tag{5.2}$$

where f_1 and f_2 define the lower and upper frequency band limits, respectively. Composite images are useful when the bandwidth of interest is finite. Furthermore, incoherent noise will be reduced in this multifrequency composite images relative to a single-frequency image.

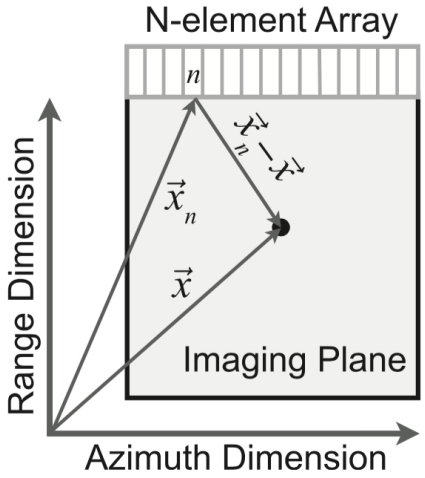

Figure 5.4: Schematic of passive imaging array and corresponding imaging plane. The n^{th} element of the array is labeled and the black dot indicates pixel or region of interest location $\vec{x}$. The elevational direction is out of the plane of the page. (*Haworth et al.*, 2012)

5.2.3.2 Experimental Setup

Experiment C: Combined HIFU and Receive - To verify the feasibility of passive cavitation imaging in our system, the experiment to record data was set up with a more confined microbubble 'carrier'. The layout of the experiment is similar to Figure 5.1 but instead of dialysis tubing, a one-way flow consisting of a micro-polyurethane tubing (inner diameter-203 μm, outer diameter-356 μm, Catalog # PE-8-25, Strategic Applications Incorporated, Libertyville, IL) was used to direct

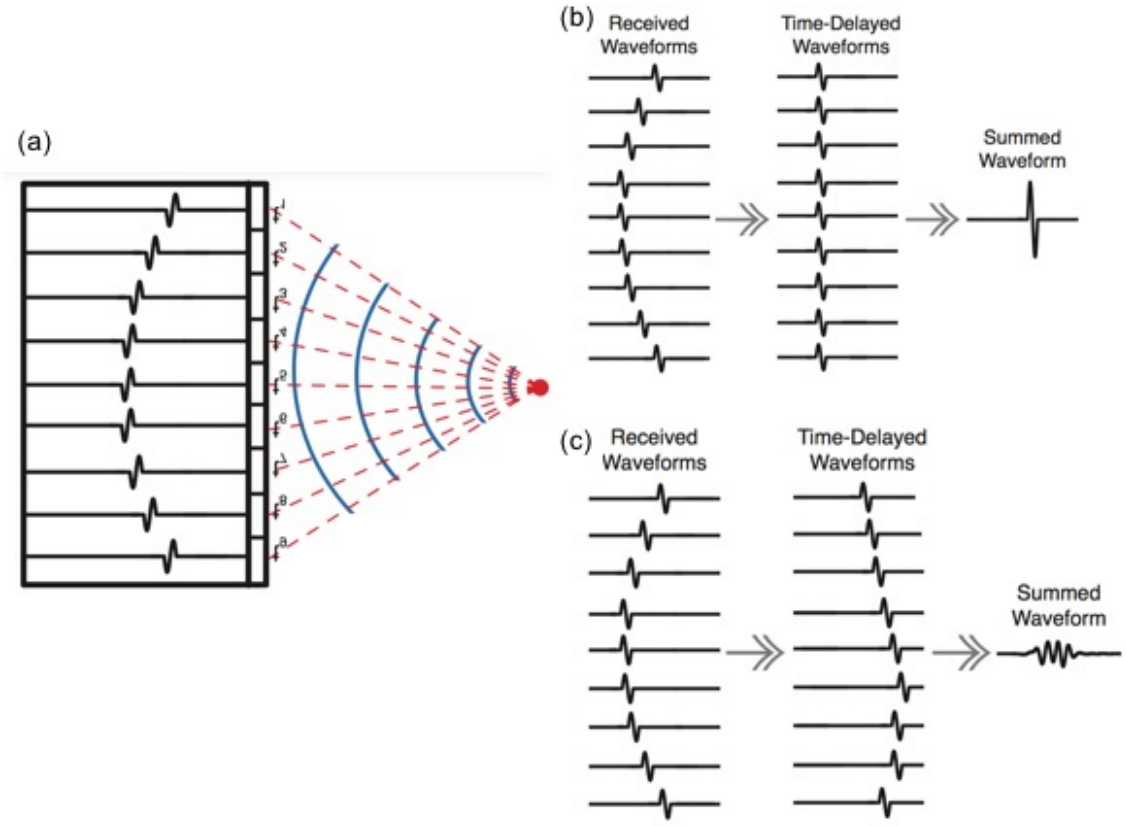

Figure 5.5: Schematic illustration of delay, sum, and integrate algorithm. (a) An acoustic pulse is emitted from a point source (red circle). Solid blue lines: wavefronts. Red dashed lines: acoustic propagation paths, each with a corresponding time of flight. Black outlined rectangles: array elements. The recorded waveforms for each element are shown as a single-cycle pulse arriving at different times. (b) When $\vec{x}$ corresponds to the source location and is used to compute the time delays to shift the waveforms, the waveforms will sum constructively. (c) When $\vec{x}$ is a location away from the source, the time-delayed waveforms do not fully add constructively and the summed waveform has a lower amplitude and less energy. (*Haworth et al.*, 2016)

the solution from the bottom of the reservoir through the region of insonification. A phased array P4-1 was employed as both high intensity output transducer and passive receiving one via the Verasonics system.

Experiment D: Separate HIFU and Receive - Another experiment system for validation of passive imaging algorithm to identify multiple cavitating locations was established. A 298-element, concentric array (Imasonic SA, Besancon, France) was driven by an in-house high power system for therapeutic excitations. The phased array P4-1 on Verasonics was operated on receive-only for cavitation detection and B-mode imaging for aiming. A phantom with 3M iM30K Hi-Strength Glass Bubbles (3M, St. Paul, MN) suspended in ultrasound gel was employed as the medium. The HIFU system focuses at 12 cm away and fires 12 pulses at 4 kHz with 4 pulses at each location being 5 mm apart as illustrated by hyperechogenicity in a B-mode image recorded with the P4-1 in Figure 5.11 (a).

5.3 Results

5.3.1 Linear Scatters vs. Microbubbles Imaging

Results in this section are from Setup A. Acoustic emissions from USCA reached from the fundamental to the 8^{th} harmonic for a 1.0 MHz excitation and were detectable within the bandwidth of the L7-4 for all tested dilutions (25 μL, 50 μL, 100 μL, 200 μL stock per liter saline). Ratios of higher harmonics to fundamental frequency increased with drive pressure and exceeded 5 dB.

Results for excitation at 3.5 MHz center frequency are shown in Figure 5.6(a)(c)(e). Three pressure levels were used. Acquisitions with higher acoustic pressure yielded higher signal to noise ratios, that in turn were ascribed to more cavitation events. To ensure that the detected signals were generated from the active agents rather than the acoustic field, a set of control experiments were performed with polystyrene spheres.

Results are shown in Figure 5.6(b)(d)(f).

No cavitation was detected with a low pressure excitation at 0.31 MPa of spheres, shown in Figure 5.6(b). Greater contrast in beamformed images resulting for exposure of USCA (Figure 5.6(a)(c)(e)) than images formed for polystyrene spheres (Figure 5.6(b)(d)(f)) was assumed to provide evidence of the existence of microbubble cavitation events.

At 2.8 MPa peak-to-peak pressure, USCA yielded a 5 dB higher signal compared to polystyrene spheres (Figure 5.6(e)). Mapped cavitation signals were observed laterally within 1.5 mm of the HIFU transducer focus and axially within approximately the spatial pulse length of 4.5 mm as shown in Figure 5.7.

5.3.2 Microbubble Cavitation Detection

The results in this section are from Setup B presenting influences of microbubble cavitation detection resulting from various 1) number of repetitive ultrasound pulses 2) ultrasound pressure amplitude 3) microbubble concentration, respectively.

5.3.2.1 Repetitive Ultrasound Pulses

One HIFU firing involves 20 repetitive pulses at 4 kHz. Figure 5.3 shows the power spectrum of some representative pulses within one pulse series and cavitation signatures plotted against the acquired RF pulse number 1-20. The decreasing trends of bubble signatures reveal the destruction of microbubbles.

5.3.2.2 Pressure Dependence

Microbubble activity was investigated against acoustic pressure change for various microbubble concentrations as shown in Figure 5.8 left. As acoustic power increases, cavitation signatures from received signals for the first RF pulse out of 20 increases until it saturates for increasing power. Energy for $2f_0$ clearly increases to a point

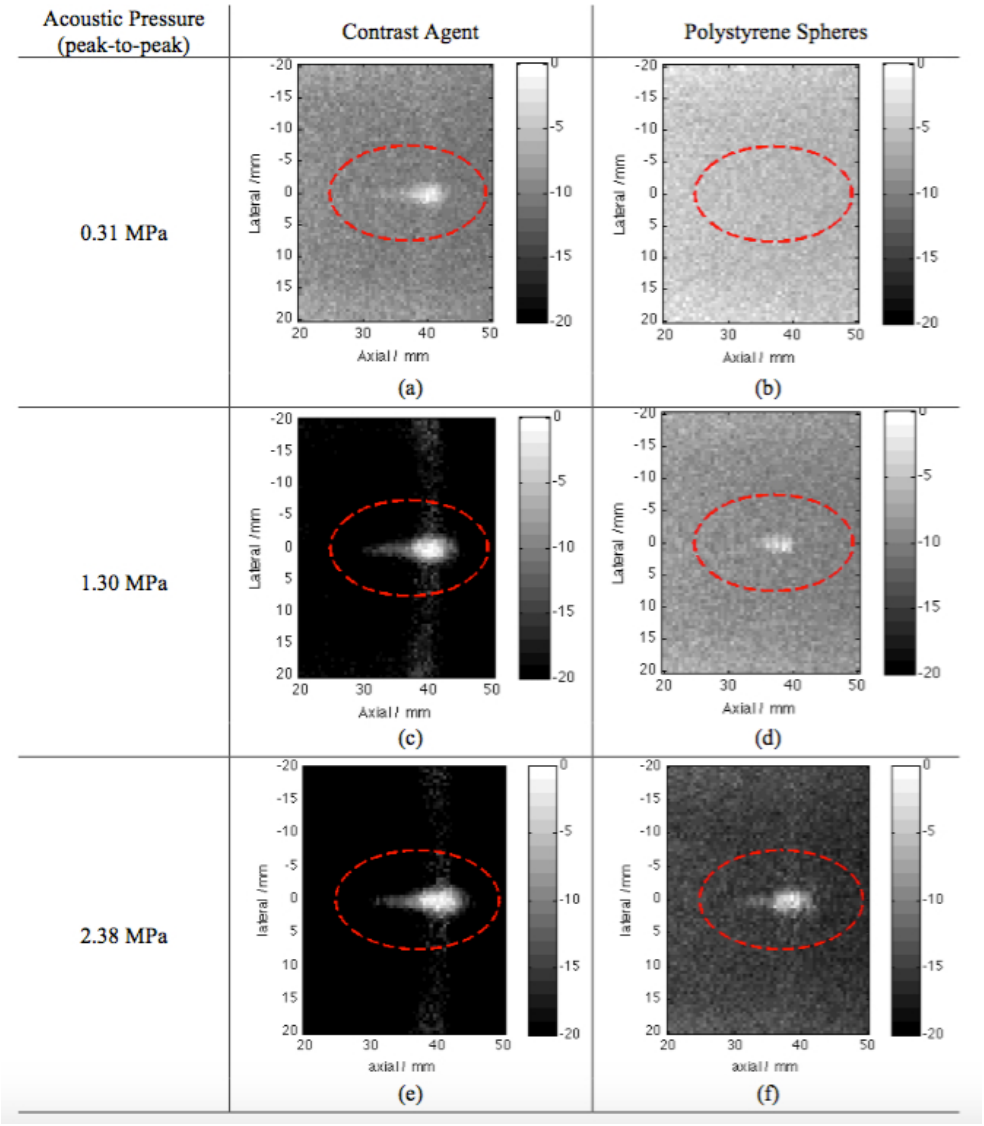

Figure 5.6: Passive imaging results (Setup A) for 3.5 MHz excitation and acoustic pressures of (a) (b) 0.31 MPa, (c) (d) 1.30 MPa (e) (f) 2.38 MPa for contrast agent (a) (c) (e), and for polystyrene spheres (b) (d) (f) with the red dotted ellipse delineating the imaging plane intersected with the dialysis tube. (*Zhu et al.*, 2017)

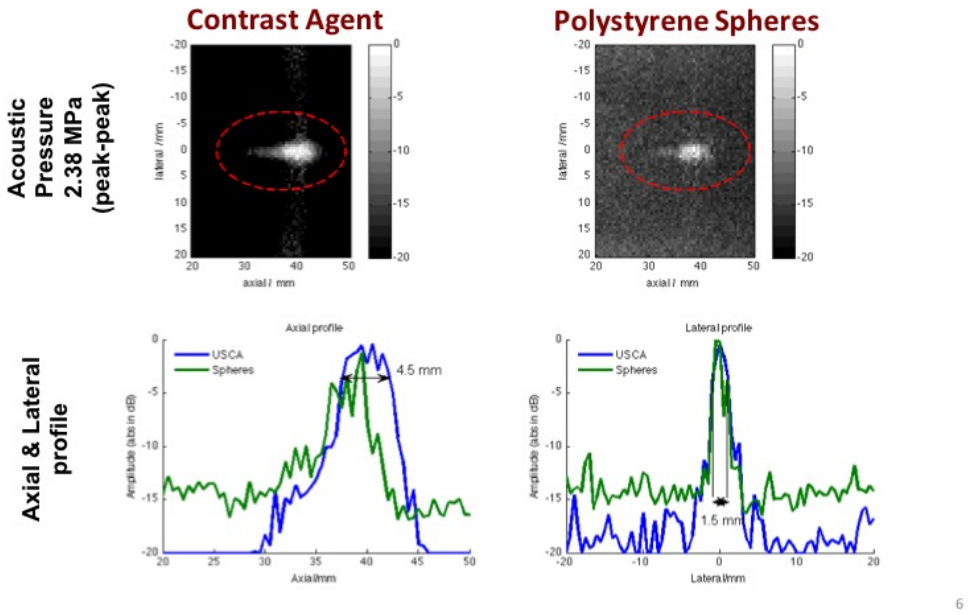

Figure 5.7: The result (Setup A) for high acoustic pressure enables us to resolve a 5 dB difference between contrast agent and spheres. The spatial resolution is 4.5 mm for axial and 1.5 mm laterally.

and starts to decrease, implying energy transition to other frequency components. Signatures of broadband and $3f_0/2$ seem to keep increasing as acoustic power go up for both bubble concentrations 2×10^4/mL and 4×10^4/mL. However, for bubble concentration of 8×10^4/mL, broadband signature seems to saturate and decrease after 2.7 MPa PRPA.

5.3.2.3 Microbubble Concentration Dependence

The cavitation signatures from received signals for the first RF pulse out of 20 were investigated against microbubble concentration for various acoustic pressures as shown in Figure 5.8 right. The signatures increase reasonably as concentration increases indicating more microbubble were acoustically active.

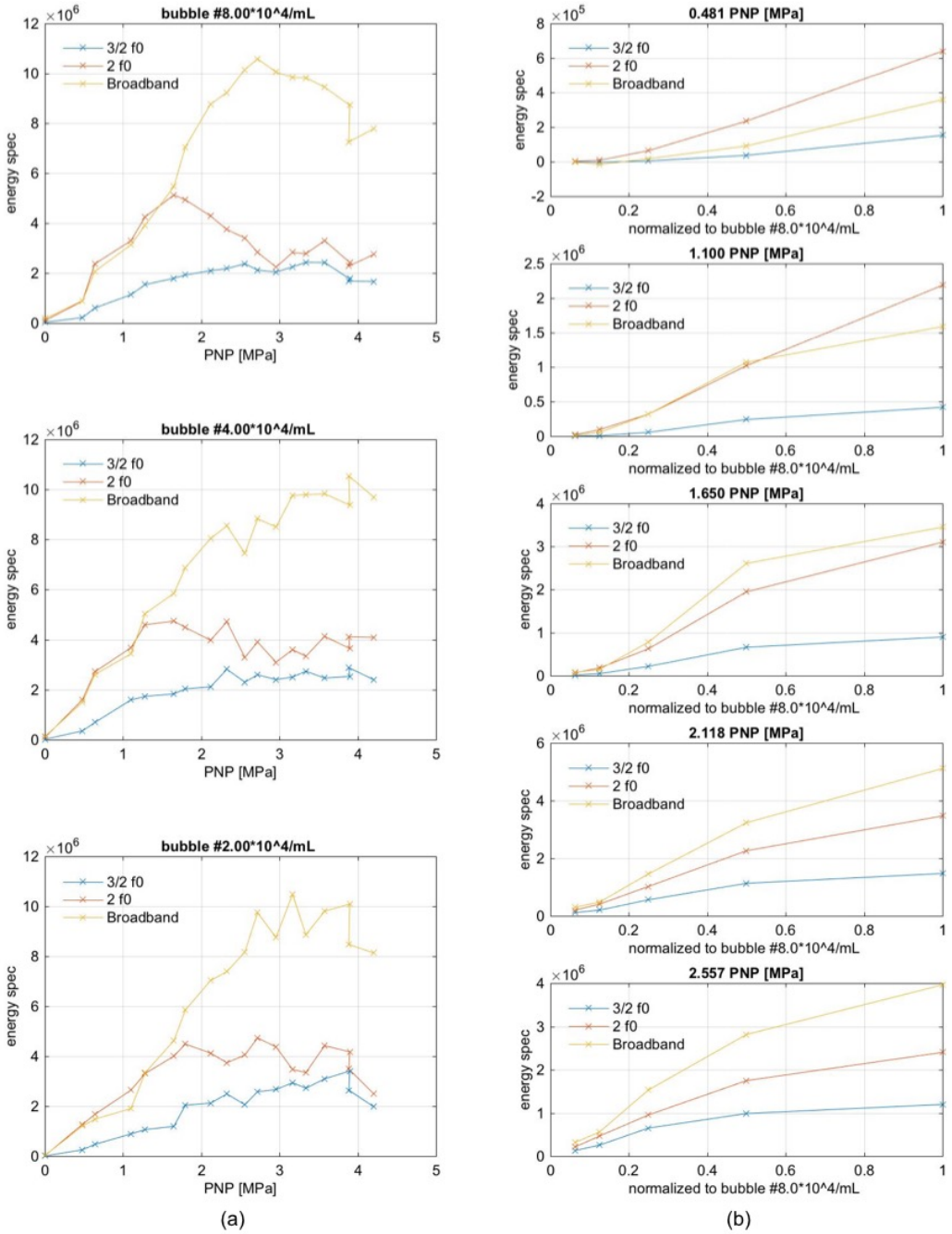

Figure 5.8: Microbubble signatures from received signal for the first RF pulse out of 20 increases for acoustic variation and microbubble concentration variation. Left: acoustic influence on microbubble signatures for various microbubble concentrations. Right: influence of microbubble concentrations on microbubble signatures for various acoustic pressure. (Setup B)

5.3.3 Passive Cavitation Imaging

Broadband signals as described in section 5.2.2.2 were beamfored by passive cavitation imaging using Setup C.

5.3.3.1 Frequency-Domain Imaging

Passively beamformed image on broadband frequency components using frequency-domain is shown in Figure 5.9, with 0.25 cm wide 6 dB lateral resolution and 5 cm wide 6 dB axial resolution.

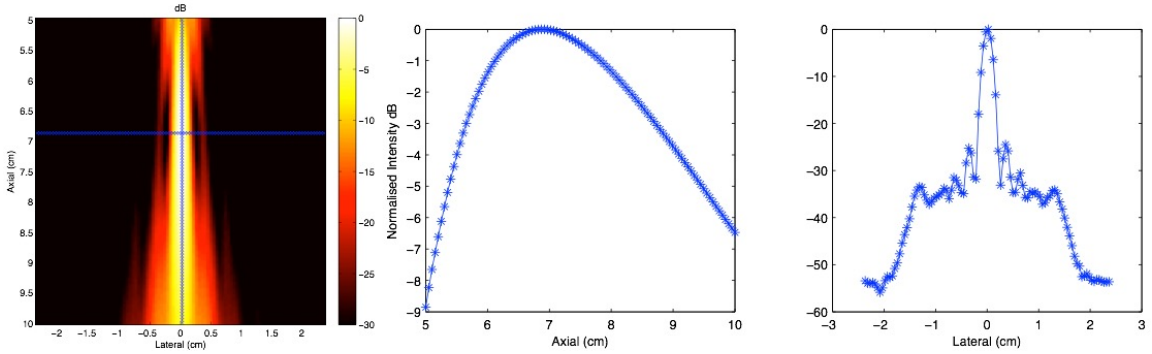

Figure 5.9: 2D (left), axial (middle) and lateral (right) cross-sections for passively beamformed cavitation image. (Setup C)

A variation of frequency-domain passive cavitation algorithm demonstrated called frequency-sum beamforming (*H. Abadi et al.*, 2013), which employs second-order or higher products of the acoustic emissions of Equation 5.1 to manufacture higher frequencies, thereby reducing the size of the point spread function (PSF). Improved resolution with frequency-sum algorithm beamformed at $2f_0$ (Equation 5.3) and $4f_0$ (Equation 5.4) has been seen using the same input data as shown in Figure 5.10.

$$B(f,\vec{x}) = |\sum_{n=1}^{N}(S_n(f)e^{i2\pi f\frac{|\vec{x_n}-\vec{x}|}{c}})^2|^2 \tag{5.3}$$

$$B(f,\vec{x}) = |\sum_{n=1}^{N}(S_n(f)e^{i2\pi f\frac{|\vec{x_n}-\vec{x}|}{c}})^4|^2 \tag{5.4}$$

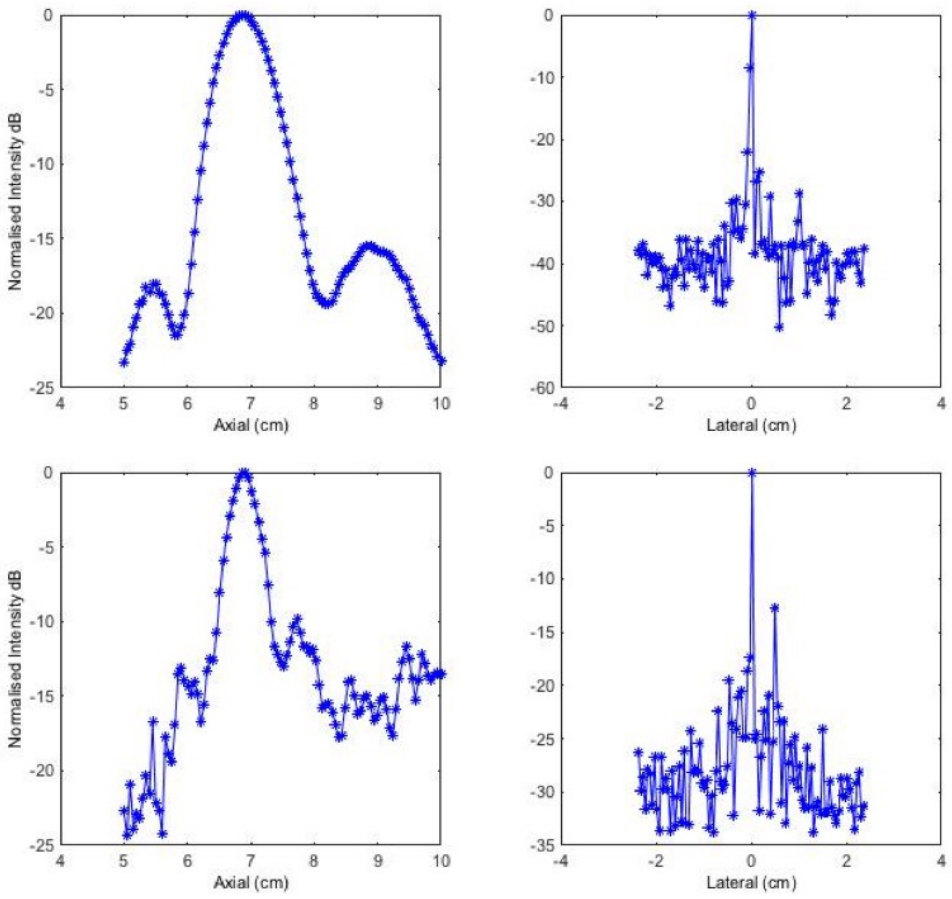

Figure 5.10: Axial and lateral cross-sections images beamformed using the frequency-sum algorithm at $2f_0$ (upper) and $4f_0$ (bottom). (Setup C)

5.3.3.2 Cavitation Location Imaging

Hyperechogenicity in B-mode imaging from P4-1 delineated cavitating locations of the HIFU system using Setup D, as shown in Figure 5.11(a) with a overlaid zoom-in window. Passive cavitation images were beamformed with the received signal shown in a hot map overlaying the B-mode image for 1-4 RF pulses (Figure 5.11(b)), 5-8 RF (Figure 5.11(c)) and 9-12 (Figure 5.11(d)) out of 12 pulses. The lateral resolution is

high enough to distinguish cavitating locations 5 mm apart while the axial resolution is not impressive.

5.4 Discussion

5.4.1 Cavitation Detection

The decreasing energy of cavitation signatures for repetitive ultrasound pulses implies the penetration of ultrasound after destructing the microbubbles closer to the transducer. Thus, the number of pulses needs to be taken into great consideration to achieve a desired depth of effect, especially in larger animal models with acoustic paths at higher attenuation.

With raising acoustic power, cavitation activities increase. The detected change in microbubble signatures positively correlates with bubble concentration. This proved the possibility of the employed system to detect and quantify larger than zero cavitation events. However, some low-level broadband emissions may also result from stable cavitation, due to random bubble motion without inertial collapse, while some subharmonic emissions may result from large-amplitude bubble oscillations preceding inertial collapse (*Haworth et al.*, 2012). Thus, variance of cavitation events quantified by frequency contents may exist. Nevertheless, in MCET treatment monitoring, it would be more interesting to relate detected signals to actual induced therapeutic effects, *e.g.* microlesion distribution, rather than explicitly distinguishing between stable and inertial cavitation.

5.4.2 Imaging Algorithm

The key difference between passive (as used in 5.2.3.1) and B-mode imaging (as used in 5.2.1.2) is that the passive algorithm does not use the absolute time of flight to determine the depth of the acoustic emission (*Haworth et al.*, 2016).

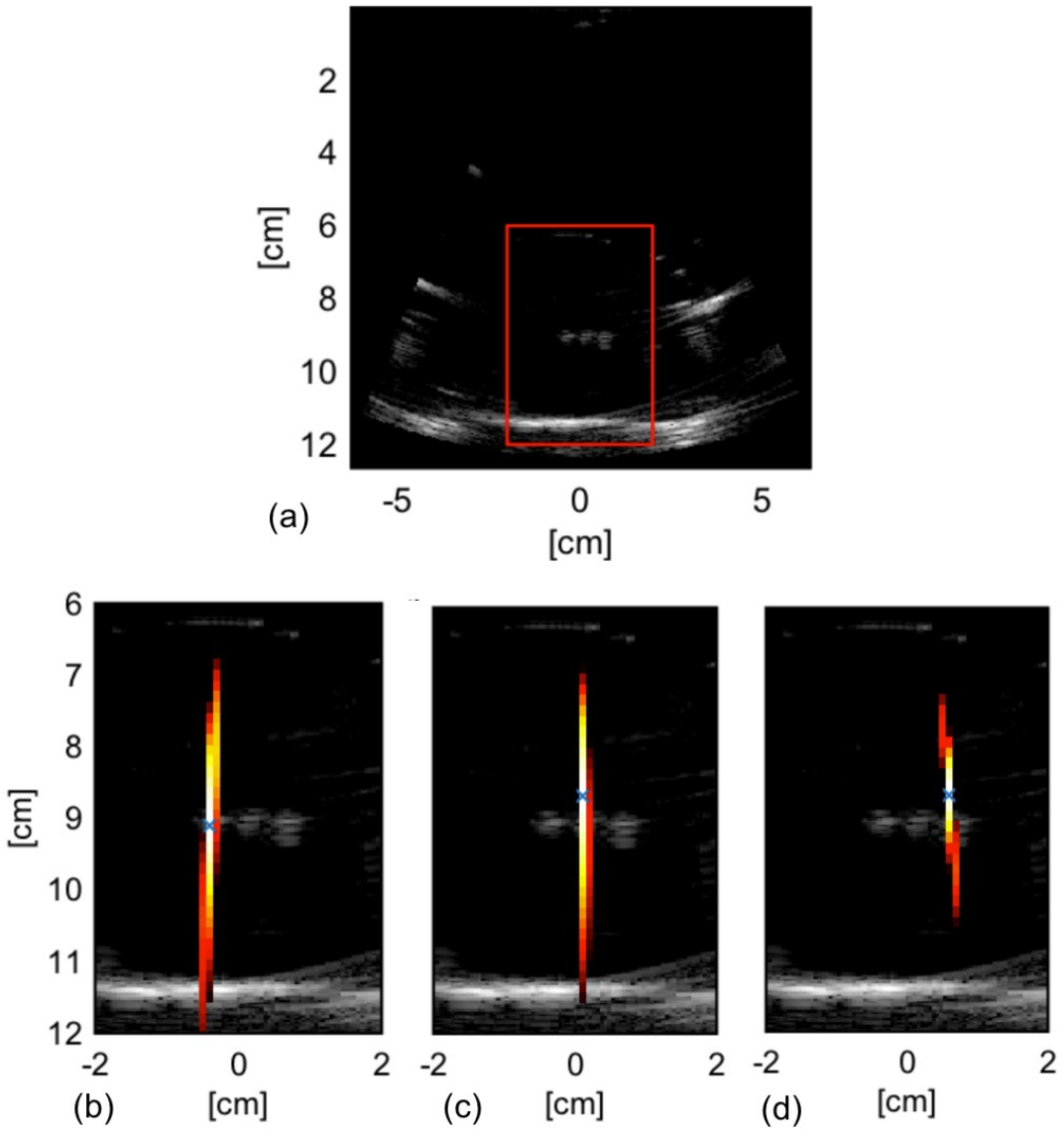

Figure 5.11: (a) B-mode image showing hyperechogenicity cavitating locations with zoom-in window for (b)(c)(d). (b) Passive cavitation imaging (color) overlaid on B-mode image for the 1-4 RF pulses out of 12 pulses. (c) Passive cavitation imaging overlaid on B-mode image for the 5-8 RF pulses out of 12 pulses. (d) Passive cavitation imaging overlaid on B-mode image for the 9-12 RF pulses out of 12 pulses. (Setup D)

The presented results were all beamformed in the frequency domain (*Haworth et al.*, 2012). A first glance, beamforming in the frequency-domain seems more computationally expensive than in the time-domain for its necessity of performing Fourier transform. However, there are several potential advantages for frequency-domain over time-domain analysis (*Haworth et al.*, 2016). Firstly, for the delay, sum, and integrate method, when only some frequency bands of interest need to be beamformed, the computational time compared is largely reduced than beamforming the entire bandwidth (similar to the time-domain approach) (*Arvanitis et al.*, 2015). Additionally, the frequency content of cavitation emissions is often used to characterize cavitation to be stable cavitation or inertial cavitation as discussed earlier. Operating in the frequency domain makes frequency selection simpler and more direct than using time-domain finite impulse response filters. It is also more convenient to select and analyze multiple discrete frequency bands for analysis simultaneously. Another aspect is the temporal quantization error for delaying signals, which time-domain analysis suffers from due to shifting discrete temporal samples. The temporal quantization error can lead to grating lobe artifacts unless the received signals are sampled temporally at a very high sampling rate (often tenfold or higher than the highest frequency of interest) or the received samples are interpolated to approximate a high sampling rate. While in the frequency domain, the time delays become phase shifts where the quantization error is reduced to the floating-point precision.

While a good lateral resolution was presented, the unsatisfactory axial resolution is the major drawback of any passive cavitation imaging algorithm. The axial resolution does not depend on the insonation pulse duration or shape but only the frequency-dependent diffraction pattern of the array (*Haworth et al.*, 2012). Other prior information, or information detected from other sources, e.g. extra detector may help to improve imaging resolution if allowed.

5.5 Conclusion

The systems presented have shown the feasibility of microbubble cavitation detection, quantification and localization. Passive cavitation imaging algorithms provide spatial information of cavitation events. The activities of bubble dynamics and cavitation can be mapped in bench-top setups with a HIFU transducer and a receive-only passive imaging array. The higher acoustic response from contrast agents compared to that from polystyrene spheres in the reconstructed images suggests that cavitation events undergoing inertial cavitation can be detected. Cavitation can be localized with reasonable lateral spatial resolutions. The described passive imaging algorithm applies to both systems: Verasonics alone transmitting HIFU and receiving, and Verasonics only for passive receiving with a HIFU system for therapeutic firing. The overall therapy monitoring system is able to adequately delineate the spatial location of triggered microbubble dynamics. Future work for MCET monitoring involves development of a coefficient or transfer function relating cavitation signals to the extent of induced microlesion, and feasible applications of cavitation imaging techniques for the more compliated *in vivo* enviroment.

CHAPTER VI

Summary

6.1 Summary and Conclusions

6.1.1 Introduction

Hypertrophic cardiomyopathy (HCM) is one of the most common genetic cardiovascular diseases, occurring in 1 in 500 people (*Maron et al.*, 2012). Septal and apical hypertrophies leads to obstruction of the left ventricular outflow path in up to 75% of patients. About one-third of patients with obstruction remain symptomatic after pharmacological therapy and are candidates for tissue debulking (*Marian*, 2009). Two methods presently available are open heart surgery for septal myectomy and transcatheter septal ablation with alcohol (*Members et al.*, 2011). The less invasive alcohol ablation procedure unfortunately has a high incidence of heart blockage requiring permanent pacemaker and of arrhythmia associated with scarring, and is not widely applied (*Maron et al.*, 2003b). A completely new non-invasive option for non-hypertensive, hypertrophic tissue debulking is sorely needed to avoid heart transplants for HCM and avoid long-term effects of ablations and avoid surgery when advisable.

Therapeutic ultrasound is a powerful modality that enables safe, low-cost and non-invasive delivery of energy to targeted tissues located deep within the body for

treatment (*Crake et al.*, 2015). It is highly versatile and readily lends itself to a diverse range of applications in the fields of minimally invasive surgery and targeted drug delivery including thermal ablation (*Illing et al.*, 2005), mechanical tissue erosion (*Roberts et al.*, 2006), blood clots breakdown (*Molina et al.*, 2009) and drug and gene delivery (*Hernot and Klibanov*, 2008). Acoustically active microbubbles are routinely used to improve contrast in conventional ultrasound diagnostic imaging (*Schutt et al.*, 2003) and may also assist with therapeutic effects, in particular those involving acoustic cavitation (*Unger et al.*, 2002).

Myocardial contrast echocardiography (MCE) has enabled enhanced contrast in visualization of myocardial perfusion. Using higher than diagnostic pressure amplitudes in myocardial contrast echocardiography (MCE), Myocardial Contrast Enabled Therapy (MCET), was proposed as a means to achieve minimally invasive myocardial reduction (*Miller et al.*, 2014a). The whole process is as illustrated in Figure 6.1. The treatment employs intermittent ultrasound to destruct contrast microbubbles resulting in lethally injured scattered cells in the focal volume. The micro-scale surgical impacts of local cardiomyocyte necrosis and microscopic lesions, can accumulate with treatment time to a desired total impact. The long-term healing process results in shrinkage of the targeted heart muscle by gradually removing the scattered microlesions (regions of dead cells). The progress has succeeded in advancing the small injury from contrast echo to substantial accumulation of microlesions to form a macrolesion with up to 21% debulking after 4 weeks healing, while retaining reduced function in the target volume. Optimization of parameters and methods avoided potentially harmful premature contraction arrhythmias, reduced the initial swelling and minimized long term scarring for the safe tissue reduction. (*Miller et al.*, 2014a,b, 2015; *Zhu et al.*, 2015a,b; *Lu et al.*, 2016).

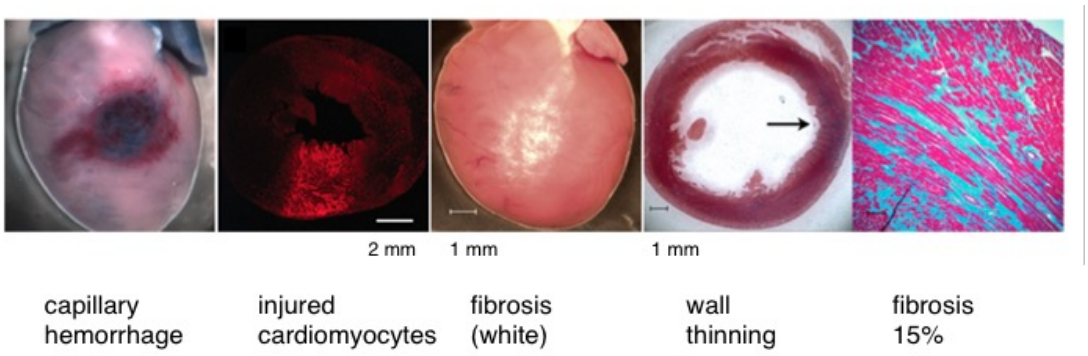

Figure 6.1: From left to right: A freshly exposed rat heart with capillary hemorrhage and Evans blue leakage, frozen section histology showing the lethally injured cardiomyocytes in fluorescent red (bar = 2 mm), a heart after 6 weeks of healing with white fibrosis evident (bar = 1 mm), a cross section of the heart showing fibrosis and wall thinning (arrow, bar = 1 mm), and histology with the fibrotic regions stained blue covering 15% of the area (bar = 100 μm).

6.1.2 Dissertation Summary

To this point, this dissertation has demonstrated the assessment of Myocardial Cavitation-Enabled Therapy (MCET) in acute and chronic studies, and investigates possible monitoring schemes.

In acute studies, Chapter II describes a computer-aided 3-D objective evaluation scheme developed to characterize macrolesions, including lesion size and lesion density, for MCET to reduce myocardial tissue. The characterization is based on brightfield and fluorescence histology images as available in acute preclinical studies. The radially symmetric model employed to characterize macrolesion density is feasible for the study using a single focused beam. This methodology reduces visual scoring ambiguity and provides a volume oriented, quantity-sensitive therapy evaluation. The comparison of characterized macrolesions to the sham group demonstrates that the evaluation scheme is robust against noise. Chapter II presents that the quantitative scoring scheme overcomes the limitation of traditional visual scoring and works for histological cases with a large lesion count, i.e. has an appropriate dynamic range for evaluating therapeutic applications. The presented results have shown that MCET-

induced macrolesions grow radially as the acoustic pressure amplitude increases. A swept beam as a new method to shorten treatment time seems promising but requires additional verification to ensure efficacy.

Based on chronic studies, Chapter IV demonstrates that it is promising for MCET to achieve minimally invasive myocardial tissue reduction by showing quantitative results of the fibrotic tissue fraction and heart muscle wall reduction induced by MCET after a long-term (4 week) healing process. It suggests that MCET is an image-guided method capable of graded and diffuse tissue reduction with potentially minimal adverse side effects, relative to alcohol ablation or other methods. Improvements are identified by addition of adjuvant treatment with steroid and antifibrotic medication. The chronic study in a HCM rat model shows that the MCET method reduced wall thickness by about 16%, which is a therapeutically useful magnitude. After further development and refinement of MCET for Hypertrophic Cardiomyopathy (HCM) should fill the need for new treatment options.

Chapter V investigates the feasibility of microbubble cavitation detection, quantification and localization for treatment monitoring and control. A passive cavitation imaging algorithm and its variations provide spatial information of cavitation events. The activities of bubble dynamics and cavitation are mapped in bench-top setups with a high intensity focused ultrasound (HIFU) transducer and a receive-only passive imaging array. The higher acoustic response from contrast agents compared to that from polystyrene spheres in the reconstructed images suggests that cavitation events from agents undergoing inertial cavitation can be detected. Cavitation sites can be localized with reasonable spatial resolution. The described passive imaging algorithm applies to both systems: Verasonics (an ultrasound research platform) alone transmitting high intensity focused ultrasound (HIFU) and receiving signals with cavitation signatures, and Verasonics only for passive receiving with another HIFU system for therapeutic exposure. The overall therapy-monitoring scheme is

able to adequately delineate the spatial location of triggered microbubble dynamics for real-time monitoring of monitoring of microlesion accumulation.

6.2 Discussion

Hypertrophic cardiomyopathy is caused by an increase in myocyte size, but not myocyte number, and by a greater amount of myocardial fibrosis, which is distributed throughout the interstium and in discrete foci (*Teekakirikul et al.*, 2012). Specifically on the cellular level, the hypertrophy results from cellular enlargement in the adult heart. In addition, structural remodeling of the myocardial cells, including alterations in the relative proportions of cellular organelles and in the ultrastructure of individual organelles, occurs during the development of hypertrophy. In contrast, hyperplasia of myocardial cells happen during embryonic and fetal life which leads to growth of the vertebrate heart by increase in cell number (*Oparil et al.*, 1984).

The idea behind MCET is to achieve myocardial volume reduction by decreasing the population of enlarged cells by inducing scattered microlesions freeing their space.

The possibility of natural regeneration of injured cardiomyocyte is minimal. After cardiomyocyte death, there is no significant replacement of old muscle with new, and a collagen-rich scar is generated by fibroblasts concomitant with removal of cell debris (*Choi and Poss*, 2012). Though numerous research has looked into stem cell based therapies as a potential alternative therapeutic strategy for myocardial regeneration and repair, using for example bone marrow derived stem cells (BMCs), adult stem cells from adipose or cardiac tissue, the current clinical studies haven't demonstrated consistent results (*Doppler et al.*, 2013).

The following addresses some discussion for therapy induced effects and is followed future directions.

6.2.1 Therapy Effects

A variety of interesting arouse during the course of the therapy. This section will touch on some including lesion induction, therapy evaluation and monitoring of heart function.

6.2.1.1 Lesion Induction

As mentioned in Figure 1.2, microbubbles under cavitation may induce a variety of biological responses.

It is possible that a large semi rigid cell adjacent to a small cavitating bubble could induce an asymmetric bubble collapse, by which a small jet of liquid would shoot directly into the cell at sonic speeds, probably rupturing the cell membrane. Likewise a collapse of a microbubble near a capillary or blood vessel wall will cause the liquid jet to shoot right into the wall. The induced liquid micro-jets at sonic velocities may be shooting through cells (and lysing them) (*Pitt et al.*, 2004).

Such may allow large amounts of Red Blood Cell (RBC) and non-destructive microbubbles to extravasate into the nearby interstitial space where microbubbles can be further cavitated to damage cells out of vessels (*Skyba et al.*, 1998).

Other than direct damage induced by the liquid jet, blood vessel become injured by sonic jets, shear stresses, or radicals could generate a nidus for thrombus formation, which may lead to local ischemia. Depending on ischemia duration, two types of cells result: viable cells (reversibly injured), and essentially dead cells (irreversibly injured) (*Jennings et al.*, 1969).

As a schematic illustration of myocardial capillary system, Figure 6.2 shows 5 *mu*m capillaries (*Potter and Groom*, 1983) and 1 *mu*m diameter microbubbles residing interleaved with 30 *mu*m (*Bassien-Capsa et al.*, 2006) cardiomyoctes. This distribution of microbubbles in the vessels makes cavitation adjacent to myoctyes feasible leading to sufficient scattered damage to the myocardium.

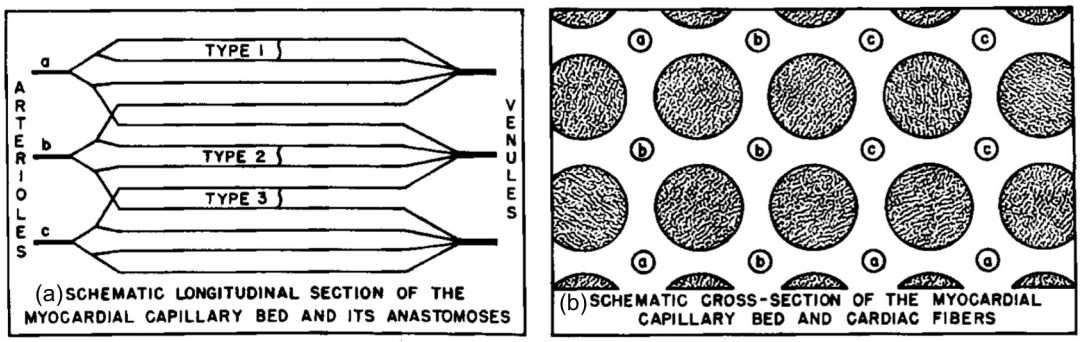

Figure 6.2: (a) Schematic longitudinal section of the myocardial capillary bed and its anastomoses. (b) Schematic cross-section of the myocardial capillary bed and cardiac fibers. (*Brown*, 1965)

The development of MCET has employed Evans blue to identify lethally injured cells. While Evans blue is a vital dye that is reported to penetrate only damaged cells (*Crutchfield et al.*, 1999), some false positive events may exist since damaged or otherwise altered cells may be, though not very likely, capable of repair and be viable. Ceramide may be a possible indicator of cell apoptosis. Its accumulation has been found following treatment of cells with a number of apoptotic agents including ionizing radiation (*Haimovitz-Friedman et al.*, 1994; *Dbaibo et al.*, 1998), UV light (*Rotolo et al.*, 2005), TNF-alpha (*Dbaibo et al.*, 2001), and chemotherapeutic agents. However at this stage, the exact viability of cells is not the main interest. Especially, as described in Chapter IV, the observed level of fibrosis corresponding to therapeutic conditions confirmed that MCET is capable to induce injuries.

6.2.1.2 Therapy Evaluation

The development of MCET suggests that it is an image-guided method capable of graded and diffuse tissue reduction with potentially minimal adverse side effects. A more appropriate comparison for MCET than surgical myectomy (extremely invasive) may be alcohol septal ablation (ASA).

ASA is a minimally invasive procedure to induce a localized infarct for myocaridal reduction. A catheter is threaded through the left anterior descending artery into the

septal perforator with a balloon placed to avoid any antegrade flow into the branch (*Seggewiss et al.*, 1999). After assessment of the area supplied by the artery, for example, by contrast-enhanced ultrasound, several milliliters of ethanol are injected to produce a localized infarct defined by the perfused tissue volume. The procedure typically produces immediate symptomatic relief of the left ventricular outflow tract (LVOT) obstruction (*El Masry and Breall*, 2008). This occurs without direct septal thinning, possibly owing to akinesis of the affected region, which may improve the dynamic motion and LVOT gradient. Septal thinning develops gradually 3-12 mo after the procedure. Reduction of the interventricular septum from 23.7 to 18.0 mm has been reported 6 mo after ASA (*Dabrowski et al.*, 2012), and the treatment may result in reduced myocardial mass involving even remote regions (*Fifer and Sigwart*, 2011). The most common serious complication is disruption of the conduction system, which may include permanent heart block requiring permanent pacemaker implantation (*Sorajja et al.*, 2008).

The ASA procedure results in a volume of necrosis, including occlusion of the artery. This volume progresses to myocardial fibrosis and scar (*Baggish et al.*, 2006), although the healing process is somewhat different from that arising from ischemia, in that minimal phagocytosis and removal of the necrotic cardiomyocytes occur (*Raute-Kreinsen*, 2003). By comparison, the MCET method has a much lower impact on the conduction system and blood vessels because of the scattered nature induced lesion. A more defined macrolesion (region of treatment) can be well controlled by placement of the ultrasonic focus. Electrocardiography (ECG) analysis for MCET revealed evidence of myocardial cell death with changes consistent with an old infarct by 6 wk, but no evidence of atrioventricular conduction loss or heart block (*Lu et al.*, 2016). MCET could also potentially treat hypertrophied regions of the heart other than the septum. This reduced impact may reduce the significant adverse consequences, as seen for some ASA patients (*Folkert et al.*, 2010).

6.2.1.3 Therapy Follow-up

Current studies focus on a 6 week followup. Longer studies might also be helpful to assess safety and efficacy aspects.

Echocardiography is recommended to follow up the treatment for heart function monitoring, specifically, for left ventricular diastolic function and filling pressures (*Nagueh et al.*, 2016). This includes Doppler E/e' ratio, left atrial volume index, pulmonary vein atrial reversal velocity, and peak velocity of ricuspid regurgitation jet by CW Doppler (*Nagueh et al.*, 1999). Aside from assessment of left ventricular filling, 2D and Doppler indices of left ventricular diastolic function provide helpful prognostic information (*Geske et al.*, 2007).

Ambulatory electrocardiographic monitoring for cardiac conduction system plays an important role in evaluating heart function, especially detecting arrhythmia resulting from myocardial ablation (*Adabag et al.*, 2005). In addition, left ventricular diastolic dysfunction causes left ventricular dilatation, which can lead to atrial fibrillation (AF) (*Tsang et al.*, 2002). In MCET, ECG analysis has already shown that a large elevation of the ST segment post treatment, followed by ST-segment suppression and T-wave inversion the next day, which persisted 6 wk after exposure (*Lu et al.*, 2016). Further ECG assessment will help assure that MCET is safe in terms of heart function (arrhythmia).

Additionally, the opportunity for contrast-enhanced cardiac magnetic resonance (CMR) imaging with late gadolinium enhancement (LGE) to identify areas of myocardial fibrosis is promising for monitoring fibrosis growth after ablation (*Rubinshtein et al.*, 2009).

6.2.2 Future Directions

To date, the development of MCET has demonstrated treatment response sufficient for potentially advantageous minimally invasive therapy for myocardial reduc-

tion. Further research is needed to understand the treatment variability, and to assess possible risks of adverse treatment outcome.

A significant local myocardial reduction was demonstrated but still lack unequivocal long-term evidence of the therapeutic benefit. The physical dimension of the employed animal model (rat) is simply too small to investigate any targeted reduction of the outflow tract obstruction in humans. The size also prevents evaluation of methods to treat larger volumes by beam scanning or to map the distribution of microlesions within a given target volume. Investigations in a larger animal model of HCM (pig) in which conditions similar to those found in the human disease would be beneficial for the verification of safe and effective treatment outcomes. In the future, testing of MCET treatment in humans seems premature without evidence of true therapeutic outcome in a larger animal model. Such would include felines which naturally develop HCM. The genetic characteristics of mutations in genes that encode for muscle sarcomeric proteins are similar in cats and humans (*Kittleson et al.*, 2015) and the feline disease closely models the human disease (*Kittleson et al.*, 1999; *Fox et al.*, 2014). The feline model appears to be a logical next step in developing MCET for myocardial reduction therapy, which can be conducted in veterinary hospitals on cats suffering from life threatening HCM.

With a larger animal model, formulating a set of optimized treatment parameters to create a desired total volume reduction needs to be addressed considering a more attenuating acoustic path. Evaluation of beam scanning and to map the distribution of microlesions within a target volume becomes feasible. In the process of MCET, the induced scattered mircolesions are injured cells probably resulting from impact from liquid jets formed during microbubble inertial cavitation. As illustrated in Figure 6.3, a microbubble experiencing ultrasound can undergo inertial cavitation in a vessel leading to vascular rupture, which may also be accompanied with damage to adjacent cells resulting in a microlesion.

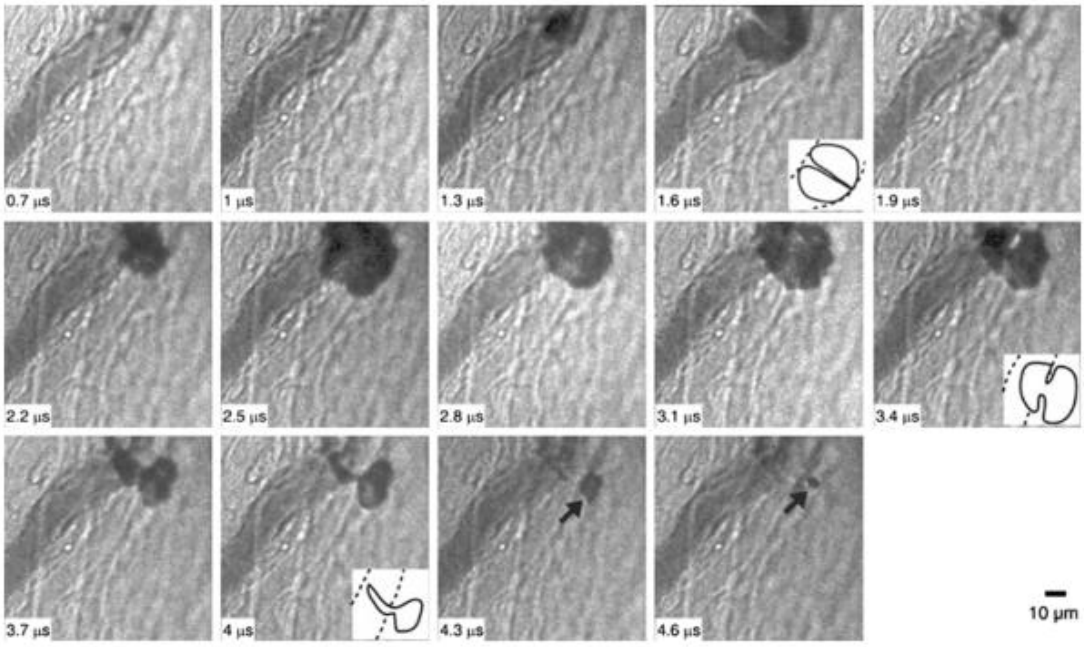

Figure 6.3: Vascular rupture involving a liquid jet. PRPA 4 MPa. Vessel diameter 15 μm. At frame 1.6 μs, a liquid jet appears to be formed inside the bubble and directed toward the right vessel wall. The jet appears to impact the vessel wall. At frame 3.4 μs, the re-expanded bubble contracted showing two connected parts: one outside the vessel and one inside. This leads to a mushroom-shaped form with its stem stretching through the vessel wall (frame 4 μs). Sketches of the bubble in the three characteristic frames are marked with the bubble in solid lines and vessel in dashed lines. In the last frame, the collapsed bubble (arrow) was observed in the interstitial space outside the vessel wall frame. (*Chen et al.*, 2010)

Therefore, future work for MCET monitoring involves development of a coefficient or transfer function relating cavitation signals to the extent of induced microlesion, and feasible applications of cavitation imaging techniques for the more compliated *in vivo* environment. Furthermore, future implementations will combine biological responses, for example, premature electrocardiogram complexes from ECG signal analysis with cavitation activity mapping to predict cell necrosis during the MCET treatment procedure. Eventually, the monitoring of treatment to provide feedback and the real-time control for therapy progression will allow for translation to a clinical setting for cardiac tissue ablation.

Meanwhile, a comprehensive safety analysis is necessary for clinical translation. Efforts may be undertaken to minimize swelling and scarring of the treated volume, and to assess potential adverse hemolytic impacts on circulating blood, possible thrombus initiation by hemolysis or endothelial cell damage.

The overall goal of our MCET investigation will be the introduction of this minimally invasive new tool for myocardial reduction therapy for use in human clinical trials. This innovative technology will advance medical care and improve significantly the prognosis for patients living with life-threatening myocardial hypertrophy.

APPENDIX

APPENDIX A

Programmable Ultrasound Phased Array Therapy System

A.1 Background

There has been an emerging interest in high intensity focused ultrasound (HIFU) for therapeutic applications. By means of its thermal or mechanical effects, HIFU is able to serve as a direct tool for tissue ablation, or an indirect moderating medium to manipulate microbubbles or perform heating (hyperthermia) for the purpose of targeted drug delivery. The development and testing of HIFU based phased arrays is favorable as their elements allow for individual phasing to steer and focus the beam. While FDA has already approved tissue ablation by HIFU for the treatment of uterine fibroids (2004) and pain from bone metastases (2012), development continues on other possible applications that are less forgiving of incomplete treatment, such as thermal necrosis of malignant masses. Ongoing efforts investigate how to maintain focusing through or around aberrating structures, how to minimize damage to tissue surrounding the target area, safely increase focal power, and how to steer in aberrating three-dimensional space.

Ideally, each element, of such an array must have its own fully programmable electrical driving channel, which allows the control of delay, phase, and amplitude of the output from each element. To enable full control, each channel needs a waveform generator, an amplification device, and an impedance matching circuit between driver and acoustic element.

Similar projects utilizing this approach to drive therapeutic arrays include a 512-channel therapy system which was built at the University of Michigan using low cost Field-Programmable Gate Arrays (FPGA) microcontroller and highly efficient MOSFET switching amplifiers (*Hall et al.*, 2006). However, this system lacks the ability to drive both, continuous wave (CW) and transient short duty-cycle high power pulses.

Here presents a hybrid system, which is able to perform CW and transient short duty-cycle high power excitation. In the following we will describe the design, programming, fabrication, and evaluation of this radio frequency (RF) driver system as used in our laboratory for a 1.5 MHz center frequency, 298-element array (Imasonic SA, Besancon, France) (*Kripfgans et al.*, 2012), HIFU-controlled amplifier boards and matching circuitry. Advantages of our design include: 1. Inexpensive components (<$15/channel); 2. Ability to program/drive individual output channels independently; 3. Sufficient time and amplitude resolution for various acoustic pattern design; 4. Capability of hybrid switching between low power CW and short duty cycle, high instantaneous power .

A.2 Methods

Our HIFU driving system was designed and assembled at the University of Michigan. The FPGA system controls 20 amplifier boards (*Umemura and Cain*, 1992), which each controls 16 RF channels, thus in total independently drive up to 320 channels (298 used).

The overall control flow from user inputs to RF outputs is described as in Figure A.1. The system uses 11 FPGA boards (1 synchronizing master board and 10 client boards). The master provides clock (100 MHz) and trigger signals to each client. Each FPGA board has 8 MB SDRAM storage and is able to control a maximum of 32 RF output channels (16 positive and 16 negative controls of 16 P- and N-channel MOSFET pairs). For each channel, frequency, burst length, amplitude, and delay can be programmed.

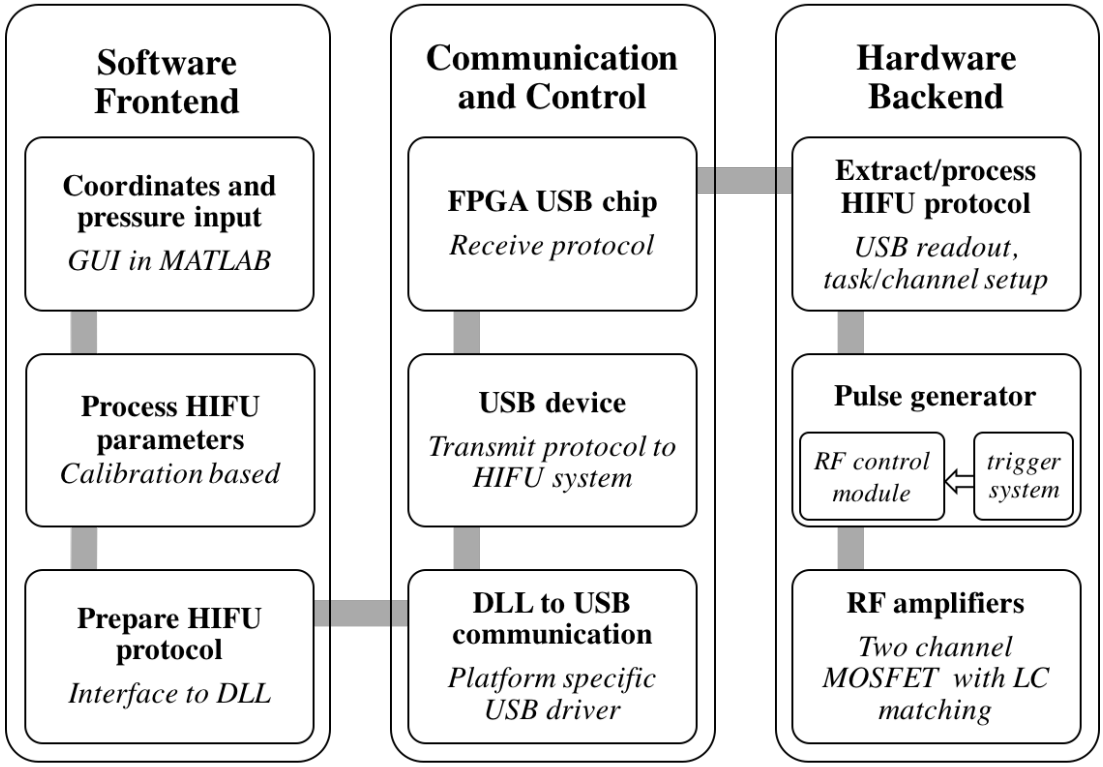

Figure A.1: HIFU system control flow. Frontend software control allows the user to select a series of desired ultrasound focal locations and individual pressure amplitudes. These are processed based on acoustic and electric calibration of the HIFU array and then communicated to the hardware backend. All 320 RF channels are driven in parallel and in real-time through asynchronous FPGA microcontrollers. The frontend is used to setup each channel and to start the general HIFU exposure. Sequential focal locations are internally triggered by the backend and controlled using local on-board SDRAM.

A MATLAB based Graphical User Interface (GUI) with entries of [position #, repetition #] as a task list was developed to program the output sequences and patterns for all channels. Figure A.2 illustrates the idea of high speed execution of complex HIFU exposure patterns by storing HIFU settings for each position in the local FPGA SDRAM. Indexed positions are called in sequence from a task list, that is also stored in SDRAM. This enables the HIFU system to run autonomously and asynchronous from the frontend at an up to 20 kHz position switching rate, which is limited by the SDRAM page read time of 50 s total. Positions define spatial location of the HIFU beam, the wave frequency, burst length, pressure amplitude, and delay for all 320 channels. Pressure is based on calibration data. The task list is set through the frontend GUI and communicated through USB to the backend. Our HIFU system allows up to 16,000 individual 'positions' and 23,000 tasks, where each task can repeat a given 'position' up to 255 times. Complex exposure patterns can be generated by manipulating tasks and 'positions', e.g. triggers generated by the master board, can be of zero amplitude and x-number of cycles, thus defining a user specified pause.

The evaluations for this system were performed to examine the following aspects: (1) Output acoustic pressure measured by a hydrophone in water tank; (2) Electrical power output per channel including peak-output performance and time-average power performance.

A.3 Results

Our phased array HIFU therapy system is able to produce >25 MPa peak negative pressure amplitudes for electronically steered beam positions. The system consists of 320 fully programmable individual broadband channels capable of generating bursts of digital waveforms with 10 ns resolution in a frequency range of 1.5 kHz to 50 MHz.

The generated RF waveforms show a root-mean-square jitter of 2.5 ns with a standard deviation of 1.9 ns, well under the inherent 10 ns system clock resolution.

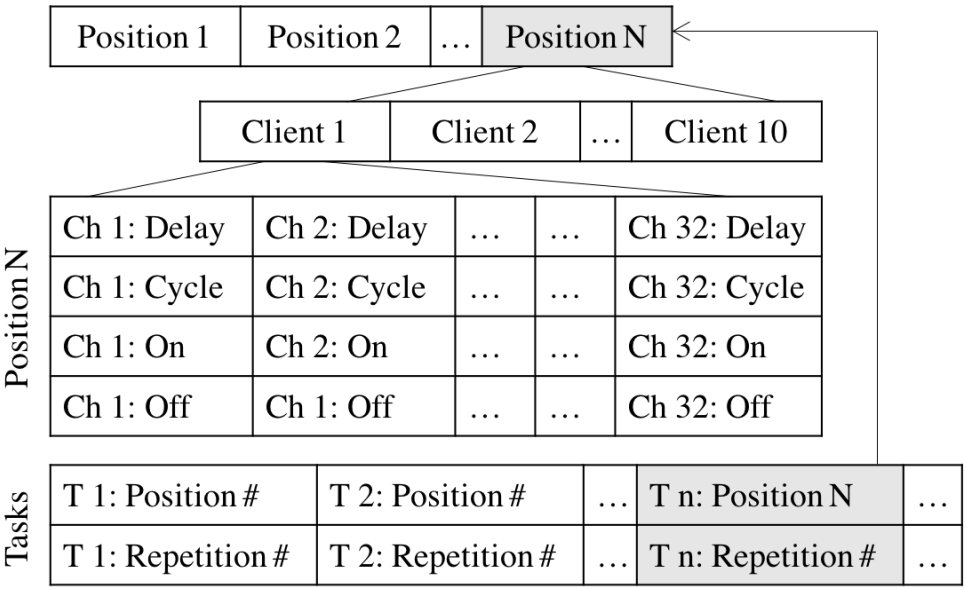

Figure A.2: Illustration of position indexing executed by a task list. User composes a list of tasks (T1, T2, , TN), each repeatable between 1 and 255 times (repetition #). The task list indices refer to 'positions' stored in client board SDRAM. Each of the 10 client boards stores 32 sets of delay, burst length, and number of on/off cycles, for its local 32 channels. (Note: On and Off determine the duty-cycle for each period, thereby controlling the amount of charge able to accumulate on each probe element, and therefore controlling the output pressure, i.e. 10%/20% duty cycle will yield a 20%/100% acoustic pressure, respectively). For every trigger the task pointer advances from n to n+1, calling the associated position # and programming the RF pulse generator. Each position can be repeated up to 255 times.

The usual electrical to acoustical energy transfer efficiency to our specific physical HIFU array is 70%. Electrical drive amplitudes were limited to 450 Vpp to protect the HIFU array elements composite materials.

Peak-output power performance: short-time performance ($< 7\mu s$) allowed for up to 18 Watts of electrical power per channel and produced 30 kW/cm^2 acoustically. Time-average power performance: long-time (CW) performance (<5 s) achieved up to 1 Watt of electrical power per channel and produced 1.7 kW/cm^2 acoustically.

This HIFU system has been validated in Myocardial Cavitation-Enabled Therapy (MCET), where ECG triggering was used to perform a therapy pulse every 8 heartbeats as illustrated in Figure A.3, and treatment paused for heartbeats 2 to 8. Here, therapy is defined as a complex pattern of 4 successive transmits, 250 μs apart. Each transmit consists of a 10-cycle, 1.5 MHz center frequency tone burst with 4 MPa peak rarefactional pressure amplitude (PRPA). The master board sends 4 trigger signals, 250 μs apart, for every external trigger (i.e. from ECG system). The task list contains two items: (1) an active item, fire at a given coordinate, repeat 4 times (=1×4), and (2) a passive item, pause the system (zero amplitude) by not firing, repeat 28 times (=7×4).

A.4 Interpretation

Here presents a low-cost programmable hybrid HIFU system, providing a design potentially attractive to ultrasonic therapy projects with complex demands. The system is capable to operate in high power (40 MPa peak-to-peak) low duty cycle (1%) pulses or low power (5 MPa peak-to-peak) high duty cycle (98%), beneficial to both mechanical (e.g. MCET and histotripsy) and thermal (e.g. hyperthermia) based therapy. The structured FPGA control framework includes a synchronizing master board and independent client boards both controlled using one Verilog file. The system can be easily configured to drive a flexible number of channels by simply

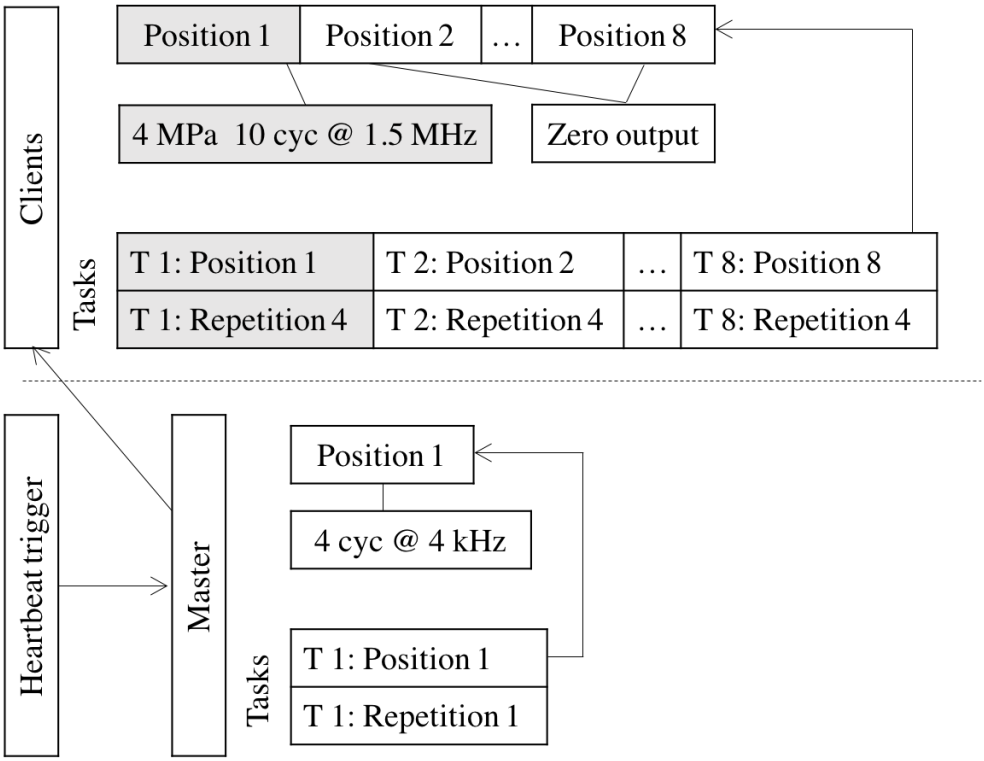

Figure A.3: Illustration of position indexing executed by the task list used for MCET therapy (10-cycle 1.5 MHz center frequency bursts, 4 MPa peak rarefactional pressure, 4 repetitions at 4 kHz every 8 heartbeats.

adding client FPGA boards/amplifiers. The driving circuits employ standard, non-expensive, off-the-shelf components. Commercial signal/power generators that would meet the aforementioned requirements would likely be more expensive.

BIBLIOGRAPHY

BIBLIOGRAPHY

Adabag, A. S., S. A. Casey, M. A. Kuskowski, A. G. Zenovich, and B. J. Maron (2005), Spectrum and prognostic significance of arrhythmias on ambulatory holter electrocardiogram in hypertrophic cardiomyopathy, *Journal of the American College of Cardiology*, *45*(5), 697–704.

Apfel, R. (1982), Acoustic cavitation: a possible consequence of biomedical uses of ultrasound., *The British journal of cancer. Supplement*, *5*, 140.

Arvanitis, C., N. McDannold, and G. Clement (2015), Fast passive cavitation mapping with angular spectrum approach, *The Journal of the Acoustical Society of America*, *138*(3), 1845–1845.

Baggish, A. L., R. N. Smith, I. Palacios, G. J. Vlahakes, D. M. Yoerger, M. H. Picard, P. A. Lowry, I. Jang, and M. A. Fifer (2006), Pathological effects of alcohol septal ablation for hypertrophic obstructive cardiomyopathy, *Heart*, *92*(12), 1773–1778.

Bao, S., B. D. Thrall, and D. L. Miller (1997), Transfection of a reporter plasmid into cultured cells by sonoporation in vitro, *Ultrasound in medicine & biology*, *23*(6), 953–959.

Baroldi, G. (1975), Different types of myocardial necrosis in coronary heart disease: a pathophysiologic review of their functional significance, *American heart journal*, *89*(6), 742–752.

Bassien-Capsa, V., J.-C. Fouron, B. Comte, and A. Chorvatova (2006), Structural, functional and metabolic remodeling of rat left ventricular myocytes in normal and in sodium-supplemented pregnancy, *Cardiovascular research*, *69*(2), 423–431.

Bouma, H., J. J. Sonnemans, A. Vilanova, and F. A. Gerritsen (2009), Automatic detection of pulmonary embolism in cta images, *IEEE transactions on medical imaging*, *28*(8), 1223–1230.

Bouraoui, B., C. Ronse, J. Baruthio, N. Passat, and P. Germain (2010), 3d segmentation of coronary arteries based on advanced mathematical morphology techniques, *Computerized medical imaging and graphics*, *34*(5), 377–387.

Brown, M. L., H. V. Schaff, J. A. Dearani, Z. Li, R. A. Nishimura, and S. R. Ommen (2011), Relationship between left ventricular mass, wall thickness, and survival after subaortic septal myectomy for hypertrophic obstructive cardiomyopathy, *The Journal of thoracic and cardiovascular surgery*, *141*(2), 439–443.

Brown, R. E. (1965), The pattern of the microcirculatory bed in the ventricular myocardium of domestic mammals, *Developmental Dynamics*, *116*(2), 355–373.

Bruce, M., M. Averkiou, S. Jensen, J. Powers, and K. Beach (2003), Pulse inversion doppler for blood flow detection in the macro-and microcirculation, in *Ultrasonics, 2003 IEEE Symposium on*, vol. 1, pp. 411–415, IEEE.

Burgess, A., and K. Hynynen (2014), Drug delivery across the blood–brain barrier using focused ultrasound, *Expert opinion on drug delivery*, *11*(5), 711–721.

Calliada, F., R. Campani, O. Bottinelli, A. Bozzini, and M. G. Sommaruga (1998), Ultrasound contrast agents: basic principles, *European journal of radiology*, *27*, S157–S160.

Carstensen, E., and H. Flynn (1982), The potential for transient cavitation with microsecond pulses of ultrasound, *Ultrasound in medicine & biology*, *8*(6), L720–L724.

Carstensen, E. L., S. Gracewski, and D. Dalecki (2000), The search for cavitation in vivo, *Ultrasound in medicine & biology*, *26*(9), 1377–1385.

Chen, H., A. A. Brayman, M. R. Bailey, and T. J. Matula (2010), Blood vessel rupture by cavitation, *Urological research*, *38*(4), 321–326.

Chen, H., A. A. Brayman, A. P. Evan, and T. J. Matula (2012), Preliminary observations on the spatial correlation between short-burst microbubble oscillations and vascular bioeffects, *Ultrasound in medicine & biology*, *38*(12), 2151–2162.

Choi, W.-Y., and K. D. Poss (2012), Cardiac regeneration, *Current topics in developmental biology*, *100*, 319.

Church, C. C. (2002), Spontaneous homogeneous nucleation, inertial cavitation and the safety of diagnostic ultrasound, *Ultrasound in medicine & biology*, *28*(10), 1349–1364.

Cochran, M. C., J. Eisenbrey, R. O. Ouma, M. Soulen, and M. A. Wheatley (2011), Doxorubicin and paclitaxel loaded microbubbles for ultrasound triggered drug delivery, *International journal of pharmaceutics*, *414*(1), 161–170.

Collin, J., C. Coviello, E. Lyka, T. Leslie, and C. C. Coussios (2013), Real-time three-dimensional passive cavitation detection for clinical high intensity focussed ultrasound systems, *Proceedings of Meetings on Acoustics ICA2013*, *19*(1), 075,023.

Crake, C., M. de Saint Victor, J. Owen, C. Coviello, J. Collin, C.-C. Coussios, and E. Stride (2015), Passive acoustic mapping of magnetic microbubbles for cavitation enhancement and localization, *Physics in medicine and biology*, *60*(2), 785.

Crutchfield, A., K. Diller, and J. Brand (1999), Cryopreservation of chlamydomonas reinhardtii (chlorophyta), *European Journal of Phycology*, *34*(1), 43–52.

Dabrowski, M., L. Chojnowska, L. Malek, M. Spiewak, B. Kusmierczyk, J. Koziarek, A. Klisiewicz, J. Misko, and A. Witkowski (2012), An assessment of regression of left ventricular hypertrophy following alcohol ablation of the interventricular septum in patients with hypertrophic cardiomyopathy with left ventricular outflow tract obstruction, *Kardiol Pol*, *70*(8), 782–8.

Dbaibo, G. S., M. Y. Pushkareva, R. A. Rachid, N. Alter, M. J. Smyth, L. M. Obeid, and Y. A. Hannun (1998), p53-dependent ceramide response to genotoxic stress., *Journal of Clinical Investigation*, *102*(2), 329.

Dbaibo, G. S., et al. (2001), Ceramide generation by two distinct pathways in tumor necrosis factor α-induced cell death, *FEBS letters*, *503*(1), 7–12.

Doppler, S. A., M.-A. Deutsch, R. Lange, and M. Krane (2013), Cardiac regeneration: current therapies—future concepts, *Journal of thoracic disease*, *5*(5), 683–697.

Eils, R., and C. Athale (2003), Computational imaging in cell biology, *The Journal of cell biology*, *161*(3), 477–481.

El Masry, H., and J. A. Breall (2008), Alcohol septal ablation for hypertrophic obstructive cardiomyopathy., *Current cardiology reviews*, *4*(3), 193–197.

Farny, C. H., R. G. Holt, and R. A. Roy (2009), Temporal and spatial detection of hifu-induced inertial and hot-vapor cavitation with a diagnostic ultrasound system, *Ultrasound in medicine & biology*, *35*(4), 603–615.

Fifer, M. A., and U. Sigwart (2011), Hypertrophic obstructive cardiomyopathy: alcohol septal ablation, *European heart journal*, *32*(9), 1059–1064.

Folkert, J., O. I. Soliman, M. Michels, D. A. Theuns, P. L. de Jong, M. L. Geleijnse, and P. W. Serruys (2010), Long-term outcome of alcohol septal ablation in patients with obstructive hypertrophic cardiomyopathyclinical perspective, *Circulation: Heart Failure*, *3*(3), 362–369.

Fowlkes, J. B., and C. Holland (2000), Mechanical bioeffects from diagnostic ultrasound: Aium consensus statements. american institute of ultrasound in medicine., *Journal of ultrasound in medicine: official journal of the American Institute of Ultrasound in Medicine*, *19*(2), 69–72.

Fox, P. R., C. Basso, G. Thiene, and B. J. Maron (2014), Spontaneously occurring restrictive nonhypertrophied cardiomyopathy in domestic cats: A new animal model of human disease, *Cardiovascular Pathology*, *23*(1), 28–34.

Frimm, C. D. C., Y. Sun, and K. T. Weber (1997), Angiotensin ii receptor blockade and myocardial fibrosis of the infarcted rat heart, *Journal of Laboratory and Clinical Medicine*, *129*(4), 439–446.

Gateau, J., J.-F. Aubry, M. Pernot, M. Fink, and M. Tanter (2011), Combined passive detection and ultrafast active imaging of cavitation events induced by short pulses of high-intensity ultrasound, *IEEE transactions on ultrasonics, ferroelectrics, and frequency control*, *58*(3), 517–532.

Gersh, B. J., et al. (2011), 2011 accf/aha guideline for the diagnosis and treatment of hypertrophic cardiomyopathy, *Circulation*, pp. CIR–0b013e318,223e2bd.

Geske, J. B., P. Sorajja, R. A. Nishimura, and S. R. Ommen (2007), Evaluation of left ventricular filling pressures by doppler echocardiography in patients with hypertrophic cardiomyopathy, *Circulation*, *116*(23), 2702–2708.

Gyöngy, M., and C.-C. Coussios (2010), Passive spatial mapping of inertial cavitation during hifu exposure, *IEEE Transactions on Biomedical Engineering*, *57*(1), 48–56.

Gyongy, M., M. Arora, J. A. Noble, and C. C. Coussios (2008), Use of passive arrays for characterization and mapping of cavitation activity during hifu exposure, in *Ultrasonics Symposium, 2008. IUS 2008. IEEE*, pp. 871–874, IEEE.

H. Abadi, S., M. J. Van Overloop, and D. R. Dowling (2013), Frequency-sum beamforming in an inhomogeneous environment, *Proceedings of Meetings on Acoustics ICA2013*, *19*(1), 055,080.

Haimovitz-Friedman, A., C.-C. Kan, D. Ehleiter, R. S. Persaud, M. McLoughlin, Z. Fuks, and R. N. Kolesnick (1994), Ionizing radiation acts on cellular membranes to generate ceramide and initiate apoptosis., *The Journal of experimental medicine*, *180*(2), 525–535.

Hall, T., C. Cain, G. T. Clement, N. J. McDannold, and K. Hynynen (2006), A low cost compact 512 channel therapeutic ultrasound system for transcutaneous ultrasound surgery, *AIP Conference Proceedings*, *829*(1), 445–449.

Haworth, K. J., T. D. Mast, K. Radhakrishnan, M. T. Burgess, J. A. Kopechek, S.-L. Huang, D. D. McPherson, and C. K. Holland (2012), Passive imaging with pulsed ultrasound insonations, *The Journal of the Acoustical Society of America*, *132*(1), 544–553.

Haworth, K. J., K. B. Bader, K. T. Rich, C. K. Holland, and T. D. Mast (2016), Quantitative frequency-domain passive cavitation imaging, *IEEE Transactions on Ultrasonics, Ferroelectrics, and Frequency Control*.

Hernot, S., and A. L. Klibanov (2008), Microbubbles in ultrasound-triggered drug and gene delivery, *Advanced drug delivery reviews*, *60*(10), 1153–1166.

Ho, S. Y. (2009), Anatomy and myoarchitecture of the left ventricular wall in normal and in disease, *European Heart Journal-Cardiovascular Imaging*, *10*(8), iii3–iii7.

Hunter, R. S. (1948), Accuracy, precision, and stability of new photoelectric color-difference meter, *Journal of the Optical Society of America*, *38*(12), 1094–1094.

Hunter, R. S. (1958), Photoelectric color difference meter, *Josa*, *48*(12), 985–995.

Ibsen, S., C. E. Schutt, and S. Esener (2013), Microbubble-mediated ultrasound therapy: a review of its potential in cancer treatment, *Drug Des Devel Ther*, *7*, 375–388.

Ignee, A., N. S. Atkinson, G. Schuessler, C. F. Dietrich, et al. (2016), Ultrasound contrast agents, *Endoscopic Ultrasound*, *5*(6), 355.

Illing, R., et al. (2005), The safety and feasibility of extracorporeal high-intensity focused ultrasound (hifu) for the treatment of liver and kidney tumours in a western population, *British journal of cancer*, *93*(8), 890–895.

Jacyn Baker, C., and N. M. Mock (1994), An improved method for monitoring cell death in cell suspension and leaf disc assays using evans blue, *Plant Cell, Tissue and Organ Culture*, *39*(1), 7–12.

Jennings, R. B., H. M. Sommers, P. B. Herdson, and J. P. Kaltenbach (1969), Ischemic injury of myocardium, *Annals of the New York Academy of Sciences*, *156*(1), 61–78.

Jensen, C. R., R. W. Ritchie, M. Gyöngy, J. R. Collin, T. Leslie, and C.-C. Coussios (2012), Spatiotemporal monitoring of high-intensity focused ultrasound therapy with passive acoustic mapping, *Radiology*, *262*(1), 252–261.

Jensen, J. A., and N. B. Svendsen (1992), Calculation of pressure fields from arbitrarily shaped, apodized, and excited ultrasound transducers, *IEEE transactions on ultrasonics, ferroelectrics, and frequency control*, *39*(2), 262–267.

Kittleson, M. D., K. M. Meurs, M. J. Munro, J. A. Kittleson, S.-K. Liu, P. D. Pion, and J. A. Towbin (1999), Familial hypertrophic cardiomyopathy in maine coon cats, *Circulation*, *99*(24), 3172–3180.

Kittleson, M. D., K. M. Meurs, and S. P. Harris (2015), The genetic basis of hypertrophic cardiomyopathy in cats and humans, *Journal of Veterinary Cardiology*, *17*, S53–S73.

Kooiman, K., H. J. Vos, M. Versluis, and N. de Jong (2014), Acoustic behavior of microbubbles and implications for drug delivery, *Advanced drug delivery reviews*, *72*, 28–48.

Kripfgans, O., A. Covert, F. Padilla, J. Fowlkes, M. Fabiilli, M. Moghaddam, P. Carson, R. Muratore, and E. E. Konofagou (2012), Ultrasound thermal ablation system and methods for treatment of breast cancer, *AIP Conference Proceedings*, *1481*(1), 185–190.

Laing, S. T., and D. D. McPherson (2009), Cardiovascular therapeutic uses of targeted ultrasound contrast agents, *Cardiovascular research*, *83*(4), 626–635.

Lawrenz, T., et al. (2011), Endocardial radiofrequency ablation for hypertrophic obstructive cardiomyopathy, *Journal of the American College of Cardiology*, *57*(5), 572–576.

Leighton, T. G. (2007), What is ultrasound?, *Progress in biophysics and molecular biology*, *93*(1), 3–83.

Lentacker, I., S. C. De Smedt, and N. N. Sanders (2009), Drug loaded microbubble design for ultrasound triggered delivery, *Soft Matter*, *5*(11), 2161–2170.

Leonardi, R. A., E. P. Kransdorf, D. L. Simel, and A. Wang (2010), Meta-analyses of septal reduction therapies for obstructive hypertrophic cardiomyopathyclinical perspective, *Circulation: Cardiovascular Interventions*, *3*(2), 97–104.

Lu, X., D. L. Miller, C. Dou, Y. I. Zhu, M. L. Fabiilli, G. E. Owens, and O. D. Kripfgans (2016), Maturation of lesions induced by myocardial cavitation-enabled therapy, *Ultrasound in medicine & biology*, *42*(7), 1541–1550.

Ma, J., L. F. Du, M. Chen, H. H. Wang, L. X. Xing, L. F. Jing, and Y. H. Li (2013), Drug-loaded nano-microcapsules delivery system mediated by ultrasound-targeted microbubble destruction: A promising therapy method (review), *Biomedical reports*, *1*(4), 506–510.

Mamou, J., A. Coron, M. Hata, J. Machi, E. Yanagihara, P. Laugier, and E. J. Feleppa (2010), Three-dimensional high-frequency characterization of cancerous lymph nodes, *Ultrasound in medicine & biology*, *36*(3), 361–375.

Marian, A. J. (2009), Contemporary treatment of hypertrophic cardiomyopathy, *Tex Heart Inst J*, *36*(3), 194–204.

Maron, B. J. (2005), Surgery for hypertrophic obstructive cardiomyopathy.

Maron, B. J., and M. S. Maron (2013), Hypertrophic cardiomyopathy, *The Lancet*, *381*(9862), 242–255.

Maron, B. J., M. S. Maron, and C. Semsarian (2012), Genetics of hypertrophic cardiomyopathy after 20 years: clinical perspectives, *Journal of the American College of Cardiology*, *60*(8), 705–715.

Maron, B. J., et al. (2003a), American college of cardiology/european society of cardiology clinical expert consensus document on hypertrophic cardiomyopathy: a report of the american college of cardiology foundation task force on clinical expert consensus documents and the european society of cardiology committee for practice guidelines, *Journal of the American College of Cardiology*, *42*(9), 1687–1713.

Maron, M. S., I. Olivotto, and B. J. Maron (2003b), Hypertrophic cardiomyopathy and outflow tract obstruction, *The New England journal of medicine*, *348*(18), 1815–1816.

McLaughlan, J., I. Rivens, T. Leighton, and G. Ter Haar (2010), A study of bubble activity generated in ex vivo tissue by high intensity focused ultrasound, *Ultrasound in medicine & biology*, *36*(8), 1327–1344.

Members, W. C., et al. (2011), 2011 accf/aha guideline for the diagnosis and treatment of hypertrophic cardiomyopathy: Executive summary: A report of the american college of cardiology foundation/american heart association task force on practice guidelines, *The Journal of Thoracic and Cardiovascular Surgery*, *142*(6), 1303–1338.

Miller, D. L. (2007), Overview of experimental studies of biological effects of medical ultrasound caused by gas body activation and inertial cavitation, *Progress in biophysics and molecular biology*, *93*(1), 314–330.

Miller, D. L., P. Li, C. Dou, D. Gordon, C. A. Edwards, and W. F. Armstrong (2005a), Influence of contrast agent dose and ultrasound exposure on cardiomyocyte injury induced by myocardial contrast echocardiography in rats 1, *Radiology*, *237*(1), 137–143.

Miller, D. L., P. Li, D. Gordon, and W. F. Armstrong (2005b), Histological characterization of microlesions induced by myocardial contrast echocardiography, *Echocardiography*, *22*(1), 25–34.

Miller, D. L., C. Dou, and R. C. Wiggins (2007), Simulation of diagnostic ultrasound image pulse sequences in cavitation bioeffects research, *The Journal of the Acoustical Society of America*, *122*(4), 2002–2008.

Miller, D. L., M. A. Averkiou, A. A. Brayman, E. C. Everbach, C. K. Holland, J. H. Wible, and J. Wu (2008), Bioeffects considerations for diagnostic ultrasound contrast agents, *Journal of Ultrasound in Medicine*, *27*(4), 611–632.

Miller, D. L., C. Dou, and B. R. Lucchesi (2011), Are ecg premature complexes induced by ultrasonic cavitation electrophysiological responses to irreversible cardiomyocyte injury?, *Ultrasound in Medicine & Biology*, *37*(2), 312–320.

Miller, D. L., C. Dou, G. E. Owens, and O. D. Kripfgans (2014a), Optimization of ultrasound parameters of myocardial cavitation microlesions for therapeutic application, *Ultrasound in Medicine & Biologyedicine & biology*, *40*(6), 1228–1236.

Miller, D. L., C. Dou, G. E. Owens, and O. D. Kripfgans (2014b), Timing of high-intensity pulses for myocardial cavitation-enabled therapy, *Journal of Therapeutic Ultrasound*, *2*(1), 20.

Miller, D. L., C. Dou, X. Lu, Y. I. Zhu, M. L. Fabiilli, G. E. Owens, and O. D. Kripfgans (2015), Use of theranostic strategies in myocardial cavitation-enabled therapy, *Ultrasound in Medicine & Biology*, *41*(7), 1865–1875.

Miller, D. L., X. Lu, M. Fabiilli, and C. Dou (2016), Do anesthetic techniques influence the threshold for glomerular capillary hemorrhage induced in rats by contrast-enhanced diagnostic ultrasound?, *Journal of Ultrasound in Medicine*, *35*(2), 373–380.

Moayyeri, A., J. Adams, R. Adler, M.-A. Krieg, D. Hans, J. Compston, and E. Lewiecki (2012), Quantitative ultrasound of the heel and fracture risk assessment: an updated meta-analysis, *Osteoporosis International*, *23*(1), 143–153.

Molina, C. A., et al. (2009), Transcranial ultrasound in clinical sonothrombolysis (tucson) trial, *Annals of neurology*, *66*(1), 28–38.

Nagueh, S. F., N. M. Lakkis, K. J. Middleton, W. H. Spencer, W. A. Zoghbi, and M. A. Quinones (1999), Doppler estimation of left ventricular filling pressures in patients with hypertrophic cardiomyopathy, *Circulation*, *99*(2), 254–261.

Nagueh, S. F., et al. (2016), Recommendations for the evaluation of left ventricular diastolic function by echocardiography: an update from the american society of echocardiography and the european association of cardiovascular imaging, *Journal of the American Society of Echocardiography*, *29*(4), 277–314.

Newman, C., and T. Bettinger (2007), Gene therapy progress and prospects: ultrasound for gene transfer, *Gene therapy*, *14*(6), 465–475.

Newman, C. M., A. Lawrie, A. F. Brisken, and D. C. Cumberland (2001), Ultrasound gene therapy: on the road from concept to reality, *Echocardiography*, *18*(4), 339–347.

Nishimura, R. A., and S. R. Ommen (2010), Septal reduction therapy for obstructive hypertrophic cardiomyopathy and sudden death, *Circulation: Cardiovascular Interventions*, *3*(2), 91–93.

O'brien, P., et al. (2006), Cardiac troponin i is a sensitive, specific biomarker of cardiac injury in laboratory animals, *Laboratory animals*, *40*(2), 153–171.

Ommen, S. R., and R. A. Nishimura (2004), Hypertrophic cardiomyopathy, *Current problems in cardiology*, *29*(5), 239–291.

Oparil, S., S. P. Bishop, and F. J. Clubb (1984), Myocardial cell hypertrophy or hyperplasia., *Hypertension*, *6*(6 Pt 2), III38.

Otsuka, R., et al. (2007), Extracardiac ablation of the left ventricular septum in beating canine hearts using high-intensity focused ultrasound, *Journal of the American Society of Echocardiography*, *20*(12), 1400–1406.

Pham, D. L., C. Xu, and J. L. Prince (2000), Current methods in medical image segmentation 1, *Annual review of biomedical engineering*, *2*(1), 315–337.

Pinter, S. Z., J. M. Rubin, O. D. Kripfgans, M. C. Treadwell, V. C. Romero, M. S. Richards, M. Zhang, A. L. Hall, and J. B. Fowlkes (2012), Three-dimensional sonographic measurement of blood volume flow in the umbilical cord, *Journal of Ultrasound in Medicine*, *31*(12), 1927–1934.

Pitt, W. G., G. A. Husseini, and B. J. Staples (2004), Ultrasonic drug delivery–a general review, *Expert opinion on drug delivery*, *1*(1), 37–56.

Potter, R., and A. Groom (1983), Capillary diameter and geometry in cardiac and skeletal muscle studied by means of corrosion casts, *Microvascular research*, *25*(1), 68–84.

Qu, F., D. Ren, X. Liu, Z. Jing, and L. Yan (2012), A face image illumination quality evaluation method based on gaussian low-pass filter, in *Cloud Computing and Intelligent Systems (CCIS), 2012 IEEE 2nd International Conference on*, vol. 1, pp. 176–180, IEEE.

Raute-Kreinsen, U. (2003), Morphology of necrosis and repair after transcoronary ethanol ablation of septal hypertrophy, *Pathology-Research and Practice*, *199*(3), 121–127.

Roberts, C. S., D. Maclean, P. Maroko, and R. Kloner (1985), Relation of early mononuclear and polymorphonuclear cell infiltration to late scar thickness after experimentally induced myocardial infarction in the rat, *Basic research in cardiology*, *80*(2), 202–209.

Roberts, W. W., T. L. Hall, K. Ives, J. S. Wolf, J. B. Fowlkes, and C. A. Cain (2006), Pulsed cavitational ultrasound: a noninvasive technology for controlled tissue ablation (histotripsy) in the rabbit kidney, *The Journal of urology*, *175*(2), 734–738.

Rotolo, J. A., J. Zhang, M. Donepudi, H. Lee, Z. Fuks, and R. Kolesnick (2005), Caspase-dependent and-independent activation of acid sphingomyelinase signaling, *Journal of Biological Chemistry*, *280*(28), 26,425–26,434.

Rubinshtein, R., et al. (2009), Characteristics and clinical significance of late gadolinium enhancement by contrast-enhanced magnetic resonance imaging in patients with hypertrophic cardiomyopathy, *Circulation: Heart Failure*, pp. CIRCHEARTFAILURE–109.

Salgaonkar, V. A., S. Datta, C. K. Holland, and T. D. Mast (2009), Passive cavitation imaging with ultrasound arrays, *The Journal of the Acoustical Society of America*, *126*(6), 3071–3083.

Samuel, S., M. A. Cooper, J. L. Bull, J. B. Fowlkes, and D. L. Miller (2009), An ex vivo study of the correlation between acoustic emission and microvascular damage, *Ultrasound in medicine & biology*, *35*(9), 1574–1586.

Sboros, V. (2008), Response of contrast agents to ultrasound, *Advanced drug delivery reviews*, *60*(10), 1117–1136.

Schutt, E. G., D. H. Klein, R. M. Mattrey, and J. G. Riess (2003), Injectable microbubbles as contrast agents for diagnostic ultrasound imaging: the key role of perfluorochemicals, *Angewandte Chemie International Edition*, *42*(28), 3218–3235.

Seggewiss, H., L. Faber, and U. Gleichmann (1999), Percutaneous transluminal septal ablation in hypertrophic obstructive cardiomyopathy, *The Thoracic and cardiovascular surgeon*, *47*(02), 94–100.

Skyba, D. M., R. J. Price, A. Z. Linka, T. C. Skalak, and S. Kaul (1998), Direct in vivo visualization of intravascular destruction of microbubbles by ultrasound and its local effects on tissue, *Circulation*, *98*(4), 290–293.

Sorajja, P., U. Valeti, R. A. Nishimura, S. R. Ommen, C. S. Rihal, B. J. Gersh, D. O. Hodge, H. V. Schaff, and D. R. Holmes (2008), Outcome of alcohol septal ablation for obstructive hypertrophic cardiomyopathy, *Circulation*, *118*(2), 131–139.

Teekakirikul, P., R. F. Padera, J. G. Seidman, and C. E. Seidman (2012), Hypertrophic cardiomyopathy: translating cellular cross talk into therapeutics.

Tsang, T. S., et al. (2002), Left ventricular diastolic dysfunction as a predictor of the first diagnosed nonvalvular atrial fibrillation in 840 elderly men and women, *Journal of the American College of Cardiology*, *40*(9), 1636–1644.

Umemura, S.-i., and C. A. Cain (1992), Acoustical evaluation of a prototype sector-vortex phased-array applicator, *IEEE transactions on ultrasonics, ferroelectrics, and frequency control*, *39*(1), 32–38.

Unger, E., T. Porter, J. Lindner, and P. Grayburn (2014), Cardiovascular drug delivery with ultrasound and microbubbles, *Advanced drug delivery reviews*, *72*, 110–126.

Unger, E. C., T. O. Matsunaga, T. McCreery, P. Schumann, R. Sweitzer, and R. Quigley (2002), Therapeutic applications of microbubbles, *European journal of radiology*, *42*(2), 160–168.

Vaezy, S., M. Andrew, P. Kaczkowski, and L. Crum (2001), Image-guided acoustic therapy, *Annual review of biomedical engineering*, *3*(1), 375–390.

Vignon, F., W. T. Shi, J. E. Powers, E. C. Everbach, J. Liu, S. Gao, F. Xie, and T. R. Porter (2013), Microbubble cavitation imaging, *IEEE Transactions on Ultrasonics, Ferroelectrics, and Frequency Controlerroelectrics, and Frequency Control*, *60*(4), 661–670.

Weissleder, R. (2002), Scaling down imaging: molecular mapping of cancer in mice, *Nature Reviews Cancer*, *2*(1), 11–18.

Weissleder, R. (2006), Molecular imaging in cancer, *Science*, *312*(5777), 1168–1171.

Wu, J., J. P. Ross, and J.-F. Chiu (2002), Reparable sonoporation generated by microstreaming, *The Journal of the Acoustical Society of America*, *111*(3), 1460–1464.

Xu, S., H. Hu, H. Jiang, Z. Xu, and M. Wan (2014), Ultrafast 2-dimensional image monitoring and array-based passive cavitation detection for ultrasound contrast agent destruction in a variably sized region, *Journal of Ultrasound in Medicine*, *33*(11), 1957–1970.

Xu, Y., G. Liang, G. Hu, Y. Yang, J. Geng, and P. K. Saha (2012), Quantification of coronary arterial stenoses in cta using fuzzy distance transform, *Computerized Medical Imaging and Graphics*, *36*(1), 11–24.

Xu, Z., A. Ludomirsky, L. Y. Eun, T. L. Hall, B. C. Tran, J. B. Fowlkes, and C. A. Cain (2004), Controlled ultrasound tissue erosion, *IEEE transactions on ultrasonics, ferroelectrics, and frequency control*, *51*(6), 726–736.

Zhou, C., L. M. Hadjiiski, B. Sahiner, H.-P. Chan, S. Patel, P. Cascade, E. A. Kazerooni, and J. Wei (2003), Computerized detection of pulmonary embolism in 3d computed tomographic (ct) images: vessel tracking and segmentation techniques, in *Medical Imaging 2003*, pp. 1613–1620, International Society for Optics and Photonics.

Zhou, C., H.-P. Chan, A. Chughtai, S. Patel, L. M. Hadjiiski, J. Wei, and E. A. Kazerooni (2012), Automated coronary artery tree extraction in coronary ct angiography using a multiscale enhancement and dynamic balloon tracking (mscar-dbt) method, *Computerized Medical Imaging and Graphics*, *36*(1), 1–10.

Zhu, Y. I., D. L. Miller, C. Dou, and O. D. Kripfgans (2015a), Characterization of macrolesions induced by myocardial cavitation-enabled therapy, *IEEE Transactions on Biomedical Engineering*, *62*(2), 717–727.

Zhu, Y. I., D. L. Miller, C. Dou, X. Lu, and O. D. Kripfgans (2015b), Quantitative assessment of damage during mcet: A parametric study in a rodent model, *Journal of Therapeutic Ultrasound*, *3*(1), 18.

Zhu, Y. I., D. L. Miller, C. Dou, and O. D. Kripfgans (2017), Passive microlesion detection and mapping for treatment of hypertrophic cardiomyopathy, *AIP Conference Proceedings*, *1816*(1), 030,002.